

QUARTERLY REPORT of

RTRI

Aug. 2022 Vol. 63 No. 3
CONTENTS

Power Supply Technology

PERSPECTIVE

- 151 Research and Development on Power Supply Systems for a Sustainable Society
..... H.SHIGEEDA

PAPERS

- 163 Method for Estimating Equivalent Salt Deposit Density on Insulator Surfaces Using
Meteorological and Topographical Information Provided by Public Institutions
..... T.USUKI, N.SHIBATA
- 169 Exposition of Revision of Seismic Design Guideline for Overhead Contact Systems
..... Y.KONDO
- 175 DC-DC Converter Control Method for High Voltage DC Feeding System to Improve Use
of Regenerative Power T.YOSHII, T.OIDE

Signalling and Telecommunication Systems

PERSPECTIVE

- 155 Trend on Research and Development Activities Relating to Signalling and
Telecommunication Systems in Railway Fields K.KAWASAKI

PAPERS

- 181 Train Frontal Obstacle Detection Method with Camera-LiDAR Fusion
..... R.KAGEYAMA, N.NAGAMINE, H.MUKOJIMA
- 187 Development of Automatic Train Operation System Based on Intermittent Type ATP
with Continuous Speed Checks H.FUJITA, T.NOMURA, T.AOYAGI, S.MORITA
- 193 Study of Anomalous Characteristics Exhibiting Between Fixing Force of Switch and
Tongue Rail Opening Force
..... S.SHIOMI, Y.OSHIMI, K.TSUBAKI, K.TAKASAKI, T.SATO

Materials Technology

PERSPECTIVE

- 159 Research and Development Activities and Future Outlook in Materials Technology
..... H.UEDA

PAPERS

- 200 Evaluation of Material Properties of Pantograph Contact Strip by Microscopic Structure
Model F.MORIMOTO, Y.KUBOTA
- 206 Moisture Behavior in Concrete Repaired by Patching Observed with Neutron Imaging
..... H.SUZUKI, M.UEHARA, M.MIZUTA, Y.OTAKE
- 212 Effects of Rotational Conditions on Performance of Gear Unit Pinion Bearing
..... K.TAKAHASHI, D.SUZUKI, T.NAGATOMO
- 218 Summaries of RTRI REPORT (in Japanese)
- 222 Annual Index: Subjects Vol.63, No.1-No.3 (2022)



CONTENTS

PERSPECTIVES

- 151 Research and Development on Power Supply Systems for a Sustainable Society H.SHIGEEDA
155 Trend on Research and Development Activities Relating to Signalling and Telecommunication Systems in Railway Fields K.KAWASAKI
159 Research and Development Activities and Future Outlook in Materials Technology H.UEDA

PAPERS

- 163 Method for Estimating Equivalent Salt Deposit Density on Insulator Surfaces Using Meteorological and Topographical Information Provided by Public Institutions T.USUKI, N.SHIBATA
169 Exposition of Revision of Seismic Design Guideline for Overhead Contact Systems Y.KONDO
175 DC-DC Converter Control Method for High Voltage DC Feeding System to Improve Use of Regenerative Power T.YOSHII, T.OIDE
181 Train Frontal Obstacle Detection Method with Camera-LiDAR Fusion R.KAGEYAMA, N.NAGAMINE, H.MUKOJIMA
187 Development of Automatic Train Operation System Based on Intermittent Type ATP with Continuous Speed Checks H.FUJITA, T.NOMURA, T.AOYAGI, S.MORITA
193 Study of Anomalous Characteristics Exhibiting Between Fixing Force of Switch and Tongue Rail Opening Force S.SHIOMI, Y.OSHIMI, K.TSUBAKI, K.TAKASAKI, T.SATO
200 Evaluation of Material Properties of Pantograph Contact Strip by Microscopic Structure Model F.MORIMOTO, Y.KUBOTA
206 Moisture Behavior in Concrete Repaired by Patching Observed with Neutron Imaging H.SUZUKI, M.UEHARA, M.MIZUTA, Y.OTAKE
212 Effects of Rotational Conditions on Performance of Gear Unit Pinion Bearing K.TAKAHASHI, D.SUZUKI, T.NAGATOMO

SUMMARIES

- 218 Summaries of RTRI REPORT (in Japanese)

ANNUAL INDEX

- 222 Annual Index: Subjects Vol.63, No.1-No.3 (2022)

Editorial Board

Chairperson: Kimitoshi ASHIYA

Co-Chairperson: Toru MIYAUCHI

Editors: Shinya FUKAGAI, Ryohei IKEDA, Masateru IKEHATA, Yusuke KOBAYASHI, Minoru KONDO, Tatsuya KOYAMA, Nozomi NAGAMINE, Erimitsu SUZUKI, Tsutomu WATANABE

Copyright © 2022 Railway Technical Research Institute, Tokyo JAPAN All rights reserved.

Research and Development on Power Supply Systems for a Sustainable Society

Hidenori SHIGEEDA

Power Supply Technology Division

Carbon neutrality is a necessary goal as a countermeasure against climate change. Therefore, it has become more important to promote further energy saving and the use of energy storage systems in railway systems. Notwithstanding, falls in passenger traffic due to COVID-19 have had a significant impact on railway management, and reducing infrastructure maintenance costs has become an urgent issue. This paper presents recent research and development on power supply systems, especially for decarbonizing the railways and reducing resources required for maintenance of overhead contact line systems.

Key words: electric power supply system (EPSS), overhead contact line (OCL) equipment, sustainability, decarbonization, energy-saving, maintenance-saving

1. Introduction

At the United Nations Summit on Sustainable Development held in September 2015, Sustainable Development Goals (SDGs) were adopted as international goals for a sustainable and better world that should be achieved by 2030. This agenda included goals related to electricity and energy: “Affordable and Clean Energy” and “Climate Action”. To this end, in October 2020 Japan’s Prime Minister announced a decarbonization policy aimed at reducing greenhouse gas emissions, such as carbon dioxide (CO₂), to virtually zero by 2050. This accelerated the integration of active decarbonization plans into management policies, through ESG (Environment, Social, and Governance), including for railway operators.

To reduce the burden on the global environment, in “Research and Development Creating the Future of Railways — RESEARCH 2025” (current Master Plan from FY 2020 to FY 2024), RTRI has set the research task, “Low-carbon power feeding networks by coordinated power control” as part of the subject, “R&D toward the future of railways” (hereinafter, Future-Oriented Task) with a target of practically applying outcomes in about ten years from now. The research tasks in questions focus on electric power, which accounts for approx. 96% of energy consumption required for train operation in Japan, and in addition to “Reduction of energy consumed by rail-

ways”, which we have been working on for some time, it aims to reduce carbon by actively utilizing renewable energy from the power grid, external to the railway. For this reason, its major feature is to work on the construction of a method that enables coordinated control between railway energy storage systems (ESS) and the power grid (Fig. 1).

On the other hand, in terms of the domestic railway business environment, research also takes into account issues already predicted, including population decline due to declining birthrates and an aging population, a resulting decrease in passenger volumes, and the securing sufficient labor required for infrastructure maintenance. Nevertheless, since the COVID-19 pandemic outbreak in FY 2020, passenger volumes have declined faster than expected, and some predict that the effect of the pandemic will be prolonged. Thus, we are urgently required to provide R&D outcomes that raise the infrastructure sustainability by enabling resource reduction and selective allocation, such as life extension, maintenance-saving, and labor-saving by automating inspections in the maintenance of infrastructure including the EPSS.

RTRI has set the Future-Oriented Task, “Labor saving by digital maintenance” in the current Master Plan. We will work toward the construction of an integrated analysis platform for equipment status data and automatic diagnostic technology, in addition, will

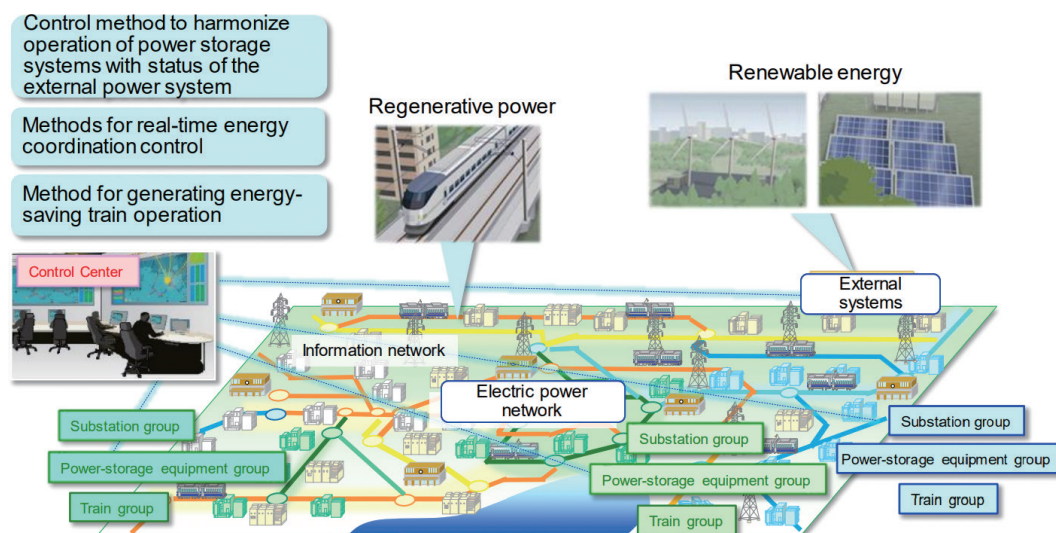


Fig. 1 Main efforts in “Low-carbon power feeding networks by coordinated power control”

promote the practical application of outcomes from the FY 2019 and earlier Master Plans, thereby providing effective outcomes to address the above needs.

This paper introduces R&D on decarbonization and R&D on maintenance labor-saving for OCL equipment.

2. R&D on decarbonization

2.1 Efforts required for decarbonization

The following is a non-exhaustive list of efforts made to achieve a decarbonized society: Energy suppliers increase the ratio of non-fossil energy, such as renewable energy and reduce CO₂ emission intensity associated with energy consumption, in addition, establish separation, capture, storage and other technologies for CO₂ emissions which are unavoidable.

The main efforts of consumers include controlling energy consumption by introducing energy-saving technology and, for users of fossil fuels, promoting the conversion to non-fossil fuels, for example, by electrification or hydrogen utilization. For suppliers to increase the ratio of variable renewable energies such as solar and wind power, the resilience of the power system is required to be strengthened, and consumers are required to have flexible adjustment capabilities such as load leveling and energy storage.

Most railway operators are consumers, and the decarbonization of railway operators with high electrification rates largely relies on the efforts of suppliers, but consumers should also steadily increase measures that can be rationally introduced, centering on energy-saving.

2.2 R&D on energy-saving

Regarding R&D for energy-saving in train operation, our past efforts regarding the EPSS include developing a high-voltage DC feeding system that applies power conversion technology [1] and making power utilization more efficient by applying energy storage technology and superconducting technology; in addition, we developed the Train Operation Power Simulator, which can quantitatively evaluate the effects of introducing these technologies [2].

The research task that we are currently working on, “Low-carbon power feeding networks by coordinated power control”, aims to establish an algorithm that assumes that the introduction of ICT enables high-speed ground-train and train-to-train communication. This algorithm will generate a train performance curve for each train, which should provide the most energy-saving performance in consideration of the utilization rate of regenerative energy, in real-time according to operating conditions. For example, if a train is delayed this may lead to other delays due to late departures or suspended operations and deceleration between stations because of signals, resulting in increased train operation time relative to the schedule. Figure 2 shows the energy-saving performance curve that was obtained when the maximum speed between stations was reduced by minimizing as much as possible the increase in stop time due to late departure or suspended operation and allocating that time to the time traveled between stations.

The Train Operation Power Simulator was used to estimate the substation power consumption for one hour, including the period during which delays were introduced. The results showed that the proposed method can reduce power consumption by approx. 1% to 2% [3].

Besides, we aim to propose a method for creating a schedule

that is expected to be the most energy-saving in consideration of the utilization rate of regenerative energy, assuming that the station-to-station section train operation time is allowed to be revised in creating the schedule. However, since revising train operating times may negatively impact passenger experience, we are aiming to achieve both energy-saving and ensure passenger convenience, while quantitatively evaluating the convenience.

We expect to reduce energy consumption by several percent compared to train operation energy based on the conventional timetable and train operating method by utilizing the above outcomes.

2.3 R&D on the utilization of ESSs

The Sixth Strategic Energy Plan, compiled by the Ministry of Economy, Trade and Industry, includes an ambitious outlook for the power generation mix in 2030 to raise the proportion of renewable energy to around 36% to 38%. It states that among renewable energies, solar power and wind power will account for around 15% and 6%, respectively; ensuring system coordination capabilities for these variable renewable energies will be increasingly important.

For railways in Japan, the introduction of ground-mounted or on-board ESSs is being promoted mainly for energy-saving applications by effectively using regenerative energy or for emergency running applications in the event of a power outage. In addition, the introduction of storage battery vehicles is in progress toward the electrification of railcars. There is also an example of introducing a large-capacity ESS for the purpose of peak shift, etc. of railway load.

In “Low-carbon power feeding networks by coordinated power control”, we are aiming to construct a system configuration and control method for ESSs of railways so that equipment for emergency running can be used for energy-saving or equipment for energy saving can be used for adjustment. This project also aims to establish a method for quantitatively evaluating the implementation impact of such measures and the effect on the life of equipment being used in this original way. Figure 3 shows an example of results of trial that were obtained from the example shown in Fig. 4, which includes a case where a large-capacity ESS installed in a substation is used for charging regenerative power and a case where it is also used for charging renewable energy connected to an AC system of the railway [4]. The conventional control, which charges only the regenerative power, reduces the amount of purchased power from the power company at the substation equipped with the ESS by 3.6 MWh compared to the case without an ESS. However, it reverses all renewable energy not consumable by the railway to the power company system. By contrast, the proposed control further reduces the amount of purchased power by 1.4 MWh by charging and utilizing renewable energy that was conventionally included in the reverse power flow.

By applying these results, we expect to improve the CO₂ reduction effect approx. 2 to 5 times relative to existing ESS.

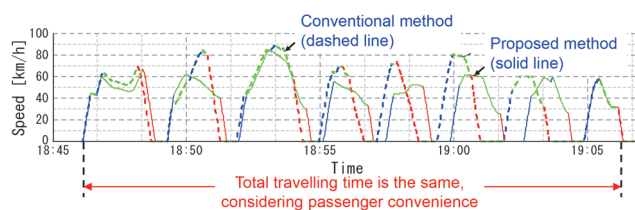


Fig. 2 Example of the energy-saving train performance curve when a delay occurs [3]

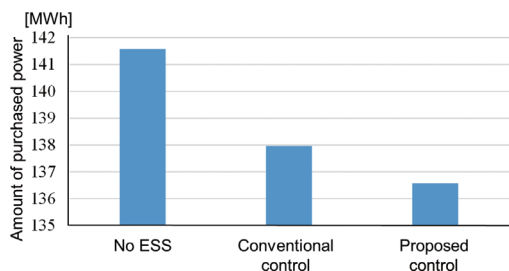


Fig. 3 Example of results of trial calculation of the amount of purchased power [4]

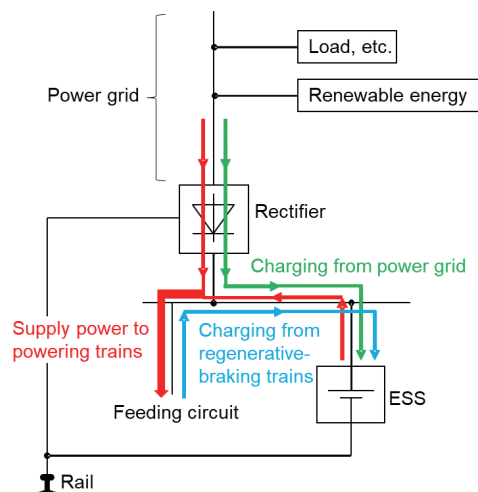


Fig. 4 Concept of charging and discharging of ESS [4]

3. R&D on maintenance labor-saving of OCL equipment

3.1 R&D on Life Extension and Maintenance Cycle Extension

OCL equipment is a single system, which requires high reliability. Therefore, it is important to prevent defects such as disconnection. In addition to regular patrols and inspection measurements, if equipment exhibits an anomaly, deterioration, or wear progress, it must be appropriately repaired, replaced, or handled otherwise. One of the issues with extending the life of equipment and the maintenance cycle is to reduce the wear of current collection materials such as contact wires and pantograph contact strips: we are working on basic research to elucidate the mechanisms underlying each type of wear, to propose measures for wear reduction.

To elucidate the wear phenomenon caused by the heat generated by energized contacts, we conducted a wear test using a direct-acting wear tester that can perform a sliding test with a constant contact force during energization, and also conducted a temperature analysis of the energized contacts; then, we created a current collection material energization wear type map (Fig. 5) [5]. In the figure, the vertical axis represents the contact voltage between the contact wire and contact strip, and the contact boundary coefficient on the horizontal axis represents the ratio of the electrical resistance including the surface coating resistance of the contact wire and contact strip. It shows that the type of wear due to heat generation of the energized contact clearly differs depending on the contact conditions. The differences among these types of wear are caused by the differences in melting point and electrical resistivity between the contact wire and contact strip.

Furthermore, to elucidate the wear phenomenon caused by

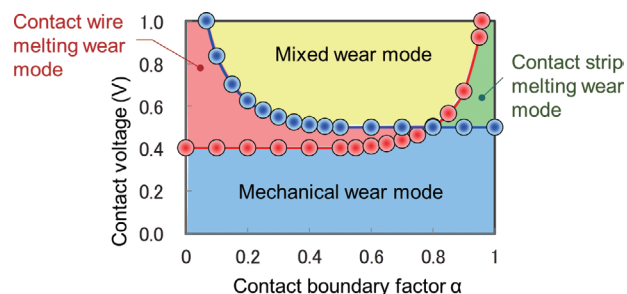


Fig. 5 Wear mode map under the effect of flowing electric current [5]

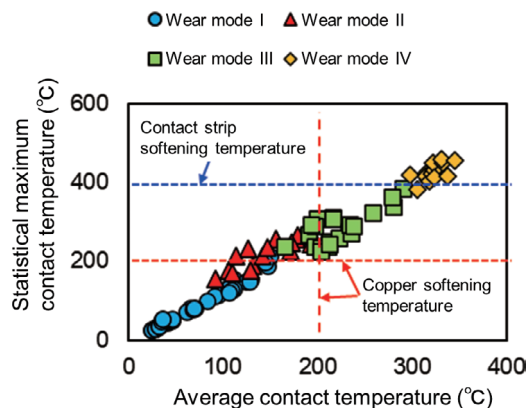


Fig. 6 Mechanical wear mode according to contact temperature [6]

frictional heat during sliding, we manufactured a rotary wear tester that can increase the sliding speed and measure the contact temperature. From the results of the wear test with this tester, the mechanical wear type was subdivided into four types according to the contact temperature (Fig. 6), clarifying the transition conditions of the respective wear types [6]. We will continue to work on the elucidation of the wear mechanism in consideration of the actual field conditions such as the internal temperature of the contact strip member, the zigzag deviation of the contact wire, and the effect of the train draft.

With regards to R&D that contributes to the reduction of salt damage countermeasures such as insulation strengthening and insulator cleaning, which are mainly performed in OCL equipment in coastal line sections, we constructed an insulator pollution degree estimation algorithm using public data on weather and topography [7]. Although the pollution classification was previously defined uniformly based on the distance from the coast, this method has enabled it to be subdivided, which is expected to lead to a review of maintenance in line with the actual conditions of each region.

3.2 R&D on automation of inspection

Regarding R&D on automation of OCL inspection measurement for the purpose of maintenance labor-saving, RTRI is working on anomaly detection of OCL metal fittings using image data acquired by the OCL non-contact measuring device [8] developed so far. As part of this, we have proposed an image normalization method using line position information [9]. When deforming an image of arbitrary size of a dropper or another extracted from image data to a constant size suitable for machine learning, this method deforms the image in a way which preserves information in the image near the

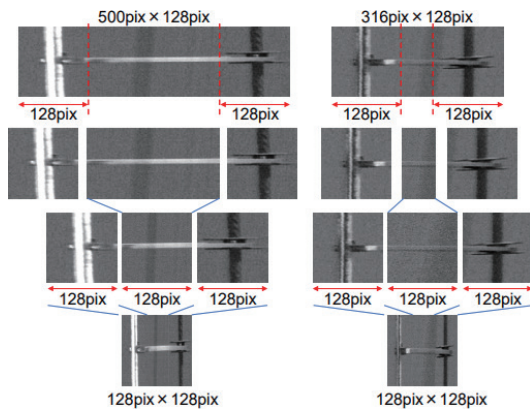


Fig. 7 Procedure for normalizing OCL metal fitting images [9]

connection with the line where abnormalities are likely to occur (Fig. 7).

We have obtained insight which suggests that anomaly detection accuracy can be improved by learning image data normalized by this method in unsupervised machine learning using a generative adversarial network.

Railway operators are conducting R&D on using unmanned aerial vehicles (drones) for OCL equipment inspection and image data collection. However, magnetic fields generated from OCLs or others may affect the flight control of drones. Especially on DC contact lines, a residual magnetic field is generated by magnetizing metal structures such as beams and steel pipe columns; this is thought to also affect flight during nighttime power outages. Therefore, RTRI has investigated the effect of the DC magnetic field on the flight control of drones and proposed the concept of flyable areas, based on the simulation of residual magnetic fields by the magnetization of metal structures [10].

4. Conclusions

This paper introduced R&D on decarbonization from the viewpoint of a Sustainable Global Environment and R&D on maintenance labor-saving of OCL equipment from the viewpoint of Sustainable Railway EPSS. In fact, these examples are only part of the various undertakings by RTRI for the realization of these targets. We will continue to work on original and innovative R&D for the sustainable development of railways and ask for the continued guidance and cooperation of railway operators and other related parties.

Author



Hidenori SHIGEEDA, Dr. Eng.
 Director, Head of Power Supply Technology
 Division
 Research Areas: Power Supply Systems

Acknowledgment

The research on the energy-saving train performance curve was financially supported in part by the Japanese Ministry of Land, Infrastructure and Transport.

References

- [1] Yoshii, T. and Oide, T., "DC-DC Converter Control Method for High Voltage DC Feeding System to Improve Use of Regenerative Power," *Quarterly Report of RTRI*, Vol. 63, No. 3, pp. 175-180, 2022.
- [2] Takeuchi, Y. et al., "Development and Verification of a Train Operation Power Simulator," *Proceedings of the 2017 IEE-Japan Industry Applications Society Conference*; 5-S8-9, 2017 (in Japanese).
- [3] Kunisaki, A. et al., "Energy-Saving Rescheduling Diagram by Adjusting the Running Time Based on the Amount of Change in Powering Energy," *Proceedings of the IEE-Japan TER / MSS Joint Technical Meeting*, TER-21-031 / MSS-21-024, 2021 (in Japanese).
- [4] Oide, T. and Konishi, T., "Absorption of Surplus Renewable Energy Output by Large Scale Energy Storage Connected to DC Feeder," *Proceedings of the 2021 IEE-Japan Industry Applications Society Conference*; 5-27, 2021 (in Japanese).
- [5] Yamashita, C., "Wear Mechanism of Current Collecting Materials under the Effect of Flowing Electric Current," *Quarterly Report of RTRI*, Vol. 58, No. 4, pp. 264-269, 2017.
- [6] Yamashita, C. and Nemoto, K., "Classification of Mechanical Wear Modes of Contact Wire and Contact Strip caused by Frictional Heat," *RTRI Report*, Vol. 35, No. 12, pp. 11-16, 2021 (in Japanese).
- [7] Usuki, T. and Shibata, N., "Method for Estimating Equivalent Salt Deposit Density on Insulator Surfaces Using Meteorological and Topographical Information Provided by Public Institutions," *Quarterly Report of RTRI*, Vol. 63, No. 3, pp. 163-168, 2022.
- [8] Matsumura, I. et al., "Measurement Accuracy Verification of OCL Contactless Measurement Device by On-board Test Run in Conventional Line," *RTRI Report*, Vol. 34, No. 9, pp. 11-16, 2020 (in Japanese).
- [9] Matsumura, I. and Nezu, K., "Study of Image Normalization Using Wire Position for Anomaly Detection of OCL fittings," *Proceedings of the 2021 Annual Meeting of The Institute of Electrical Engineers of Japan*, 5-191, 2021 (in Japanese).
- [10] Morita, G., Higuchi, K. and Sasakawa, T., "A Method of Estimating Flight Area for Unmanned Aircrafts Used for Inspection of DC Overhead Contact Line System," *RTRI Report*, Vol. 35, No. 12, pp. 17-22, 2021 (in Japanese).

Trend on Research and Development Activities Relating to Signalling and Telecommunication Systems in Railway Fields

Kunihiro KAWASAKI

Research & Development Promotion Division

The spread of new coronavirus infections (hereinafter referred to as COVID-19), which began in Japan at the end of 2019, has greatly affected railway business. There is an urgent need to reduce fixed costs while responding to changing needs for mobility in a post COVID-19 society. As such it is necessary to speed up research and development so that it can contribute to helping railway companies reduce fixed costs. This paper first introduces an overall picture of research and development related to the sophistication of automatic operation and its application to conventional railway lines. Secondly, it introduces ongoing research and development efforts related to the utilization of non-failsafe processors or a public communication network such as 5th Generation mobile communication systems (5G) for critical applications in the railway field. Finally, it presents the direction and policy of future research and development for equipment saving and cost reduction.

Key words: automatic operation, equipment saving, digital technology, 5G, autonomous train operation, COVID-19

1. Introduction

The spread of new coronavirus infections in Japan from the end of 2019 (hereinafter “COVID-19”) has greatly affected the country’s railways. Railway operators are trying to provide safe and convenient mobility while taking various infection control measures so that customers can this mode of transport with peace of mind. These conditions have increased the urgency of railway operators to reduce fixed costs while responding to changing needs for mobility in a post-COVID-19 society.

Our belief is that it is necessary to speed up R&D on cost reduction and equipment saving, which already forms part of RTRI’s research program, so that railway operators can contribute to future efforts to reduce fixed costs.

This paper introduces R&D for the advancement of automatic operation and expansion to general line sections, and R&D on cost reduction of signal communication equipment by using general-purpose technology and 5G. It also describes the direction and policy of future R&D for railway maintenance and development in a post-COVID-19 society.

2. R&D for automation of train operation

2.1 Issues with crew duties and automation of operation

According to Article 11 (on-board business, etc. of the staff who operate the motor vehicle) of the Ministerial Ordinance to Provide Technical Regulatory Standards on Railways, stipulated by the Ministry of Land, Infrastructure, Transport and Tourism (MLIT), staff on board trains can be divided into three categories: (1) staff for operating motor vehicles, (2) staff for train protection and those handling operational tasks, and (3) staff for passenger handling operations.

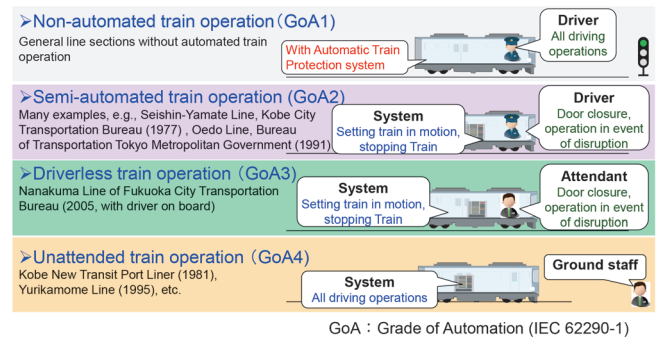
In the case of one-man operation, the driver plays the roles of these three staff categories alone, and in driverless operation, the staff member taking the place of the driver and the automated system play the roles of (1) to (3). Unmanned operation is a type of driverless operation in which no staff is on board the train and the

system and ground staff play the roles of (1) to (3).

There are several ways to realize automation of train operation, depending on the division of roles between people and systems. A ‘Grade of Automation’ (GoA) is used to determine the degree of automation in a railway train operation, which is defined by the international standard IEC 62290-1 (JIS E 3802) [1], which defines the requirements for urban railway commands and control systems (Fig. 1).

In Japan, GoA4 unmanned operation is realized on railway routes that have elevated structures without level crossings and have platform doors on the platform of each station, which prevents people accessing the tracks [2].

The MLIT established an Automatic Operation Technology Study Group on Railways (chaired by Prof. Koseki of the University of Tokyo Graduate School) in FY2018. This group is currently identifying technical issues with and examining the requirements for realizing automatic train operation for the grade above that in which a member of staff who is not qualified to operate a train is at the front of a train and tasked with ensuring automatic train operation in general line sections with level crossings (tentatively called GoA2.5 because it is between GoA2 and GoA3) [3]. Specific tech-



GoA3, 4: Currently put into practical use only in line sections without level crossings or lines where tracks are protected and cannot be accessed by passengers (e.g. subways, new transportation systems).

Fig. 1 Division of roles between people and systems in automatic operation

nical issues include safety monitoring of the track ahead and evacuation and guidance of passengers in the event of an anomaly.

2.2 R&D to support drivers and migration to driverless operation

This special issue contains the following four papers concerning the introduction and expansion of automatic operation and R&D to support drivers in one-man operations.

- (1) Development of an automatic operation system using ATSDK
- (2) Operation pattern generation technology for automatic acceleration/deceleration control assuming ATS-P
- (3) Train front obstacle detection method with a camera and LiDAR sensor integrated
- (4) Safety check method using vehicle side-mounted cameras

R&D (3) and (4) above make full use of digital technologies such as image processing and AI. The technology in R&D (3) will be indispensable for developing driverless operation in general line sections in the future. The technology in R&D (4) will be extendable to driverless operation although the goal is to support one-man operation.

The following sections briefly introduce some examples of research that could not be included in this special issue.

2.2.1 Detection of abnormalities inside level crossings using far-infrared images

Regarding the detection of motor vehicles on railroad crossings, in order to detect automobiles, railways have conventionally introduced systems that irradiate the inside of level crossings with a laser beam and those that use laser radar, etc.

These systems, however, have limitations. For example, they can only detect objects above a certain size, or have an undetectable range. Thus, RTRI has been developing a system capable of detecting objects smaller than cars (e.g. humans) in level crossings by processing thermal images taken by far-infrared cameras (Fig. 2) [4]. Initially, machine learning technology was applied, but issues were encountered involving processing volumes and machine learning. Therefore, by developing a technology capable of recognizing an object at high speed from the difference in time and space, a

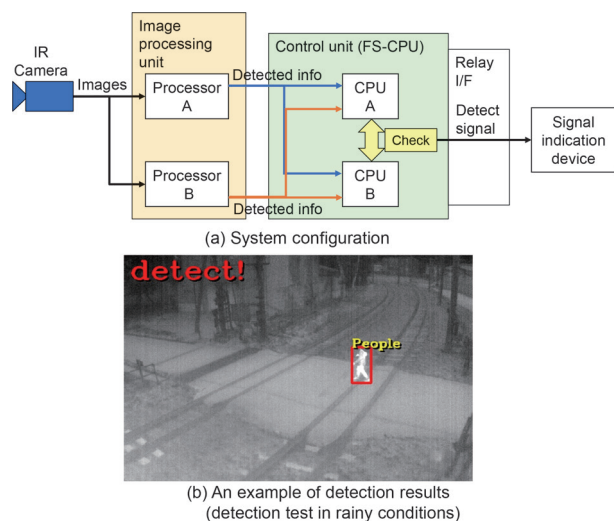


Fig. 2 Far-infrared image type detection of abnormalities inside level crossing

performance has been achieved that enables even the recognition of a person falling on the road. The processing system has been duplicated, and the reliability of the device has been improved by developing a mechanism to check the video output from the camera. The development of a prototype device designed for practical use was completed in the last fiscal year. Detection performance verification tests are currently underway in the field under various meteorological conditions. This method detects targets based on temperature difference: if the temperature of a target is close to the road surface temperature, the system may either not detect it or detect a false positive. We are now trying to quantitatively evaluate false negative detection probability, false-positive rates, etc. in various conditions, with a view to launching this into practical application in FY2022.

2.2.2 Detection of abnormalities inside level crossings using far-infrared images

Obstruction warning signals are devices which emit light in conjunction with an emergency button, etc. at a level crossing to notify the driver of an anomaly along the railway. On many routes, the driver visually sees the light emission and operates the brake to stop the train. We have developed the emission detection method of the flashing obstruction warning signal using an on-board camera so that safety can be further improved by supporting this visual recognition by the driver (Fig. 3) [5].

Our developed method uses an on-board camera equipped with an optical filter to shoot the front of the train and detects only the light emitted by the obstruction warning signal by image processing from the shot video. To separate the emitted light from other red flashing lights such as traffic lights in a short time, this method first quantifies the emission pattern of the obstruction warning signal shown in the video, then realizes detection by collating this with the contents of a database in which the emission pattern of the obstruction warning signal has been registered in advance.

We have experimentally verified that the light can be detected within 1 s after the obstruction warning signal located 600 m ahead emits light.

We are currently developing a device which can be mounted on a vehicle for practical use and could be put into service in FY2023 after conducting monitored runs on actual line sections in FY2022. We are also developing an algorithm applicable to rotary signals.

This method was developed as an element of the forward monitoring technology using a camera. Since the light emission is detected using a camera, the information can be left as a moving image, in addition, it is applicable and expandable to the detection of other objects such as the aspect of a signal.

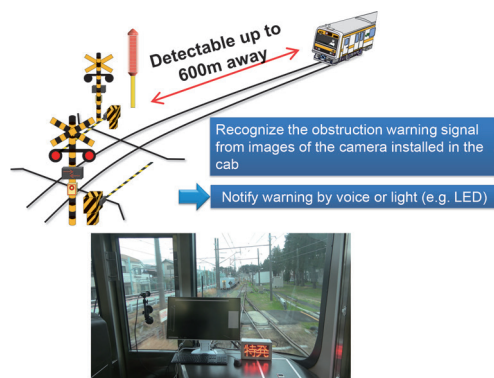


Fig. 3 Recognizing the light emitted from the obstruction warning signal with the on-board camera

3. R&D for equipment and cost reduction

To reduce fixed costs related to signal communication equipment, we should reduce the amount of necessary equipment as well as the equipment cost. To show technologies to reduce the equipment cost and the amount of equipment, this section overviews an example of configuring fail-safe devices with general-purpose processors and an example of R&D for applying 5G to security applications.

In FY2020, at an RTRI lecture [6] and in this journal [7], the concept of Autonomous Train Operation was introduced as a topic of R&D for the future of railways. It aims to reduce the amount of security equipment placed on the ground while making driverless operation, detailed in Section 2, even more sophisticated.

3.1 Configuring fail-safe devices with general-purpose processors

In railway signal systems, a basic requirement is to maintain the system in a safe state or ensure fail-safe functions in which the system transitions to a safe state in the event of a system failure. For this reason, even if using a relay, where contacts are dropped in the event of a failure or if using a computer, the system is configured with fail-safe devices that ensure the fail-safe properties of each input, processing, and output with a single device. However, since fail-safe devices are generally expensive, currently, a method has been studied for configuring security devices at a lower cost by using general-purpose processors, whose performance has improved remarkably in recent years.

When applying a general-purpose processor to a railway signal system, there are issues that (i) the device alone is not fail-safe, and (ii) the product life cycle is short, thus maintaining or renewing it is difficult within the life cycle of the entire system.

Therefore, we took the following steps: first, after organizing and defining the requirements for applying a general-purpose processor to safety-related processing, we proposed a flow to configure the system through the phase to perform safety analysis of the entire system and the phase to check safety requirements. Then, we proposed a configuration method that includes the first step of applying a general-purpose processor to the input/output section of a fail-safe device [8]. We also presented a framework for applying cryptographic techniques with fail-safe appliances for ensuring security, which is an issue when using general-purpose computers and public lines. In future, we will go one step further and proceed with R&D on a method for constructing a system using only general-purpose processors without relying on fail-safe devices.

3.2 Using 5G for security control

Regarding the application of 5G to railways, individual railway operators have already conducted demonstration experiments mainly on the improvement of passenger services in cooperation with telecommunications carriers. The provision of new services is about to begin. However, the application of 5G to safety-related information transmission such as train operation control has not been sufficiently studied or verified. If 5G is available for security use, standalone ground-to-train communication system can be replaced, in addition, this could simplify standalone ground networks.

Thus, in order to apply 5G to realize safer and more stable train operation including wireless train control and future automatic operation, we are working on R&D on the configuration of control systems that take advantage of the features of 5G, and conducting per-

formance evaluations on transmission reliability and delays.

In March 2021, on the RTRI in-house test line, we constructed a non-standalone (NSA) local 5G system using the 28 GHz band (Fig. 4). A standalone LTE system (standalone BWA) in the 2.5 GHz band has been introduced as an anchor for exchanging control signals between the base station and terminals. In addition to local 5G, we have obtained a license for a specified radio station for standalone LTE systems together, thus allowing comparison in transmission characteristics between local 5G and standalone LTE.

In the future, we will quantitatively grasp the 5G transmission characteristics in the railway environment and evaluate the reliability, delay, etc. We will prepare and propose a draft guideline for 5G utilization centered on railway train operation control by the end of FY 2021, taking into (i) the study on the Future Railway Mobile Communication System (FRMCS) being promoted by the International Union of Railways (UIC) and (ii) needs for railway operators in Japan.

4. R&D for a post-COVID-19 society

Since before the COVID-19 pandemic, we have been working on R&D to reduce fixed costs and realize train operation control that can flexibly respond to changing needs. We recognize that these efforts are important for maintaining and developing the railway also in a post-COVID-19 society. In particular, we believe that R&D must be further accelerated for technologies that directly lead to the reduction of fixed costs, such as automation of operation and equipment saving.

First of all, we will aim at reducing load and time related to driver decision-making, and further automation by developing methods which can exploit different types of data, apply latest data processing, and AI. Our research also aims to reduce costs and increase system and device reliability by designing rapid reliability/validity evaluation methods and methods for detecting abnormalities in processing results, which are needed to apply high-speed processor technology (e.g. general-purpose CPU and GPU used to apply AI) and wireless communication networks (e.g. 5th Generation Mobile Communication System (5G) in safety-critical work.

In addition, R&D will focus on preparing the transition to new systems that can help save labor, equipment, and energy by constructing a cross-sectoral data-sharing platform and achieving autonomous train operation.

Another goal is to share and disseminate research outcomes more rapidly. Currently, findings are often shared when practicality and reliability have been confirmed. However, it is important to disseminate results as soon as possible even when outcomes only

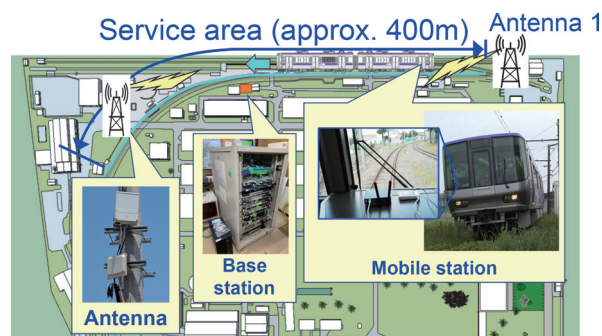


Fig. 4 Configuration of local 5G system deployed along the test track in RTRI

partially meet railway operator needs because they are still in performance. This is especially true for outcomes which involve new uses of digital technology: given that the development and obsolescence of base digital technology itself progresses rapidly, we should deliver developments to railway operators at an early stage to allow them to be sophisticated while being used. Nevertheless, the performance and effectiveness of findings do need to be verified in terms of safety and in relation to passenger satisfaction, which means that some R&D outcomes will still need to meet the traditional high criteria in terms of performance before they can be introduced in practice. This means that not all R&D outcomes will be dealt with uniformly, and only selected items of research will be proposed at an earlier stage in consultation with railway operators.

5. Conclusions

This paper introduced recent R&D that contributes to the automation of train operations and equipment saving. It also described the future direction and principles underpinning RTRI's approach to R&D aimed at adapting maintenance and development of railways in a post-COVID-19 society.

At present, while there are positive signs that it will be possible to live with COVID-19 with vaccines and treatments, long-term pandemic control measures are still required. As such R&D aims to help railway operators save labor and improve efficiency improvement, to enable them to continue operating trains on time every day against a background of dramatically altered mobility needs in a difficult business environment. It is also important for us to consider what technologies are required to respond to changes in people's transport and distribution patterns in a post-COVID-19 society and reflect them in future R&D. We will work diligently on R&D in collaboration with Japanese domestic and overseas railway operators and research institutes, manufacturers, and universities with advanced technologies so that we can contribute not only to the maintenance of railways as a social infrastructure, but also to its further development.

The R&D on 5G introduced herein was carried out in collabo-

ration with Hitachi, Ltd.

References

- [1] IEC 62290-1:2014, "Railway applications - Urban guided transport management and command/control systems - Part 1: System principles and fundamental concepts," IEC, 2014.
- [2] Mizuma, T., "History and Future of the Automatic Train Operation System in Railway field," *Journal of the Society of Instrument and Control Engineers*, Vol. 56, No. 2, pp. 93-98, 2017 (in Japanese).
- [3] The Ministry of Land, Infrastructure, Transport and Tourism, Automatic Operation Technology Study Group on Railways, https://www.mlit.go.jp/tetudo/tetudo_fr1_000058.html, 2021 (in Japanese).
- [4] Ichikawa, T., Nagamine, N., Mukojima, H., "Study on Evaluation Method of Anomaly Detection Algorithm for a Level Crossing," presented at the *Technical Meeting on "Transportation and Electric Railway"*, IEE Japan., May 13th, 2021, Paper TER-21-050 (in Japanese).
- [5] Mukojima, H., Nagamine, N., Nomura, T., Ichikawa, T., "Blinking Detection for Obstruction Warning Signal using Front Camera," *Quarterly Report of RTRI*, Vol. 62, No. 2, pp. 118-123, 2021.
- [6] Kawasaki, K., "Overview of Research and Development Activities Relating to Digitalization of Railway Operation Management and Future Outlook," *Quarterly Report of RTRI*, Vol. 61, No. 4, pp. 235-239, 2020.
- [7] Kawasaki, K., "Outlines and Future Outlook of Research and Development Activities relating to Utilization of Information and Communication Technology for Signalling and Telecommunication Systems," *Quarterly Report of RTRI*, Vol. 62, No. 2, pp. 83-87, 2021.
- [8] Gion, A., "Structure and Configuration Method for a Fail-Safe System using General Purpose Computers," *the Journal of Japanese Railway Engineers' Association*, Vol. 64, No. 8, pp. 12-15, 2021 (in Japanese).

Author



Kunihiro KAWASAKI
Principal Researcher, Research & Development Division
Research Areas: Radio Communication System, Radio Propagation, Electro Magnetic Compatibility

Research and Development Activities and Future Outlook in Materials Technology

Hiroshi UEDA

Materials Technology Division (Former)

Materials used in the railway system are required to maintain a designated performance over a predetermined period of time. Management of changes in these materials over time is therefore very important. Our current research focuses mainly on materials with a long serviceable life such as concrete and steel structures, and friction members such as rails, wheels, bearings, brake shoes, contact wires, and pantograph contact strips. We are also developing new materials or new technologies for the railway system. This paper outlines recent research and development activities in and the future outlook for materials technology.

Key words: materials for railway applications, clarification of phenomena, evaluation methods, countermeasures, new materials, development of materials

1. Introduction

The environment surrounding the railway sector has been undergoing major changes including major shifts in the use of railways due to the COVID-19 pandemic which has been spreading since FY2019, and the growing difficulty in recent years in recruiting staff for maintenance and other operations. Railway research and development must take this changing environment and other factors into consideration, when developing materials for the railways.

Railways are essentially a land-based guided transport system populated by vehicles which carry people and goods, requires a vast range of materials. Each material used is expected to deliver a required performance throughout its serviceable life to help support safe and undisrupted train operations.

Generally, although to varying degrees depending on their type, materials can break under excessive impact and other forces, as well as wear, snap, crack, peel, become brittle and experience other types of failure over time as they are exposed to cyclic loads, water, chemical substances, ultraviolet light and other influences. Proper management of material deterioration over time is thus critical for the safe and undisrupted operation of railway systems. Many of the past and current research and development projects naturally have been confronted with this fundamental issue.

Past projects produced a range of results including the extension of the service life of materials and the advancement of evaluation techniques and the associated updating of replacement intervals, contributing to reductions in cost and labor for material procurement, repair and parts replacements. These outcomes and other similar initiatives are expected to gain greater importance going forward as they contribute directly to further reducing costs and labor requirements in this new normal which must take into account the COVID-19 pandemic.

This paper presents an overview of RTRI research and development in the materials division including background to this work and its outlook.

2. Characteristics of materials for railway applications

2.1 Key areas requiring management of aged deterioration of materials for railway applications

Management of deterioration over time of materials used for

railway applications, as mentioned in Section 1, is important especially with respect to the following areas:

- 1) Long-term outdoor exposure to the elements,
- 2) Frictional sliding materials.

With regard to 1) above, civil structures, for example, are expected to last at least 100 years if maintained according to requirements including repair and reinforcement. Vehicles are not expected to be in service as long as civil structures, but still have longer service life than motor vehicles. Materials are generally more heavily impacted when used outdoors and subject to temperature change, solar irradiation and rainwater than when used indoors. These elements can often lead to deterioration of materials. For proper management of material wear, it is necessary to know the impact of these elements and control them accordingly.

As for 2), materials range widely and include wheels and rails, contact wires and pantographs, or axles and bearings. Railways are a system where vehicles run on the ground, which cannot be achieved without those and other frictional sliding materials on both the vehicles and the ground. Working in a harsh environment, those frictional sliding materials are more prone to wear, which affects their performance, and present many other issues specific to railways.

As such the RTRI makes these areas a higher priority among materials division activities.

In addition, the following area needs to be pursued by the materials division to help advance innovation in 1) and 2) above as well as develop new railway systems:

- 3) Development of new materials and technologies to achieve step changes in railway system progress.

2.2 R&D approach

To properly manage deterioration of materials because of ageing, it is essential to clarify the mechanisms and develop evaluation methods and countermeasures as shown in Fig. 1.

Possible approaches to executing those tasks include site investigations, experiments and simulations. Combining these approaches can improve understanding about what is going on in the field and these insights can be used to develop effective countermeasures. Rapidly advancing simulation technologies are now actively employed while at the same time equal efforts are being invested into field investigations and experiments, in the hope that synergies in this work will produce positive results.

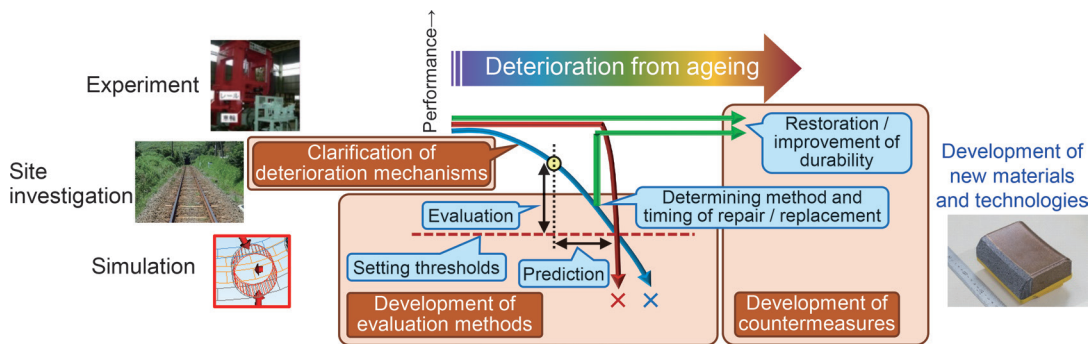


Fig. 1 Managing material deterioration over time [1]

3. Major research and development projects currently underway

Figure 2 shows some of the research and development projects in the materials field that are currently underway at RTRI. Covering a wide range of fields from vehicles, structures and tracks to ground facilities such as those related to power supply, signaling and communication, those projects are being conducted primarily by four laboratories specializing in concrete materials, vibration isolating materials, lubricating materials and frictional materials respectively and working in coordination with other relevant laboratories.

The projects presented here are grouped by phase into deterioration mechanisms clarification, evaluation methods development and countermeasures development, with each shown in the current phase of the project in the figure. Those currently in the phase where deterioration mechanisms are being clarified will either later or concurrently move to evaluation and countermeasure development phases. It is hoped that the results of this work will be adopted by railway operators.

3.1 Clarification of deterioration mechanisms

Clarification of deterioration mechanisms is essential in scientifically establishing phenomena occurring in the field and for devis-

ing countermeasures based on science. This in turn is extremely important for the continued growth of railways.

Reducing the wear of contact wires and strips is a key to reducing the cost of railway operations.

On Shinkansen lines, contact wire wear, which must be properly controlled by maintenance, is more significant in locations where the pantograph stops in stations than in high-speed running sections. In an attempt to clarify the phenomenon and come up with proposed countermeasures, an experiment is underway in which low-speed contact is simulated between a contact wire and a contact strip to observe wear (Fig. 3).

Traction motor bearings used on electric railcars and locomotives rotate at high speed while the train runs. If those bearings become damaged for any reason, safe and uninterrupted train operation may be compromised. To prevent damage to traction motor bearings, mechanism leading to damage must be clarified and a method for accurately evaluating the bearing life established. To that end, a program is currently underway that combines experiment and dynamic numerical simulation. Thus far, the program activities have included the designing of a test machine capable of collecting essential data and simulation modeling. The current plans include endurance test on bearings and simulation accuracy improvement, both of which are intended to help clarify factors that contribute to bearing

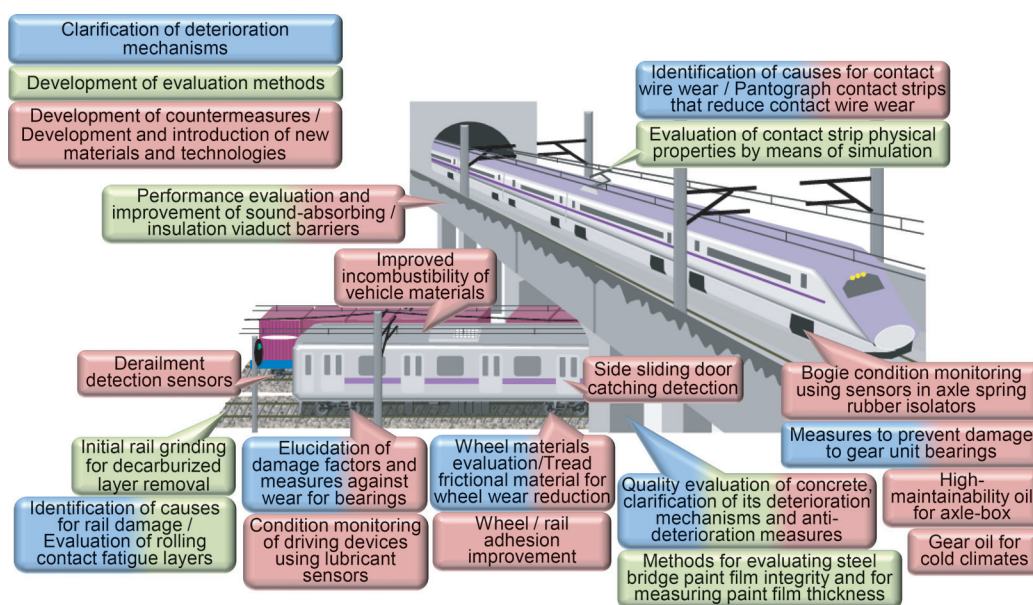


Fig. 2 Major research and development projects currently underway

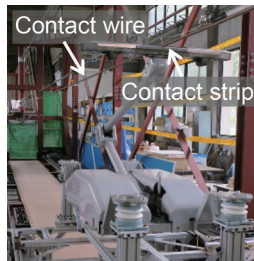


Fig. 3 Experiment on the impact of low-speed contact on contact wire wear

damage (Fig. 4).

Growing evidence suggests that the behavior of water plays a major role in the deterioration of concrete structures [2]. However, it has been difficult to measure the behavior of water in concrete and repair materials, which has been an obstacle to establishing systematic, relevant repair technology that factors in the effect of water. Consequently, a study is underway to visualize the penetration properties of water into concrete and repair materials using neutron beams to clarify the behavior of water (Fig. 5) [3]. Concurrently, research and development projects are being advanced on minimizing frost damage to improve the durability of concrete structures in cold regions.

3.2 Development of evaluation methods

Once developed, evaluation methods enable, among others, establishing the serviceable life limit of materials being evaluated as well as determining the performance level at the time of evaluation and the remaining time before the serviceable life limit is reached. All this information is useful in securing safe and undisrupted train operation and helps reduce cost through full use of materials over longer periods of time and optimization of replacement intervals for parts.

One of the methods available to diagnose the condition of engines and hydraulic torque converters on diesel railcars etc. is to measure the concentration of iron particles in the lubricating oil in those components. To simplify and facilitate the measurement process, a portable lubricating oil analyzer for iron particles was developed, enabling the measurement right next to the component being measured (Fig. 6) [4]. Currently, an onboard version of the analyzer is being developed.

Research and development programs on material simulation technology combine clarification of field phenomena and experiments, which is conducive to the development of more desirable materials. Currently, efforts are being made to develop a method for estimating the physical properties of pantograph contact strips through homogenization analysis using X-ray computed tomography image-based modeling. The method being developed has been found to achieve results closer to actual measurements than those obtained using the rule of mixture which states that the physical properties of a component material are proportional to the material's volume of fraction (Fig. 7) [5].

3.3 Development of countermeasures

While clarification of deterioration mechanisms and development of evaluation methods help improve daily operations in the field, the expertise gained from those efforts can be harnessed to develop countermeasures to directly achieve results. Currently at

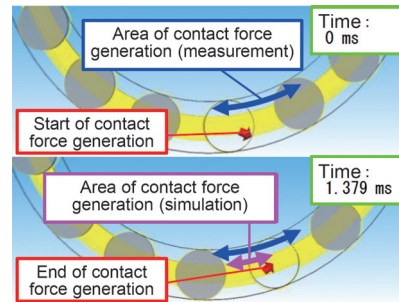


Fig. 4 Simulation of contact between roller and cage on traction motor bearing

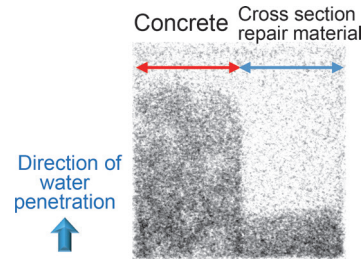


Fig. 5 Visualization of moisture penetration properties into concrete and repair material using neutron beams [3]

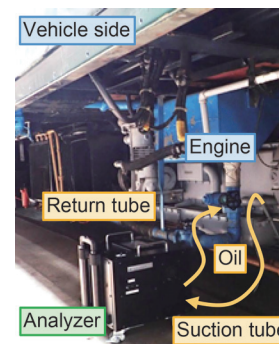


Fig. 6 Portable lubricating oil analyzer enabling measurement right next to the vehicle

RTRI, countermeasure development is underway on a number of subjects such as, as shown in Fig. 2, the development of multifunctional tread frictional material for wheel wear reduction [6], the development of oil for axle-box with improved maintainability and the development of a pantograph contact strip for contact wire wear reduction.

Today, it is essential to actively adopt rapidly advancing information and communications technology. One way the materials field and related technology can accelerate this process is to develop and offer sensor materials. Currently, for further enhancement of safety, a project is underway to develop a pinch detection system whereby sensors integrated within the side sliding door stop rubbers detect any object such as a string when it is pinched between the doors to prevent dragging incidents (Fig. 8) [7]. In another ongoing development project, a sensor using piezoelectric material is installed in the rubber isolator on an axle spring to detect occurring damage early to the axle journal bearing [8]. The sensor has shown the potential of meeting expectations (Fig. 9). Generally, installing additional sensors increases data input volumes while at the same

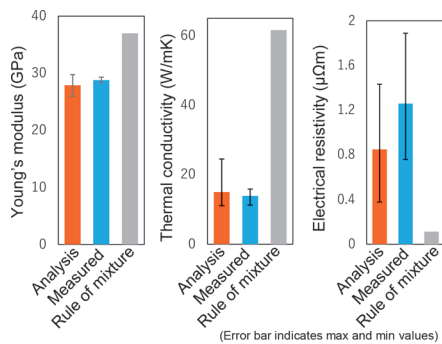


Fig. 7 Evaluation of physical properties of contact strips by microscopic structure model simulation [5]

time increasing the risk of installed sensors becoming loose and falling. In the examples cited above, however, the sensors are assembled within the existing components, eliminating the chances of them falling. It is hoped that this arrangement for sensor installation will be useful in a coming age of sensing technology.

4. Conclusion

Various kinds of materials are used for railway applications. To ensure that the materials used deliver the expected performance throughout their service life, it is important to properly manage deterioration of materials over time, with the help of continuously updated, relevant technology. In addition, the development of new materials and technologies holds the key to continuous technological innovation, to achieve step changes in railway system improvement. RTRI is dedicated to studying and developing materials for railway applications to help further improve safety, save labor, reduce cost, protect the environment and achieve other goals set, for a rapidly changing business environment conscious of future needs.

References

[1] Ueda, H., "Latest Research and Development in Materials Technology," *Quarterly Report of RTRI*, Vol. 62, No. 3, pp. 159-162, 2021.
 [2] Ueda, H. et al., "Durability Design Method Considering Reinforcement Corrosion due to Water Penetration," *Journal of Advanced Concrete Technology*, Vol. 18, pp. 27-38, 2020.

Author



Hiroshi UEDA, Dr. Eng.
 Director, Head of Materials Technology Division (Former)
 Research Areas: Durability of Concrete and Related Materials

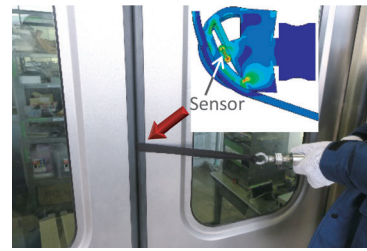


Fig. 8 Development of pinch detection system

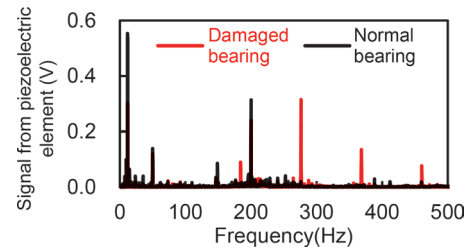


Fig. 9 Damage detection using axle spring rubber isolator

[3] Suzuki, H. et al., "Moisture Behavior in Concrete Repaired by Patching Observed with Neutron Imaging," *Quarterly Report of RTRI*, Vol. 63, No. 3, pp. 206-211, 2022.
 [4] Suzumura, J. et al., "Abnormality Diagnosis of Diesel Engines and Hydraulic Torque Converters by using Portable Lubricating Oil Analyzer," *RTRI Report*, Vol. 34, No. 10, pp. 29-34, 2020 (in Japanese).
 [5] Morimoto, F., Kubota, Y., "Evaluation of Material Properties of Pantograph Contact Strip by Microscopic Structure Model," *Quarterly Report of RTRI*, Vol. 63, No. 3, pp. 200-205, 2022.
 [6] Handa, K. et al., "Development of Improved Wheel Friction Block with Integrated Flange Lubrication and Tread Adhesion Functions," *Quarterly Report of RTRI*, Vol. 62, No. 3, pp. 197-200, 2021.
 [7] Mamada, S. et al., "Pinch Detection System for Door Edge of Rolling Stock Using Door Edge Rubber Containing Pressure Sensor," *RTRI Report*, Vol. 34, No. 10, pp. 23-28, 2020 (in Japanese).
 [8] Mamada, S. et al., "Sensing Technology Using Piezoelectric Rubber for Railways," *RTRI Report*, Vol. 32, No. 10, pp. 11-16, 2018 (in Japanese).

Method for Estimating Equivalent Salt Deposit Density on Insulator Surfaces Using Meteorological and Topographical Information Provided by Public Institutions

Tadanori USUKI

Current Collection Maintenance Laboratory, Power Supply Technology Division

Naoki SHIBATA

Power Supply Systems Laboratory, Power Supply Technology Division

Traditionally, the design and maintenance of electric power facilities of electric railways in bay areas have been carried out according to a uniform classification of pollution based on distance from the coast and other factors. In order to improve the safety of these facilities and save labor for maintenance, it is necessary to subdivide this uniform classification according to the actual pollution situation. Therefore, we propose a method for estimating the Equivalent Salt Deposit Density on insulator surfaces at any point on an open section using meteorological and topographical information provided by public institutions.

Key words: insulator, ESDD, estimating method, meteorological, topographical, open data

1. Introduction

An insulator is a component that provides electrical isolation between parts with different potentials, e.g. live parts and the earth. There are few cases of power transmission failures due to polluted insulation since an insulator is designed or maintained to ensure adequate insulation. On the other hand, if actual pollution is less than expected, an insulator may have been over-designed and over-maintained. It is therefore necessary to review current pollution classification from the viewpoint of both designing equipment suitable for the actual state of pollution and saving labor for maintenance. However, in order to achieve this, it would be required to measure pollution levels densely, and frequently over a wide area and accumulate data over several years.

A method for measuring the degree of pollution of an insulator widely used in Japan is to measure the amount of pollution (mainly sea salt) on the surface of an insulator by wiping it with gauze. However, it is difficult to obtain a sufficient amount of data for reviewing the pollution classification with the above-mentioned method, since a lot of labor is required for each data acquisition. In addition, there is an issue that the measurement results depend on the weather conditions immediately before the measurement and the proficiency of the measurer.

So far, the authors have surveyed reports [1-3] about measurements and simulations of sea salt particles on power transmission line insulators, conducted by electric utility companies in the past. Using these reports, we developed a method for estimating change in pollution over time for railway electric power facilities [4, 5], which are more sensitive to the surrounding environment as they are lower than transmission lines. In this proposed estimation method, meteorological information published by the Japan Meteorological Agency (hereinafter JMA) and topographical information published by the Geospatial Information Authority of Japan (hereinafter GSI) are used as input data. This method makes it possible to estimate changes in the Equivalent Salt Deposit Density (ESDD) as a degree of pollution over time at any point in an open section. This report provides an overview of the proposed methodology and the estimation accuracy.

2. Method for estimating ESDD on insulator surfaces

2.1 Model for transport and deposit of sea salt

Based on the investigations carried out by the Electric Technology Research Association on generation, transport, deposit and shedding of sea salt particles, as well as other literature reviews, we have developed a model for the transport and deposit of sea salt particles (hereinafter sea salt) as shown in Fig. 1. This model (Fig. 1) explains how sea salt generated at sea or along the coast is carried inland by wind, adheres to electrical equipment, and is washed away by rainfall. Each of the estimation equations corresponding to A) through E) in Fig. 1 is restated in equations (1) through (6).

A) density of sea salt in the air near the coast C_0

$$C_0 = \alpha \times W_0^2 \quad (1)$$

where C_0 : the density of sea salt in the air per unit volume near the coast (mg/cm^3);

α : coefficient; and

W_0 : wind speed near the coast at 10 m above sea level (m/s).

B) wind speed near the coast at 10m above sea level W_0

$$w = W \times \left(\frac{h}{H} \right)^p \quad (2)$$

where w : wind speed at local equipment height (m/s);

W : wind speed in meteorological data (m/s);

h : height of wind speed to be calculated (m) = 10 m;

H : height of wind speed measuring points in meteorological data (m); and

p : surrounding environment coefficient (big cities = about 0.5, general residential area and forest = about 0.25, on the sea = about 0.14).

$$\therefore W_0 = W \times \left(\frac{10}{H} \right)^{0.14} \quad (3)$$

C) salt density in the air C decreases with distance from shore

$$C = C_0 \times l^x \quad (4)$$

where C : density of sea salt in the air at a distance of l (km) from the coast (m/s);
 l : distance from the coast (km); and
 x : coefficient.

D) density of salt deposit on equipment per unit time M

$$M = \beta \times C \times w \quad (5)$$

where M : density of sea salt deposition per unit time (mg/cm^2);
 β : coefficient; and
 w : wind speed at local equipment height (m/s).

E) shedding by rain R

$$M' = M \times (1 - R^y) \quad (6)$$

where M' : density of sea salt deposition per unit time subject to washing by rainfall (mg/cm^2);
 R : total rainfall in the last 1 hour (mm/h); and
 y : coefficient.

2.2 Algorithm for ESDD estimation

As shown in section 2.1, each of the equations given in Fig. 1 is simple. However, since they are interrelated, there are several possible estimation algorithms to derive ESDD estimates. Furthermore, some of the equations contain unknown coefficients. For this reason, the estimation algorithm and unknown coefficients were determined by repeating the calculation of each of the equations given in Fig. 1 until the correlation coefficient between measured ESDD values and the estimated ones reached the maximum. The main characteristics of the measured data used to determine the algorithm are shown in Table 1. The meteorological information used as input data was taken from the data of the JMA observation points closest to the es-

timated points from the JMA website. Note that topographical information was taken from the GSI website.

The algorithm for ESDD estimation is shown in Fig. 2. The algorithm uses meteorological and topographical data to estimate the degree of ESDD at any point in an open section at any given time in the past. The meteorological and topographical information used as input are as follows:

Wind speed, wind direction: average of last 1 hour

Rainfall: total rainfall in last 1 hour, and

Topographical information: 16 azimuthal distances from the coast at estimated point, surrounding environment coefficient.

Table 1 Main characteristics of the measured data used to determine the algorithm

| | |
|-----------------------|--------------------------------|
| Measuring location | 5 places in Japan |
| Measuring period | 2 to 5 years |
| Number of data | About 120 |
| Min.ESDD (lower side) | 0.0022 mg/cm^2 |
| Max.ESDD (lower side) | 0.2119 mg/cm^2 |

3. Verification of estimation accuracy

3.1 Verification of estimation accuracy at multiple locations

In order to obtain estimates of the ESDD densely over a wide area, it is necessary to verify that the application of the same method is effective at any point. Table 2 shows the locations where the ESDD for verification was measured with the actual insulator. Note that the locations in Table 2 are different from the location where the data for algorithm determination were obtained. The upper and lower sides of the insulator are shown in Fig. 3. Measurements of ESDD were carried out on both sides using conventional methods (wiping the pollution with gauze).

Table 3 shows the categories and their definition (ESDD) in

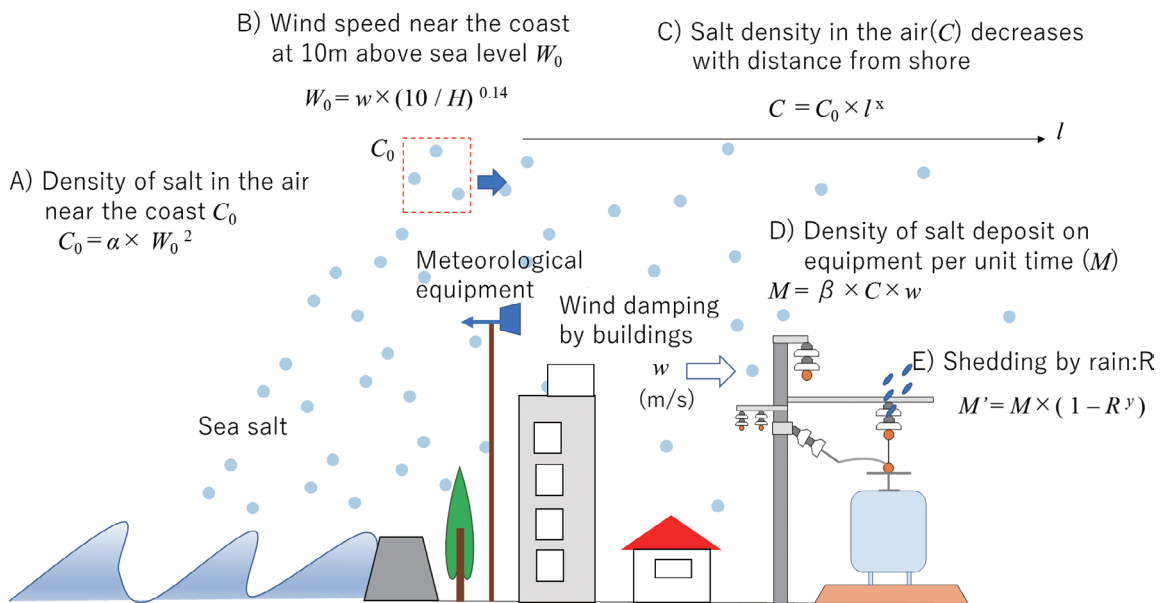


Fig. 1 Model for transport and deposit of sea salt

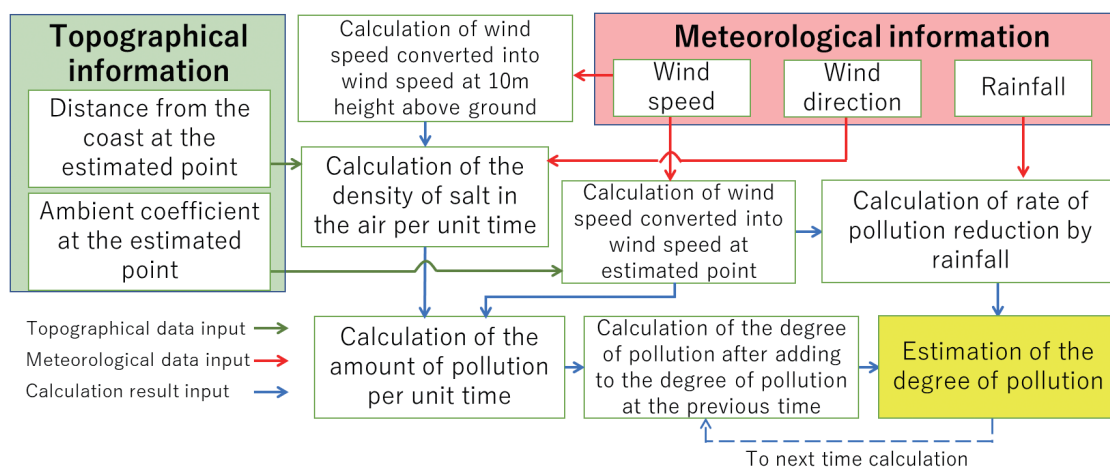


Fig. 2 Algorithm for ESDD estimation

Table 2 Locations of measurement

| Company | Lines | Location characteristics |
|---------|-------|--------------------------|
| A | A-1 | From coast to inland |
| B | B-1 | On the sea |
| | B-2 | From coast to inland |
| C | C-1 | Inland |
| | C-2 | Coast |

Table 3 Categories and their definition(ESDD)

| Categories | Equivalent Salt Deposit Density, ESDD |
|------------|--|
| Grade 1 | Under 0.01 mg/cm ² |
| Grade 2 | Over 0.01 mg/cm ² under 0.03 mg/cm ² |
| Grade 3 | Over 0.03 mg/cm ² under 0.06 mg/cm ² |
| Grade 4 | Over 0.06 mg/cm ² under 0.12 mg/cm ² |
| Grade 5 | Over 0.12 mg/cm ² under 0.35 mg/cm ² |
| Grade 6 | Over 0.35 mg/cm ² |

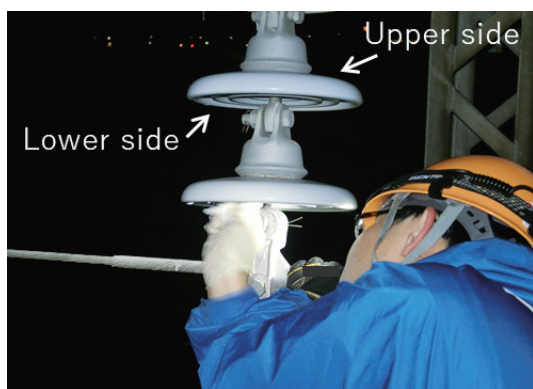


Fig. 3 Upper and lower sides of insulator

Ref. 2, and Fig. 4 shows measurement results of ESDD. Even the maximum ESDD on the lower side, which is prone to pollution, had a measured value classified as Grade 3. Figure 5 shows a comparison of the estimated values with the measured values shown in Fig. 4. The determination coefficient between the measured and estimated values R^2 for the upper side is 0.62, while the determination coefficient R^2 for the lower side is 0.72. As a result, it was found that there is a high correlation between the measured and estimated values. Furthermore, since the slope of the approximate straight line for the lower side is almost 1, the estimation of the ESDD up to Grade 3 is generally appropriate.

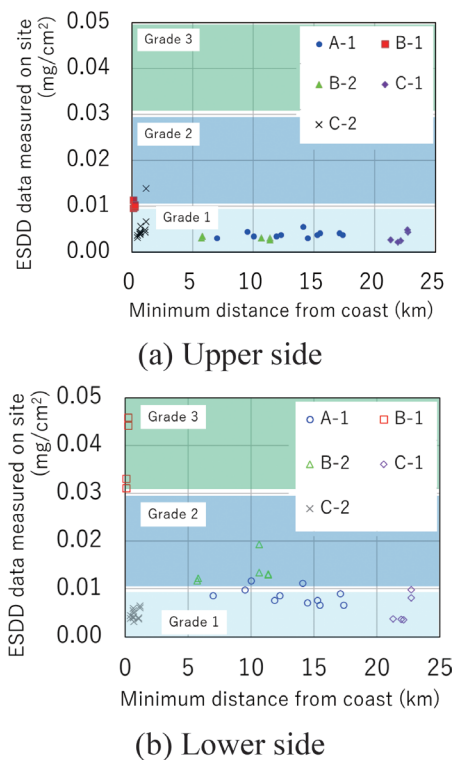
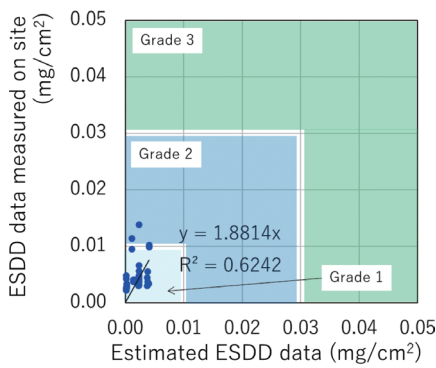
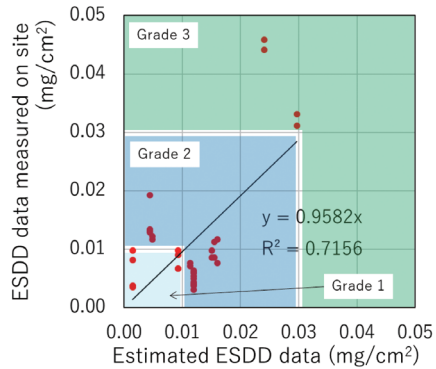


Fig. 4 Measurement results of ESDD



(a) Upper side



(b) Lower side

Fig. 5 Comparison of the estimated values with the measured values

3.2 Verification of estimation accuracy by using ESDD of the Anti-Salt Testing Station

As described in section 3.1, it was confirmed that the proposed method is generally correct. However, it was not possible to verify the method in a way which included highly polluted areas. In order to verify the accuracy of the proposed method in highly polluted areas, we attempted its verification using data obtained at the anti-salt testing station where we can obtain a large amount of data on high levels of pollution.

The locations of the anti-salt testing station and the JMA station closest to the test site are shown in Fig. 6. Both of them face the Sea of Japan and are about 10 km apart in a straight line. Figure 7 shows the estimated values (lower side) and measured values (lower side) in 2019 at the anti-salt testing station. At the testing station, high

levels of ESDD are expected in winter and the estimated results showed a peak in ESDD in winter, so that the trend is consistent.

Plots of the measured values and estimated values for the three-year period 2018 to 2020 at the anti-salt testing station, by frequency of occurrence, are shown in Fig. 8(a). In Fig. 8(a), it was confirmed that the 5% frequency of occurrence value of the approximate line of the measured values and the 5% frequency of occurrence value calculated from the estimated values roughly match. In addition, the same estimation method was used to verify the results at another location (facing a bay). The results are shown in Fig. 8(b). In the same way as the results of the anti-salt testing station, the 5% frequency of occurrence measured ESDD and the 5% frequency of occurrence estimated ESDD also roughly matched. Therefore, it is concluded that the proposed method has an estimation accuracy applicable to ESDD setting at any point.

4. Examples of the use of estimation methods

By using this method, it is possible to obtain the frequency of occurrence of ESDD for any point as shown in Fig. 8. Therefore, areas with a wide range of uniform pollution categories can be subdivided into categories that match the actual situation of pollution. This will lead to carrying out design and maintenance in accordance with the actual situation. As a result, this can contribute to optimization of insulation co-ordination and labor-saving maintenance.

An example of pollution category subdivision using the proposed method is shown in Fig. 9. First, select the point you want to estimate. Here, the estimation point is the location closest to the coast between one station and the next station. Second, collect topographical information on the estimated point and meteorological information for any period. Here, we have collected about 10 years

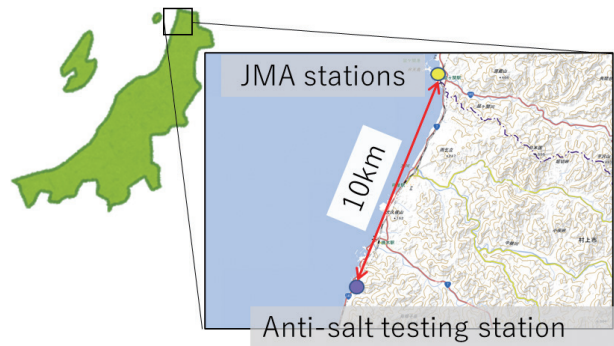


Fig. 6 Location of the anti-salt testing station and the closest JMA station

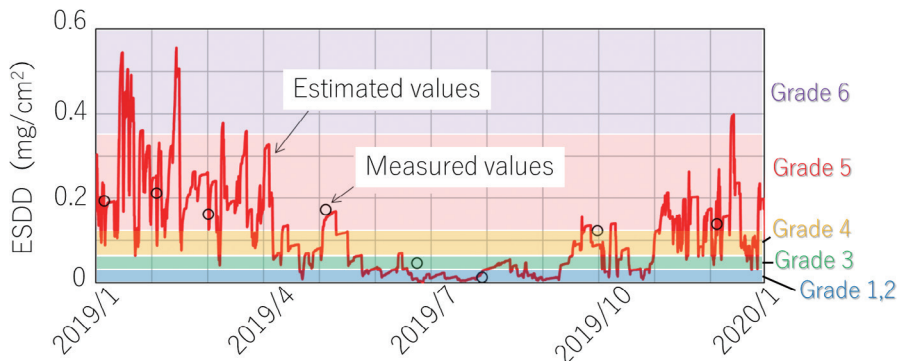


Fig. 7 Results of the estimated and measured values (both of lower side) in 2019 at the anti-salt testing station

of meteorological information. Third, calculate ESDD (5% frequency of occurrence) at the selected point. And fourth, classify the estimated results (ESDD) according to the categories shown in Table 3. Figure 9(a) shows the current categories where all sections are currently set as “sections where salt pollution is considered”. On the other hand, the results of subdividing the classification into areas with a low and high risk of pollution according to the estimated degree of pollution by the proposed method are shown in Fig. 9(b). In this case study, the estimated point was closest from the coast between one station and the next station. The proposed method can estimate the ESDD on each mast instead of between one station and the next station.

5. Conclusions

We proposed an estimating method of ESDD on insulator sur-

face at any point in an open section using meteorological and topographical information provided by public institutions. The research findings are as follows:

- Results confirmed that estimated values using the proposed method roughly matched measured values.
- It was confirmed that the proposed estimation method can be applied to any point.
- The measured and estimated ESDD (5% frequency of occurrence) roughly matched. Therefore, it is concluded that the method has the estimation accuracy that is applicable to the ESDD setting at any point in an open section.
- By using the proposed method, it is possible to design and maintain insulators according to actual pollution conditions. This makes it possible to improve safety, as well as optimize insulation coordination and save labor for maintenance.

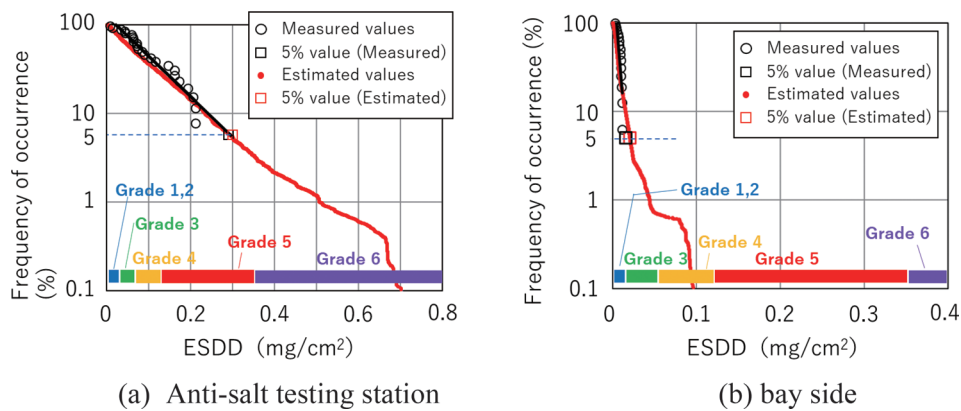


Fig. 8 Relationship between ESDD and frequency of occurrence

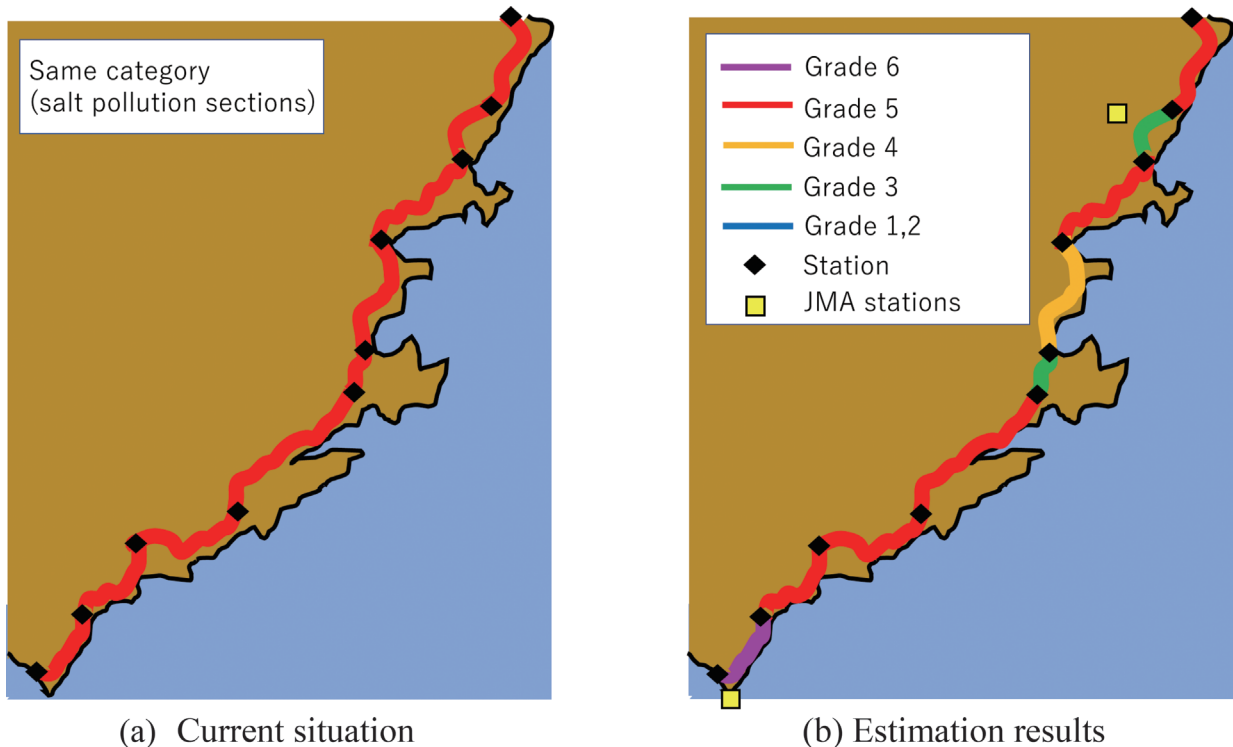


Fig. 9 Examples of subdivisions

References

- [1] Electric Technology Research, Salt damage prevention for power distribution equipment, Electric Technology Research Association, Vol. 20, No. 1, 1964 (in Japanese).
- [2] Electric Technology Research, Quantitative evaluation of degradation environment for power distribution equipment, Electric Technology Research Association, Vol. 69, No. 3, 2013 (in Japanese).
- [3] Electric Technology Research, Measures to improve salt resistance of power distribution equipment, Electric Technology Research Association, Vol. 51, No. 3, 1996 (in Japanese).
- [4] Shibata, N., and Usuki, T., "Study on the salt deposition density estimated by meteorological data and the corrosion reduction of steel plates exposed to actual conditions," Proceedings of the 67th Japan Conference on Materials and Environments, B-303, pp. 157-160, 2020 (in Japanese).
- [5] Usuki, T., and Shibata, N., "Accuracy Validation of Estimating Method of Insulator Pollution Degree Using Meteorological and Topographical Information Provided by Public Institutions," 2021 IEE-Japan Industry Applications Society Conference, 5-47, pp. V-273-V-276, 2021 (in Japanese).

Authors



Tadanori USUKI
Senior Researcher, Current Collection
Maintenance Laboratory, Power Supply
Technology Division
Research Areas: Corrosion of Overhead
Contact Line Materials



Naoki SHIBATA
Assistant Senior Researcher, Power Supply
Systems Laboratory, Power Supply
Technology Division
Research Areas: Power Supply Systems

Exposition of Revision of Seismic Design Guideline for Overhead Contact Systems

Yuichi KONDO

Contact Line Structures Laboratory, Power Supply Technology Division

In Japan, in order to prevent supports (referred to poles and portal structure etc.) in overhead contact systems from collapsing at the time of an earthquake, we design them according to the Seismic Design Guideline for Overhead Contact Systems and Commentary (hereafter referred to as the OCS Guideline).

We revised the OCS Guideline in 2013 to evaluate seismic performance of supports more precisely. The paper shows the process of revising OCS Guideline until now and details of the latest revision of the OCS Guideline.

Key words: earthquake, railway structure, Overhead Contact System, seismic design, supports

This paper is published in STECH2015 No. 3 E23, © 2015 by the Japan Society of Mechanical Engineers, November 9, 2015.

1. Introduction

Japan is one of countries affected by earthquakes frequently. We need to design railway structures adequately so that earthquakes of higher magnitude do not cause serious damage to them, such as destruction of viaducts and collapse of supports (referred to poles and portal structure etc.) in overhead contact systems. International Electrotechnical Commission (IEC) does not describe any seismic design methods of supports in overhead contact systems. Incidentally, in Japan, we established the Seismic Design Guideline for Overhead Contact Systems and Commentary (hereafter referred to as the OCS Guideline) in 1982 [1] and the Design Standard for Railway Structures of Seismic Design and Commentary (hereafter referred to as the Seismic Standard) in 1999 [2]. We design supports according to the OCS Guideline and railway structures according to the Seismic Standard including civil engineering structures.

The Seismic Standard, revised in 2012, additionally includes new design ground motion and a method of inputting waves into overhead contact systems and station buildings on civil engineering structures when estimating their dynamic behavior [3]. In order to maintain consistency with the Seismic Standard, we revised the OCS Guideline in 2013 [4]. The paper shows the process of revising OCS Guideline until now and details of the latest revision of the OCS Guideline.

2. Establishment and revision of OCS Guideline

2.1 Establishment of the OCS Guideline

In the past we had designed supports used in overhead contact systems mainly to resist wind pressure. However, in the 1978 MIYAGI-KEN-OKI Earthquake, many concrete supports in overhead contact systems, which were installed under construction of Tohoku Shinkansen line, were damaged. Therefore, in 1982 we established the OCS Guideline that describes the design method for preventing collapse of the supports by an earthquake. In 1978, supports on earth structures were hardly damaged, and most of the damaged supports were on viaducts. Thus, the OCS Guideline describes the design method in consideration of the effect of the dynamic behavior between supports and civil engineering structures.

2.2 Revision of the OCS Guideline in the past

The 1995 Great Hanshin-Awaji Prefecture Earthquake seriously damaged civil engineering structures. Therefore, the seismic design method for civil engineering structures has been modified and the seismic force to which civil engineering structures are subjected has been substantially modified. Since we designed supports on civil engineering structures using this force basically, the OCS Guideline was also modified in 1997 [5].

2.3 Latest revision of the OCS Guideline

In 2012, the Seismic Standard was revised accordingly since the international standers were changed to performance regulations. In consideration of the ground motion and damage at the 2011 Great East Japan Earthquake, the Seismic Standard additionally included new design ground motion and a method of inputting waves into overhead contact systems and station buildings on civil engineering structures when estimating their dynamic behavior. In order to maintain consistency with the Seismic Standard, we revised the OCS Guideline in 2013. The revised OCS Guideline included new knowledge to make more precise evaluation of seismic performances.

3. Outline of the seismic design method of supports in overhead contact systems

According to the analysis of the damage in the past earthquakes, we found that many supports were damaged in case they resonated with civil engineering structures at the time of the earthquakes. Therefore, we have to design supports in consideration of the vibration property of both supports and civil engineering structures.

There are methods using a unified model and a separated model as the seismic design method of supports on civil engineering structures. Figure 1 shows a concept of the unified model and the separated model. In case of the unified model based on the consideration of unifying supports and civil engineering structures, we evaluate the response acceleration of supports to the ground motion. However, it is difficult and complex to evaluate the response acceleration of supports. On the other hand, the separated model is easy to evaluate

the response acceleration of supports but cannot evaluate the dynamic behavior between supports and civil engineering structures. Therefore, we compensate the effect of the dynamic behavior to adopt the separated model.

4. Details of latest revision of the OCS Guideline

The OCS Guideline describes the seismic design method of supports on viaducts and those on the earth structures. Since the seismic design method of supports on viaducts was mainly revised in 2013, we show it as an example and explain the details of revision of the OCS Guideline.

4.1 Procedure of the seismic design method of supports on viaducts

Figure 2 shows the procedure of the seismic design method of a support on a viaduct. In this case, we assume that design parameters of the viaduct were evaluated when the viaduct was designed. First, we evaluate the response wave of the crown of the viaduct to the ground motion. Second, we input this wave into the foundation of the support and evaluate the response acceleration of the support. Third, we evaluate the maximum moment of the support generated by this acceleration. Last, we compare the maximum moment of the support with its limit moment to evaluate the safety.

4.2 Ground motion to be considered

In the Seismic Standard, the design ground motion consists of L1 earthquake ground motion and L2 earthquake ground motion. L1 earthquake ground motion means the ground motion having a high possibility of occurrence, among those expected to occur at that place, judging from the relationship between the recurrence intervals of earthquake ground motion and the design working life of the viaduct concerned. L2 earthquake ground motion means the ground motion having an intensity of the maximum scale among those expected to occur at that place. In the OCS Guideline, the target is that supports in overhead contact systems do not cause destruction or collapse so that serious troubles for train run do not occur. Therefore, the ground motion to be considered is L2 earthquake ground

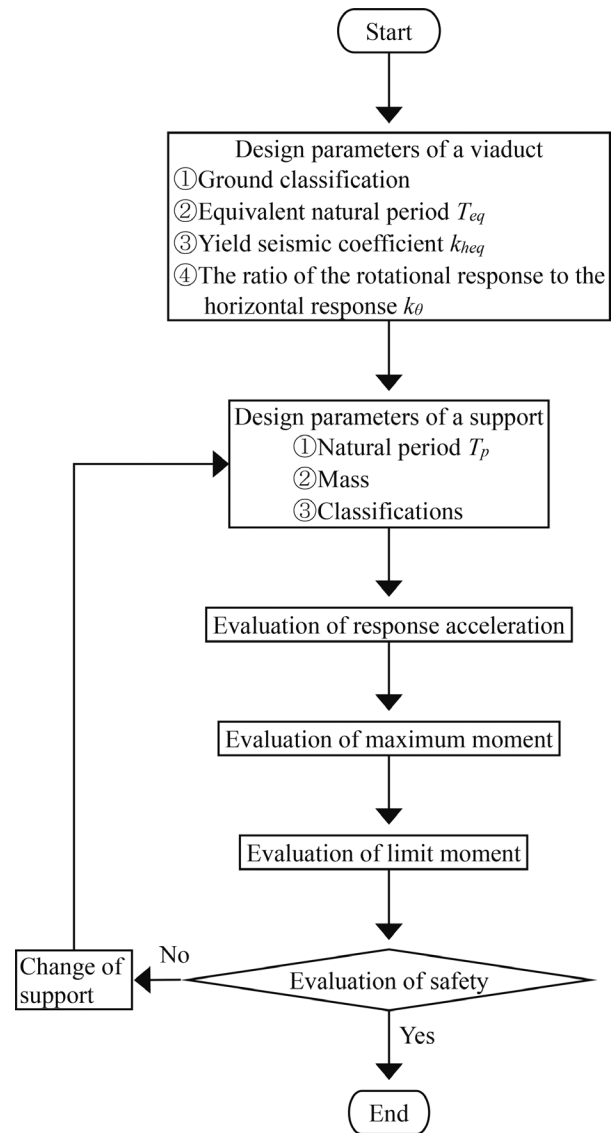


Fig. 2 Procedure of the seismic design method of supports on viaducts

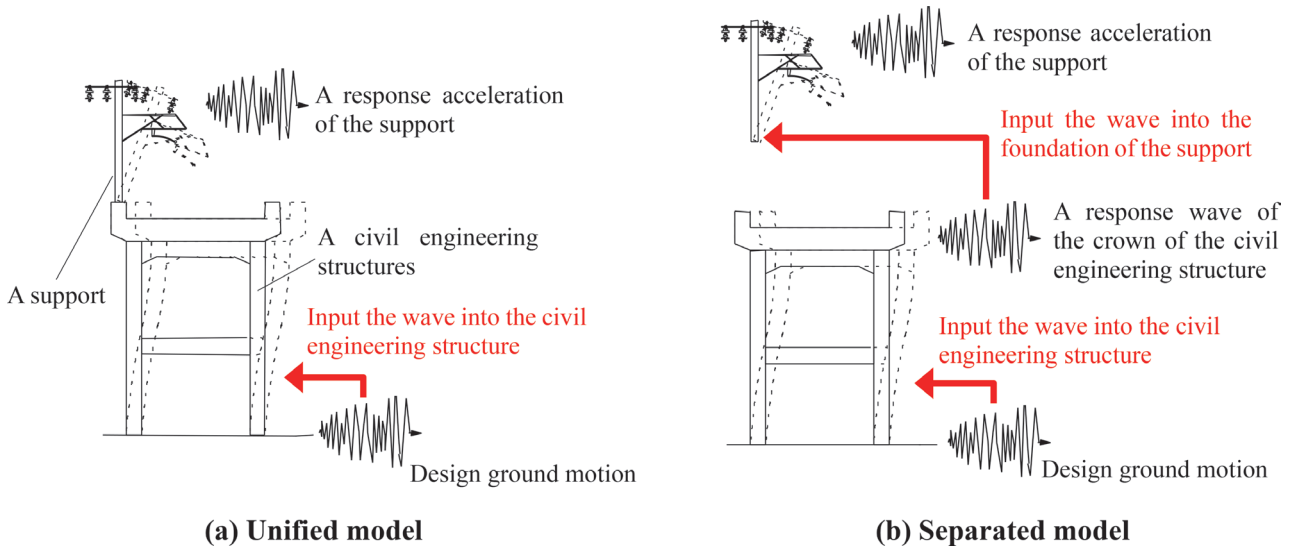


Fig. 1 Concept of models for the seismic design

motion for the seismic design of supports in the OCS Guideline.

L2 earthquake ground motion consists of spectra I and II. Spectrum I is assumed as a subduction-zone earthquake and spectrum II is assumed as an inland active-fault earthquake. The acceleration wave of spectrum I keeps for a longer duration than that of spectrum II. On the other hand, the acceleration wave of spectrum II has higher amplitude than that of spectrum I. Therefore, in the past OCS Guideline, only spectrum II had been used. However, on account of the structural characteristic of supports, we found that the duration of the ground motion affects the response acceleration of supports when resonating with civil engineering structures. Therefore, in the latest OCS Guideline, we determine to use both spectra I and II.

Furthermore, in consideration of the characteristic of the ground motion and the damage at the 2011 Great East Japan Earthquake, in the Seismic Standard, we set two types of motion as L2 earthquake ground motion. One is the general ground motion that is the modification of the past design ground motion. The other is the additional ground motion in which a shorter period is predominant. In order to maintain consistency with the new design ground motion, in the latest OCS Guideline, we also determined the ground motion should be considered.

4.3 Methods of compensating the natural period of supports

As mentioned above, we design supports in consideration of vibration properties of both supports and civil engineering structures. A natural period is one of the vibration properties. In the past OCS Guideline, the natural period of a support such as a single pole was calculated assuming that it was the first natural period of a cantilever. Equation (1) shows the calculation.

$$T_p = \frac{1}{f_p}, f_p = \frac{1}{2\pi} \left(\frac{1.875}{L} \right)^2 \sqrt{\frac{EI}{\rho}} \quad (1)$$

where,

T_p : Natural period of a support (s)

f_p : Natural frequency of a support (Hz)

L : Length of a support (m)

EI : Flexural rigidity of a support (Nm²)

ρ : Mass per unit length of a support (kg/m)

However, the mass of overhead wires and metal fittings attached to the pole may have an effect on the natural period of the pole. Figure 3 shows the example of calculations considering the effect. The natural frequency of the pole with wires and fittings is smaller than that of the pole without them. In case of a steel pipe pole, its natural frequency is much smaller, since it is lightweight.

Figure 4 shows the relation between load-point displacement and bending moment of a concrete pole. They are not in linear if the concrete pole is subjected to a load more than the allowable load of concrete. As the flexural rigidity of the concrete pole decreases, we need to consider the effect of it on the natural period of the pole.

The latest OCS Guideline describes compensation coefficients in order to compensate the natural period of a support in consideration of the mass of objects attached to the support and, in case of concrete supports, the flexural rigidity of supports as well.

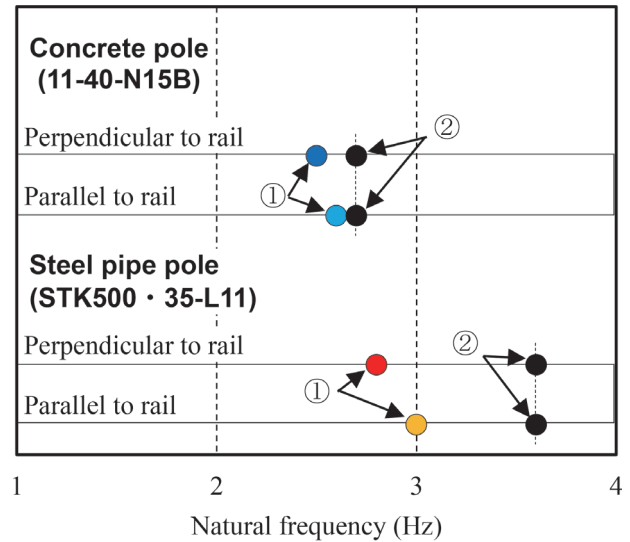
4.4 Evaluation of response acceleration

4.4.1 Horizontal response acceleration

As same in the past OCS Guideline, we evaluate the horizontal response acceleration of a support using both the response acceleration spectrum and the ratio of between the equivalent natural period

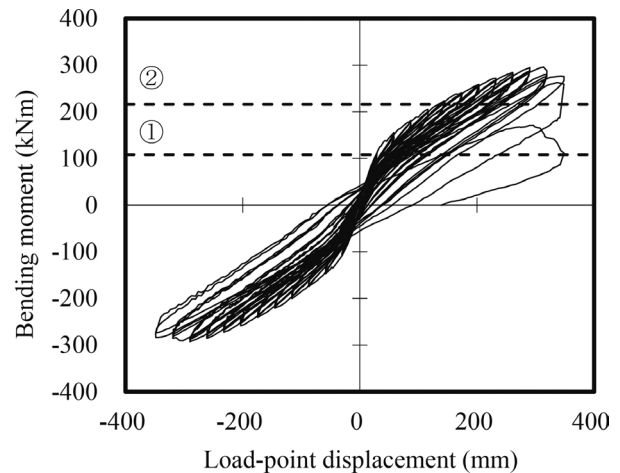
of a viaduct T_{eq} and the natural period of a support T_p . The latest OCS Guideline describes the new response acceleration spectrum according to combination of the ground classifications and support classifications. The ground classifications have five categories according to the characteristic of the ground. Supports are classified into two categories depending on their material, that is, concrete and steel. Figure 5 shows the example of the response acceleration spectrum.

We evaluate the response acceleration of a support using the



- ① Pole which general wires and metal fittings attach to
- ② Only pole

Fig. 3 Effect of mass of objects attached to poles on the natural frequency of poles



Load-point: A point located 5.775 m away from the foundation of the pole

- ①: Allowable bending moment
- ②: 2×allowable bending moment (Limit moment)

Fig. 4 Relation between load-point displacement and bending moment of a pole (Concrete pole: 9-40-N11B)

response acceleration spectrum in consideration of an effect of horizontal response of the viaduct. However, we found that this evaluation by a separated model is smaller than that by a unified model. Since that by a unified model is more precise, the past design method by a separated model can be dangerous [6]. To evaluate the behavior of supports more adequately at the time of an earthquake, we should also consider the effects of the rotational response of viaducts (Fig. 6). Actually, we have confirmed that considering this effect, we have estimated the situation of damage more adequately at the 2011 Great East Japan Earthquake [6].

The latest Seismic Standard describes the method to evaluate the response acceleration in consideration of the effects of the rotational response of a viaduct. On the basis of this, we set the ratio of the rotational response to the horizontal response $k\theta$ in the latest OCS Guideline as the compensation coefficient to compensate the response acceleration of a support to the horizontal response of viaducts.

Equation (2) shows how to compensate the horizontal response acceleration of a support.

$$A'_h = A_h \times (1 + k_0 \times L) \quad (2)$$

where,

A_h : Horizontal response acceleration of a support (m/s^2)

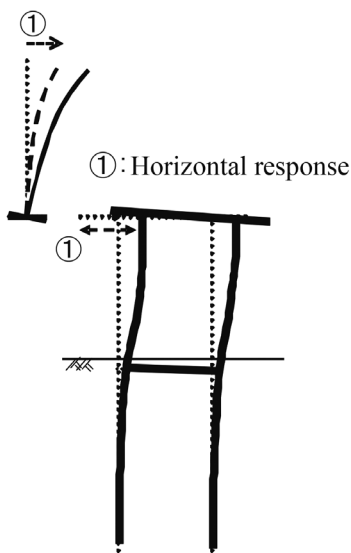
A'_h : Compensated horizontal response acceleration of a support (m/s^2)

k_0 : The ratio of the rotational response to the horizontal response.

By installing this method of compensating, the evaluation by a separated model is almost equal to that by a unified model [6]. Therefore, the method by a separated model in consideration of the effects of rotational response is more precise. Furthermore, we are easy to apply this method since it is similar to the past method.

4.4.2 Vertical response acceleration

We set the vertical response acceleration of a support to a half of the maximum of the design ground acceleration according to the ground classification in order to maintain consistency with the Seismic Standard.



(a) Only effect of the horizontal response

4.5 Evaluation of the maximum moment

The maximum moment of a support is the moment at the foundation of the support. Figure 7 shows the loads used in calculating the moment at the ground of a support. We calculate the moment generated by inertial force of the support, the overhead wires and objects attached to them. Assuming that response acceleration calculated in the previous section is acting at the center of gravity of the support, we calculate inertial force multiplying the mass of them by this acceleration. In this regard, we assume that masses of the overhead wires are a half of them since they are not rigidly attached to the support.

Equation (3) shows the calculation of the moment of a support at the foundation.

In order to evaluate safety, we check that this moment is smaller than the limit moment of the support. Otherwise, we should

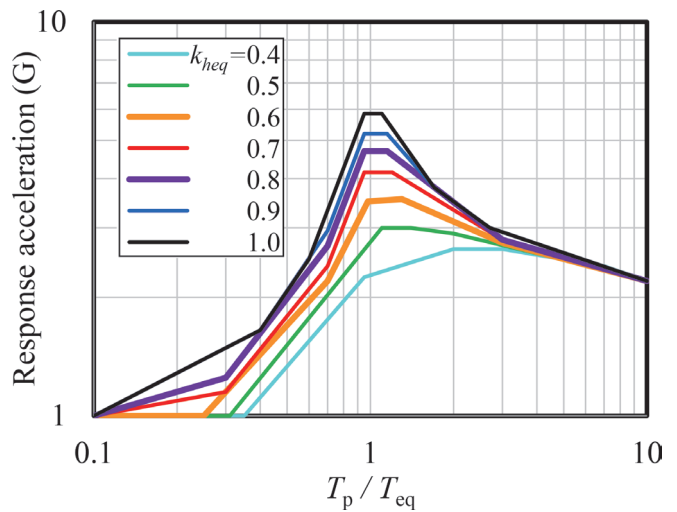
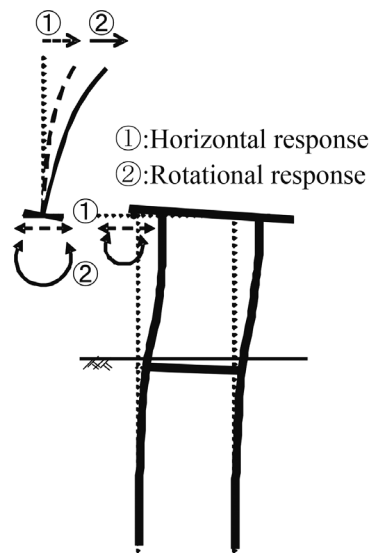


Fig. 5 Example of the response acceleration spectrum of a concrete support (Ground classification: G3, k_{heq} : yield seismic coefficient)



(b) Additional effect of the rotational response

Fig. 6 Effect of the rotational response of viaducts on the response acceleration of supports

change the support to the adequate one and evaluate the safety of it in the same way. The limit moment of supports is set at the double allowable bending moment, since the safety factor for breaking strength is greater than two [7].

$$M = \begin{cases} A'_h g \sum mh + (1 + A_v) g \sum mr + (1 + \alpha) \sum ph & \text{(Perpendicular to the direction of the rail)} \\ A_h g \sum mh & \text{(Parallel to the direction of the rail)} \end{cases} \quad (3)$$

where,

M : Moment of a support at the foundation (the maximum moment of a support) (Nm)

A_v : Vertical acceleration of a support (m/s²)

α : Variability rate of the tension of overhead wires

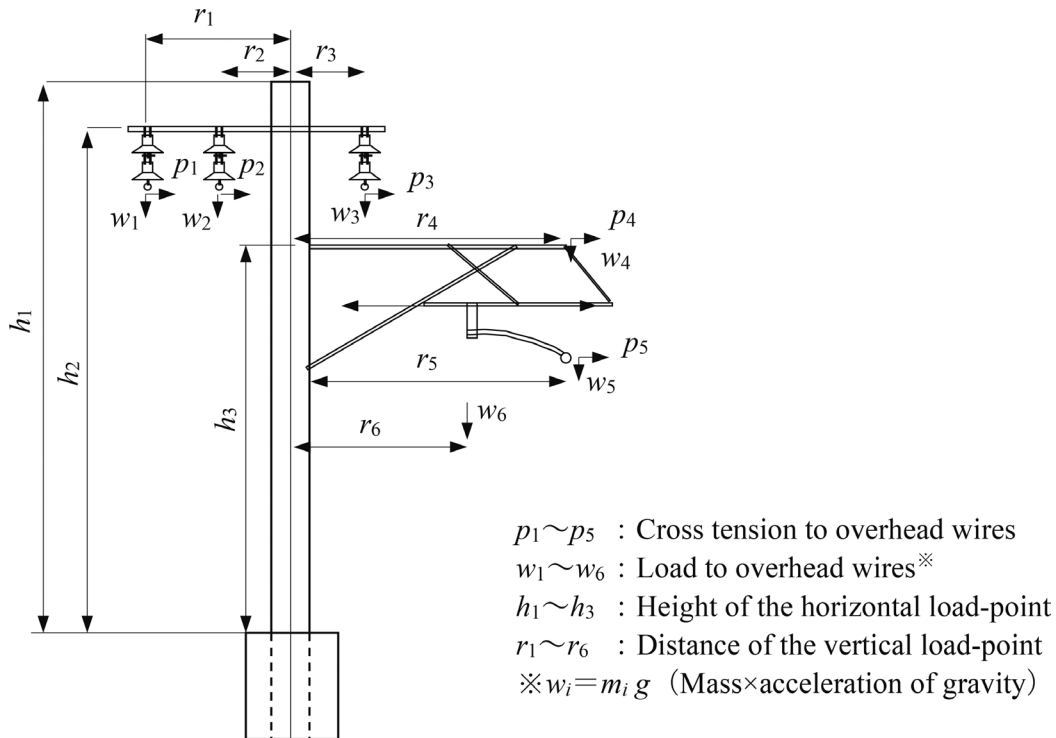


Fig. 7 Load related to the moment of supports at foundations of supports

Table 1 Main detail of the latest revision of the OCS Guideline

| Lists | The past OCS Guideline | The latest OCS Guideline |
|-------------------------------------|---|---|
| Ground motion to be considered | L2 earthquake ground motion Spectra II | L2 earthquake ground motion • General ground motion Spectra I, spectra II • Ground motion in which shorter period is predominant Spectra I, spectra II |
| The natural period of single pole | The calculation of the first natural period of a cantilever | Calculation of the first natural period of a cantilever compensating the following effect • The mass of overhead wires and metal fittings attached to the pole • The flexural rigidity of the concrete pole |
| Evaluation of response acceleration | In consideration of the only effect of the horizontal response of the viaduct | In consideration of the effect of the horizontal and rotational response of the viaduct |

4.6 Conclusion of latest revision of the OCS Guideline

Table 1 shows main details of the latest revision of OCS Guideline. These revisions allow us to evaluate the seismic performance of supports more precisely.

5. Conclusion of this paper

In order to maintain consistency with the revised Seismic Standard, we revised the OCS Guideline. The latest OCS Guideline includes new knowledge and examples of the evaluation of seismic performance to design supports efficiently and more precisely. In order to operate Japanese railway more safely, we should keep improving the precision of evaluating seismic performance.

References

[1] Railway Technical Research Institute, *The Seismic Design*

Guideline for Overhead Contact Systems and Commentary, 1982 (in Japanese).

[2] Railway Technical Research Institute, *The Design Standard for Railway Structures and Commentary (Seismic Design)*, 1999 (in Japanese).

[3] Railway Technical Research Institute, *The Design Standard for Railway Structures and Commentary (Seismic Design)*, 2012 (in Japanese).

[4] Railway Technical Research Institute, *The Seismic Design Guideline for Overhead Contact Systems and Commentary*, 2013 (in Japanese).

[5] Railway Technical Research Institute, *The Seismic Design Guideline for Overhead Contact Systems and Commentary*, 1997 (in Japanese).

[6] Takashi Kato, et al., "Evaluation of the Seismic Response by the Model of the Structure and the Power Pole," *RTRI Report*, Vol. 26, No. 11 (2012) (in Japanese).

[7] Yasukazu Fujii, et al., "Vibration and Bending Properties of Poles for Overhead Contact Systems in Earthquake," *RTRI Report*, Vol. 11, No. 5, 1997 (in Japanese).

Author



Yuichi KONDO
Assistant Senior Researcher, Contact Line
Structures Laboratory, Power Supply
Technology Division
Research Areas: Dynamics of Overhead
Contact Systems

DC-DC Converter Control Method for High Voltage DC Feeding System to Improve Use of Regenerative Power

Tsurugi YOSHII

Power Supply Systems Laboratory, Power Supply Technology Division

Tamanosuke OIDE

Power Supply Systems Laboratory, Power Supply Technology Division (Former)

A high voltage DC feeding system, which consists of higher-voltage feeders and DC-DC converters in addition to an existing feeding circuit, is assumed to improve the performance of power supply to trains without changing the nominal voltage of contact lines and onboard traction systems. In this system, the method for controlling the converter is an important element which must be taken into consideration to maximize energy savings. In this paper, we propose a converter control method to make the voltage ratio constant between the contact line and the higher-voltage feeder. In this paper, the high voltage DC feeding system with this converter control method is called a “DC-AT feeding system.” We evaluated the energy savings of this system through simulation, and case studies on a model line confirmed that this system can reduce energy consumption by 4.5% at most, and on average 3.5%, compared to conventional DC feeding systems.

Key words: DC feeding system, high-voltage DC feeding system, DC-DC converter, regenerative power, energy saving, auto-transformer

1. Introduction

DC electric railways are generally low-voltage and high-current systems for the amount of power they should supply. For this reason, there are problems such as voltage drops and Joule loss, due to the resistance of contact lines, due to the large resistance of contact lines, feeders and rails, and poor utilization of regenerative braking power.

In Japan, to solve these problems proposals have been made on several occasions until now to change the standard voltages of the contact line from 1500 volts to 3000 volts. However, implementation of this proposals was too difficult: not only because of the high cost and time required for renovating contact line supports and substations, but also because of the need for expensive dual voltage motor cars that can operate under multiple DC voltages used while construction of the system was underway.

This led to the idea of a “high-voltage DC feeding system,” shown in Fig. 1. This idea has been examined in various fields for some time [2, 3]. One of the purposes of this system is to obtain the same advantages as raising the standard voltage of contact lines, by installed “high voltage feeders” with a higher voltage than that of the contact line. With this method, existing 1500 V trains can continue to operate, and construction can be advanced in stages. However, in order for the system to function effectively, one particular issue had to be overcome: how to control power converters that transfer power between the contact line and the high-voltage feeder.

Therefore, we examined a new control method for the converters used in this system. The new method can promote the interchange of regenerative power, and significant energy savings can be obtained. This paper describes the details of the control method, and simulation case studies conducted to verify energy savings achieved with this system by implementing this method.

2. High-voltage DC feeding system

2.1 Outline configuration of high-voltage DC feeding system and its expected effects

In the high-voltage DC feeding system, the voltage of the contact line (hereinafter referred to as T; including existing feeder) is not changed, but a high-voltage feeder (F) is added to operate at a higher voltage than T, and DC-DC converters (hereinafter referred to as converters) are installed at traction substations (hereinafter referred to as SS) and track sectioning cabins (hereinafter referred to as SP). The converters transfer power between the T side and the F side, and the power flow between substations and loads (trains) are divided appropriately between the T side and the F side.

One significant advantage of this system is that it can achieve the same effect as raising the contact line voltage while continuing to use existing vehicles. Control methods and circuit methods of the converters are important factors to determine the effectiveness of the high voltage feeder system.

2.2 Solving the problems of DC electric railways with a high voltage DC feeding system

Silicon diode rectifiers (hereinafter referred to as diode rectifiers) are generally used in DC electric railways. The power flow of diode rectifiers is unidirectional from AC to DC. Therefore, in order to save energy, the regenerative power generated by a decelerating train using regenerative braking (regenerating train) should be used

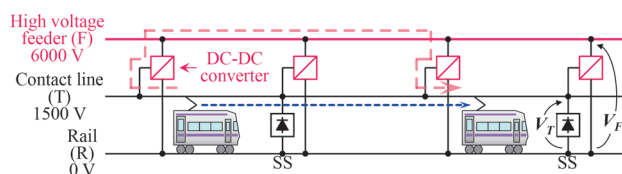


Fig. 1 High-voltage DC feeding system [1]

better within the feeding circuit, that is, it should be smoothly transferred to another accelerating train (powering train).

However, compared to the peak power flow up to several megawatts per train in acceleration or deceleration, the nominal value of 1.5 kV is sometimes considered not high enough to ensure sufficient power transfer capability. One of the examples is restriction of regenerative braking. When there is a large distance between a regenerating train and a powering train, the transferable current between them is limited due to line resistance to avoid excessive voltage not allowed by the insulation design or traction circuit design. In such cases, the reuse rate of kinetic energy is low because mechanical brakes or onboard brake resistors are used to secure braking force.

With the larger power transfer capability obtained from adding high-voltage feeders, we expect that the high-voltage DC feeding system will be able to promote regenerative power interchange between trains and bring significant energy savings. However, previous studies have examined the high-voltage DC feeding system only from the perspective of improving the efficiency of power supply from substations to trains, and there have been few specific studies of the effect of promoting regenerative power interchange [2, 3]. Therefore, we did research focused on this point.

3. DC-DC converter control methods

There can be innumerable control methods for power transfer between the T side and the F side of converters. One of extremely advanced examples is when each converter is controlled in real time according to certain information, such as position and load status of each train, which is collected in a facility such as an operations control center. However here, we attached greater importance to finding a method which would be more feasible, easier to implement, easier to operate and fast to install. Consequently, the control method would ideally not require control information obtained remotely from other locations other than where each converter was installed --- for example from the central processing equipment in the operations control center, and so on. Each converter should be able to operate stand-alone, using only the measurements of voltage and current with sensors in each converter itself.

Such simple controls that satisfy the above-mentioned conditions could be as follows:

- Constant control of the F side voltage V_F
- Constant control of the T side voltage V_T
- Emulating an output characteristic of existing diode rectifiers and inverters in substations (e. g. V_T drops linearly according to current output to contact line, while V_T is constant when the current is drawn from the contact line)
- Constant control of the voltage ratio $N = V_F/V_T$

In the high-voltage DC feeding system, plural converters are installed in multiple locations, such as each substation and each track sectioning cabin. Also, they should be controlled as a group of converters with any or several of the above control methods. There are also countless configurations for group control, but the following requirements should be satisfied in order to demonstrate energy savings:

- Distributing appropriate currents between the T-side and the F-side
- Promoting regenerative power interchange
- Suppressing circulating currents

Since there is no external power supply on the F side, there must be at least one converter that directly controls the V_F in order to stabilize the V_F in a steady state. And it should be noted that the

power sent to the F side by one converter must be returned to the T side by another converter, minus losses.

4. DC-AT feeding system

4.1 Basic characteristics

We devised a method to meet the requirements of group converter control described in Section 3, to ensure constant control of the voltage ratio N to all the converters in the line (Fig. 2 (b)). This idea is based on the circuit topology of AT feeding systems (Fig. 2 (a)) which is one of the common configurations for AC feeding systems. Similar to high-voltage DC feeding systems, AT feeding systems aim to reduce voltage drops and perform long-distance power transmission by applying higher transmission line voltage than contact line voltage.

Although the connection relationship of T, F, and R is slightly different, a similarity in the geometric configuration of the circuit can be found between the autotransformer (AT) of the AT feeding system in Fig. 2(a) and the converter in Fig. 2(b). For this reason, we named the feeding system in Fig. 2 (b) a “DC-AT feeding system,” in the sense that it is a system composed of “Autotransformers operating in a DC circuit.”

Figure 3 shows the power flow and potential gradient in the DC-AT feeding system. There are following features of this system:

- Between adjacent converters, directions of potential gradient between the T side and the F sides are the same; i.e., basically, no circulating current is generated.
- The load condition of T side is accurately reflected on the F side since the variation of V_F is proportional to the variation of V_T due to the load current.
- A stable circuit can be constructed by simulating AT, which is a linear passive element.

4.2 Effect of improving regenerative power interchange

As mentioned previously, regenerative brake force is available only when the regenerative power is consumed by nearby loads, such as powering trains, etc. The V_T just at the point of a regenerating train must be higher than the V_T at the points of adjacent power-

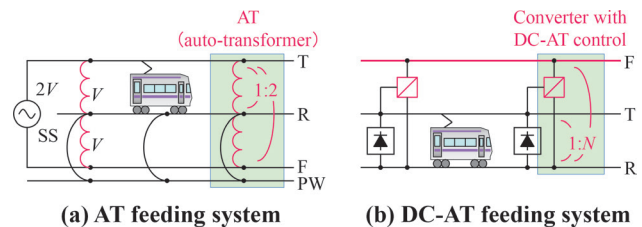


Fig. 2 Similarity between AT feeding system and high-voltage DC feeding system with DC-AT control (DC-AT feeding system) [1]

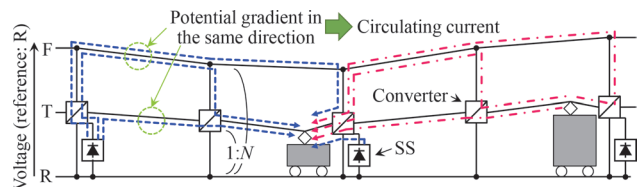


Fig. 3 Potential gradient in DC-AT feeding system [1]

ing trains or SSs to enable a transfer of the regenerative power through contact lines. In contrast, vehicle's onboard traction converters have generally implementation of a restricting control that limits regenerative braking when V_T exceeds a fixed voltage, in order to prevent damage to vehicles and feeding systems due to over-voltage. Therefore, the distance at which sufficient regenerative power can be interchanged is limited by voltage drops due to resistance of the feeding circuit and the restricting control described above. In other words, the farther a powering train and a regenerating train are apart, the more insufficient the regenerative braking power will be. As a result, the mechanical braking ratio increases, and more kinetic energy of a regenerating train is lost as thermal energy.

Here, focusing again on the characteristics of DC-AT feeding systems, converters with the constant control of the voltage ratio N can be regarded as impedance converters as well as transformers. Therefore, the resistance of a high-voltage feeder r_F is seen as $r'_F = r_F/N^2$ when referred to the T-side circuit. For example, assuming $N = 4$, it is equivalent to adding a somewhat unrealistic low resistance feeder which has a 16 times larger cross-sectional area than that of an ordinary one in conventional DC feeding systems (Fig. 4).

As a result, as shown in Fig. 5, the electrical distance between SS and trains or between trains is greatly shortened, which results in significant energy savings such as reduction of power transmission loss and increase in regenerative power interchange.

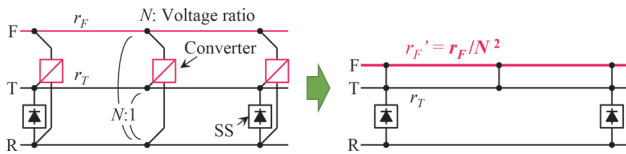


Fig. 4 Equivalent circuit of DC-AT feeding system [1]

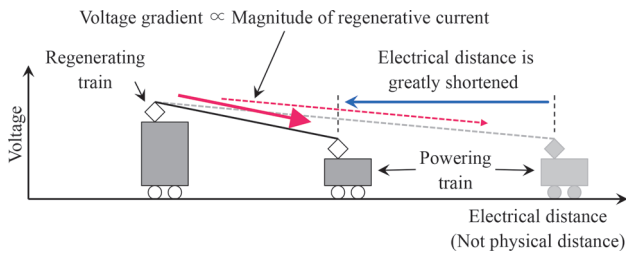


Fig. 5 Increased regenerative current due to shorter electrical distance

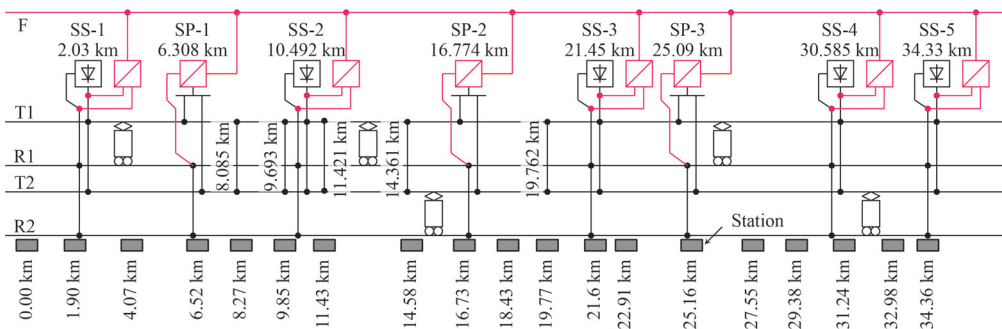


Fig. 6 Suburban line model [1]

5. Verification of energy savings by simulation

5.1 Simulation conditions

Trains move around on rails; magnitude and direction of its current also changes greatly and rapidly. Therefore, the power flow of the entire circuit, consisting of multiple substations, DC-AT converters and trains, is very complicated and involves large time-dependent changes.

In order to verify energy savings of the proposed system compared to conventional DC feeding systems (hereafter referred to as "conventional systems"), it is essential to determine change in power consumption of an entire circuit with difficult characteristics. In other words, it is necessary to calculate the power flow at each moment in time sequentially and integrate them as they change from time to time. An analysis based on a state of the circuit at a certain moment in time or an analysis that treats each electric quantity as an average value alone will not provide a correct evaluation.

Therefore, we used the DC traction power supply simulation tool [4] that can evaluate the continuous time variation of electrical and dynamic behavior of trains, similar to that of an actual feeding circuit. Here, we assumed that the DC-AT feeding system to be applied to a double-track model line electrified by the conventional system as shown in Fig. 6, which is based on an actual line. The speed limit and gradient were set in accordance with a certain real commuter line. Calculation steps are at 1-second intervals.

The train characteristics used in the simulation were based on those of a typical commuter train (7-car train) in operation on that certain line. The restricting control described in Section 2.2 was also taken into account as a characteristic that starts restricting at $V_T = 1700$ V and decreases linearly with the V_T until the regenerative braking effort reaches zero at $V_T = 1830$ V.

The high-voltage feeder was common to both up and down lines. The converters were installed in all SSs and SPs, and the voltage ratio N was set to 4. The conversion efficiency of the converters was assumed to be 97% regardless of the current magnitude. Other circuit constants are shown in Table 1 and Table 2.

The train timetables for the simulation had to be set with care. In this research, we focused only on a comparison of power flow trends between DC-AT feeding systems and conventional systems. So we used a very simple assumption that all trains are operated with the same type and configuration, stop at every station, with a departure interval of 7 minutes and 30 seconds for both up track and down track (Fig. 7). Herein, the amount of interchanged regenerative power is strongly affected by the chances of an overlap of accelerating trains and decelerating trains. This is highly dependent on train timetables; executing simulation with only one particular train timetable is not enough to get a fair judgement of energy savings of

Table 1 Feeding circuit parameter (Substation)

| Substation | Rated Power (kW) | Voltage drop (%) | No-load voltage (V) |
|------------|------------------|------------------|---------------------|
| SS1 | 4000 | 5 | 1575 |
| SS2 | 6000 | 5 | 1575 |
| SS3 | 6000 | 5 | 1575 |
| SS4 | 6000 | 5 | 1575 |
| SS5 | 6000 | 8 | 1620 |

Table 2 Feeding circuit parameter (Contact line system)

| Line name | Resistance (Ω/km) | Note |
|-------------------------|-----------------------------------|---|
| Contact line (T) | 0.0238 | GT110 mm ² +St90 mm ² +HAL510 mm ² ×2 |
| Rail (R) | 0.017 | JIS 50 kgN |
| High voltage feeder (F) | 0.04845 | HAL300 mm ² ×2 |

GT: Copper grooved contact wires (JIS E 2101)

St: Zinc-coated steel wires strands (JIS G 3537)

HAL: Hard-drawn aluminum stranded conductors (JIS C 3109)

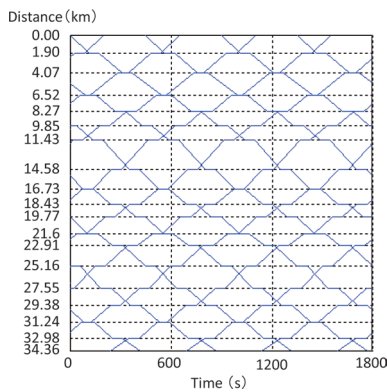


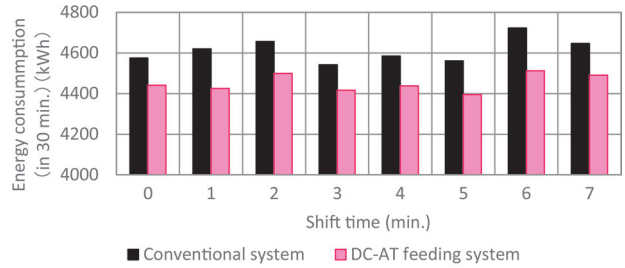
Fig. 7 Train timetable (shift time: 0 min.)

the proposed DC-AT feeding system compared to conventional systems. Therefore, we executed a total of 8 simulations with different train timetables: departure times of the down trains from the first station was fixed but departure times of the up trains was shifted in the step of 1 minutes from zero to 7 minutes (hereafter “shift time”).

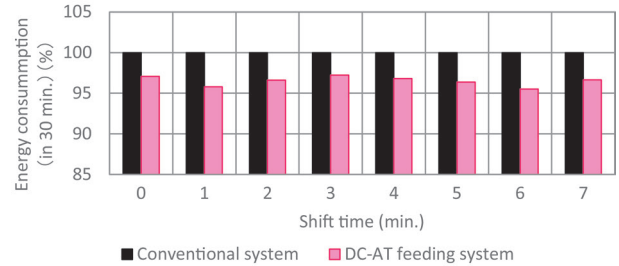
5.2 Evaluation of the effect of energy saving

Figure 8(a) shows comparison results of the total amount of energy supplied (energy consumed) from all SSs to the model line in 30 min. for each train timetable between a conventional system (circuit without the red line part of Fig. 6) and the DC-AT feeding system. When a regenerative power is reused by other trains, the total amount of energy supplied from SSs, that is, the total energy consumption, decreases. Fig. 8(b) shows the change in the amount of energy consumption for each train timetable, normalized it of the conventional system as 100.

It can be seen from Fig. 8(a) that the energy consumption varies widely depending on each train timetable in both cases of the conventional system and the DC-AT feeding system. This is because the opportunities of the overlap of acceleration and deceleration vary



(a) Absolute amount



(b) Relative amount with normalizing conventional system as 100%

Fig. 8 Difference in power consumption between conventional system and DC-AT feeding system [5]

depending on “time shifts.” Figure 8(b) shows that the DC-AT feeding system can reduce the energy consumption in all cases of shift time settings. The reduction in energy consumption reached 4.5% at most, and on average 3.5%. It should be noted that since these figures are affected by the condition of the lines, trains, timetables, and so on, the magnitude itself cannot be generalized.

Basically, the larger N , the higher the energy savings, however there is a trade-off between the higher savings and higher cost of responding to increases in rated voltage.

5.3 Verification of the effect of promoting the regenerative power interchanging

As shown in Fig. 8, the reduction in energy consumption by the DC-AT feeding system tended to be higher in the cases of train timetables which produced relatively large energy consumption on the conventional system (shift time: 1 min., 6 min.) compared to the other cases. This is probably because the effect of shortening the electrical distance becomes more obvious due to the DC-AT feeding system which reduces the power loss between substations and powering trains and promotes regenerative power interchanging.

Figure 9 shows the voltage and current at each location of the model line with the shift time: 6 min., and at the time: 558 seconds, as an example of how regenerative power interchange can be improved. Figure 9(a) shows the case of a conventional system and Fig. 9(b) shows the case of the DC-AT feeding system. In Fig. 9, trains shown with a red arrow and a positive current value are powering trains, and trains shown with a blue arrow and a negative current value are regenerating trains. The converters shown with a red arrow and a positive current value are in powering mode (power flow: F side to T side), and the converters shown with a blue arrow and a negative current value are in regenerative mode (power flow: T side to F side). Voltage values shown at the top of Fig. 9(a) represent output voltages of rectifiers in substations. Voltage values shown at the top of Fig. 9(b) are V_F (upper) and V_T (lower) of the

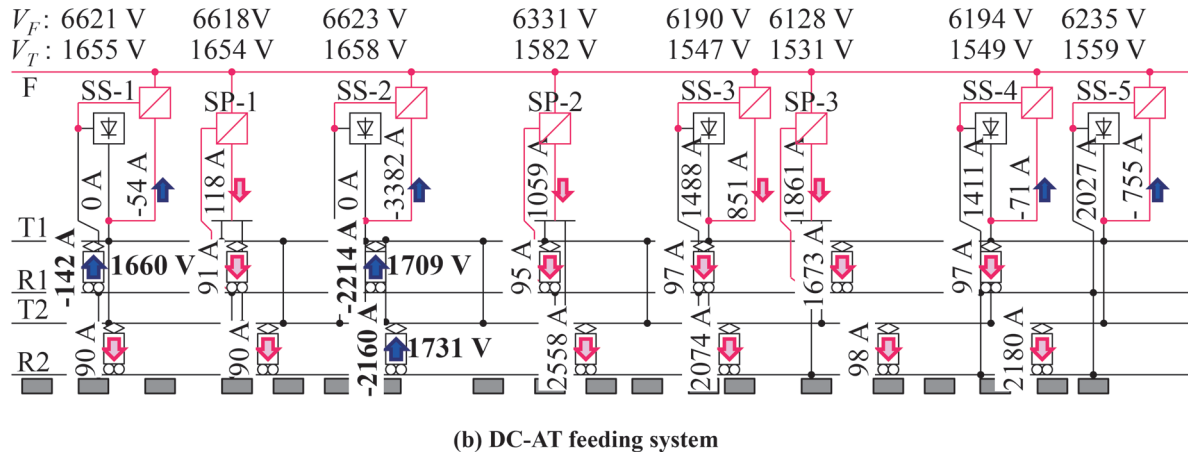
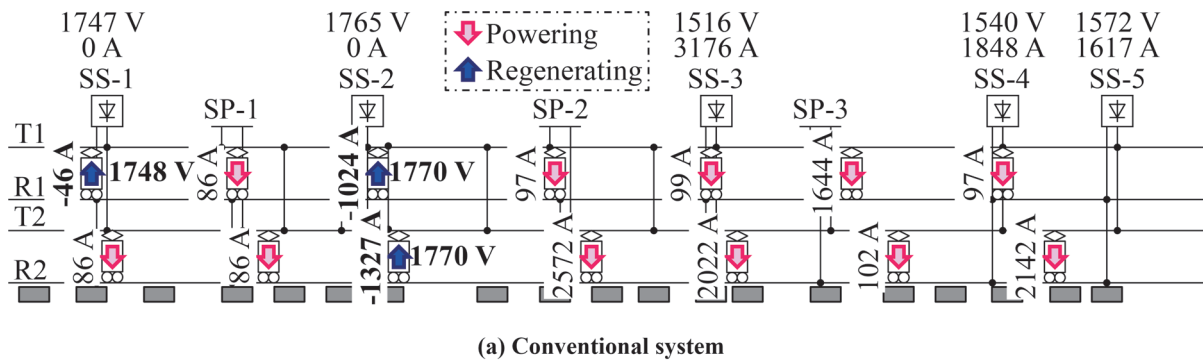


Fig. 9 Current distribution of model line (shift time: 6 min., $t = 558$ s) [5]

converters. For converters placed in substations, V_r equals to the DC output voltage of the corresponding rectifier.

There are powering trains between SP-2 and SP-3 and total load current is 6000 A. At the same time, there are two regenerating trains nearby SS-2 and total regenerative current is 2400 A. In the case of the conventional system (Fig. 9(a)), the regenerative current is limited due to the restricting control, because V_r of these trains reached 1700 V or higher, which exceeds the threshold at which the control starts. That means, despite sufficient energy demand, the regenerative power interchange was limited due to the electrical distance and a large amount of energy expected to be regenerated was lost. As a result, a current of approximately 3200 A is supplied from SS-3 to the powering trains; which leads to an increase in power received from the power grid.

On the other hand, in case of the DC-AT feeding system, V_r of regenerating trains decreased to 1709 V (the train on down track), 1731 V (the train on up track) respectively and the total regenerative current increased by 80% to about 4400 A. Of this regenerative current, 3300 A or more was sent to the F side by the converter within SS-2, and returned to the T side from the converters within SP-2 and SP-3. In this way, regenerative current can be smoothly sent over a long distance by the high-voltage feeder, and as a result, the current from SS-3 decreases to about 1400 A, which is less than half.

6. Conclusion

This paper focused on high-voltage DC feeding systems consisting of high-voltage feeders and converters that transfer power between contact lines and high-voltage feeders in addition to con-

ventional DC feeding system as a way of saving energy on DC electric railways. We proposed a new converter control method to make the voltage ratio between the contact lines and the higher-voltage feeders constant. Then we named the high-voltage DC feeding system with this method implemented in all the converters a “DC-AT feeding system,” which improves regenerative power interchanging. We evaluated the energy savings of this system through simulation, and a case study on a model line confirmed that this system can reduce energy consumption by 4.5% at most, and on average 3.5%, compared to conventional DC feeding systems.

Acknowledgment

We would like to express our sincere gratitude to Mr. Takuma Ishiyama of Mitsubishi Electric Corporation, Mr. Takayuki Yachida of Toshiba Mitsubishi Electric Industrial Systems Corporation, Mr. Daisuke Akashi of West Japan Railway Company, and others who participated in this research.

References

- [1] Yoshii, T., Morimoto, H., Ishiyama, T., Yachida, T. and Akashi, D., “Control Method of DC-DC Converters for High-Voltage Feeding Systems,” *IEEJ Transactions on Industry Applications*, Vol. 142, No. 3, pp. 222-231, March 2022.
- [2] Ladoux, P., Blaquiere, J.M., Caron, H., Iannuzzi, D., and Coppola, M., “New three-wire supply systems for DC electric railways,” *IET Electrical Systems in Transportation*, Vol. 5, Issue: 3, 2015.

- [3] Ito, K., Shigeeda, H., Morimoto, H., Fujii, T. and Morishima, N., "Feeding-loss Reduction by Higher-voltage DC Railway Feeding System with DC-to-DC Converter," *2018 International Power Electronics Conference (IPEC-Niigata 2018 -ECCE Asia)*, DOI: 10.23919/IPEC.2018.8507567, 2018.
- [4] Morimoto, H. and Yoshii, T., "Extension of DC traction power supply simulation tool," *Proceeding of J-Rail 2015*, No. 2506, 2015 (in Japanese).
- [5] Yoshii, T., Ishiyama, T. and Kawahara, K., "DC-AT control method for DC-DC converter used for high voltage DC feeding system," *Proceeding of JIASC 2019*, R5-19, 2019 (in Japanese).

Authors



Tsurugi YOSHII
 Assistant Senior Researcher, Power Supply
 Systems Laboratory, Power Supply
 Technology Division
 Research Areas: DC and AC Traction Power
 Supply Systems



Tamasuke OIDE
 Researcher, Power Supply Systems
 Laboratory, Power Supply Technology
 Division (Former)
 Research Areas: DC and AC Traction Power
 Supply Systems

Train Frontal Obstacle Detection Method with Camera-LiDAR Fusion

Ryo KAGEYAMA

Nozomi NAGAMINE

Hiroki MUKOJIMA

Image Analysis Laboratory, Information and Communication Technology Division

Recently, the importance of obstacle detection methods for railway has been increasing. In the field of automobiles, obstacle detection systems with sensors have been introduced on mass-produced vehicles. However, in railway, a practical detection system does not exist because railways require longer detection distances than do automobiles. Therefore, we have developed a train frontal obstacle detection method using a camera and LiDAR. We confirmed that our method detects a person 200 m away, which a camera alone cannot detect, with 45% accuracy at night.

Key words: train front monitoring, deep learning, LiDAR, 3D point cloud processing sensor fusion

1. Introduction

Reducing the number of collisions is important to further improve the safety of railways. In the field of automobiles, Advanced Driver-Assistance Systems (ADAS) using cameras and sensors have been already developed and introduced on mass-produced vehicles [1]. In the case of railways, the coefficient of friction between wheels and rails is low, and braking distances are about three times longer than for cars traveling at the same speed. For this reason, it is difficult to apply ADAS for automobiles directly to railways, and sensors and algorithms that can detect more distant objects are needed. However, so far no system that meets these requirements has been put into practice. Therefore, we developed a method for detecting obstacles in front of trains which could be applied to operational support systems for railways. Our past studies examined detection methods based on machine learning [2] and detecting differences in successive images [3]. In this study, we developed a detection method using deep learning to further improve detection accuracy. In addition, as a countermeasure against the weakness visible light cameras, which is the deterioration of detection performance at night, we developed a detection method with integrated LiDAR.

2. Study of obstacle detection methods for railway

2.1 Target setting for detection performance

2.1.1 Consideration of detection targets

First, we examined the target object. According to the results of a survey of the percentage of railway crossing accidents by object involved in collisions, collisions with pedestrians accounted for the highest percentage of the 208 railway crossing accidents that occurred in FY 2019, which was about half the total number of accidents, or 95 cases [4]. Based on this observation, it was considered that detection of a person and avoidance of a collision would contribute to a significant reduction in the number of accidents. Therefore, in this study, we set people as the main target for detection.

2.1.2 Consideration of detection distance

The detection distance that should be satisfied by the obstacle detection method for railway should be at least 600 m, which is the standard braking distance in an emergency on conventional railway in Japan [5]. However, it is difficult to detect an object as large as a

person 600 m away with the performance of sensors available currently. In this study, we investigated distances below 600 m which would still mitigate disaster and set them as the target detection distances. For the main JR lines (about 10,300 km length), we calculated the percentage of line lengths that could be stopped at different braking distances from maximum speed of each line section and vehicle emergency deceleration [6]. Figure 1 shows a graph with the horizontal axis representing the braking distance and the vertical axis representing the percentage of line segments where this stopping distance was possible. It was found that when the braking distance is more than 300 m, stopping is possible on more than 50% of the route. From this, it can be inferred that if the target can be detected 300 m away, disaster mitigation would be effective for at least half of the line segments. Therefore, the target detection distance was set at 300 m in this study.

2.2 Target setting for detection performance

Figure 2 shows the overall picture of the detection method to achieve the target detection distance of 300 m. The proposed method extracts rails from the image of what can be seen from the front of the train, obtained from the camera, to limit the detection area to the direction in which the train is moving and more than 300 m ahead, which is the target detection distance. For the extracted detection area, object detection was performed only from the image information during daytime. On the other hand, during nighttime, when visible light cameras are not good at detecting objects, detection performance is ensured by integrating 3D point clouds obtained from LiDAR.

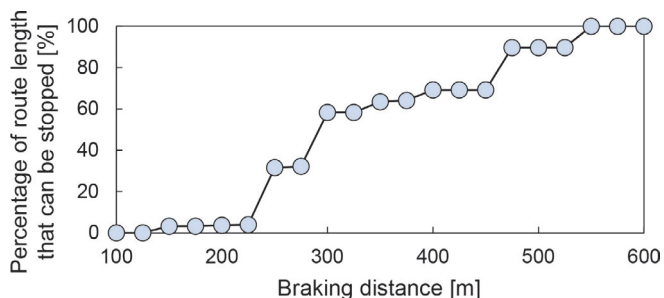


Fig. 1 Relationship between braking distance and percentage of route with suitable stopping distance.

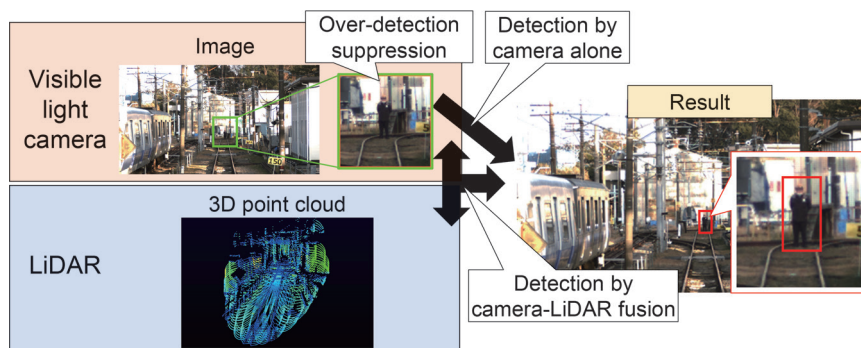


Fig. 2 Overall view of the train front obstacle detection method using camera and LiDAR.

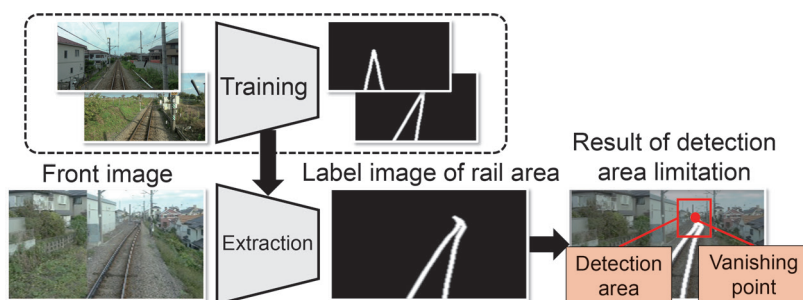


Fig. 3 Flow of detection area limitation.

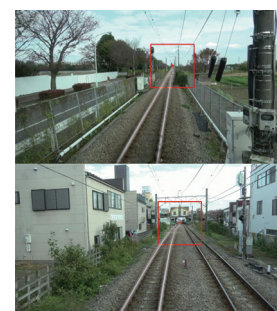


Fig. 4 Results of detection area limitation.

3. Over-detection suppression method

3.1 Suppression of over-detection by rail detection

Images from the front of the train contain information on various objects such as trackside equipment, roads and buildings, etc., which can cause over-detection. Since this leads to excessive train emergency stops, it should be prevented. Therefore, we developed a method to limit the detection area in the direction of train travel in order to suppress excessive detection in the preliminary stage of inputting the train front image to the detection algorithm.

Figure 3 shows a flow chart illustrating how the detection area is limited. In the proposed method, first, the rail position is learned by deep learning using single frames of the video taken from the front of the train and a dataset of mask images with pixel values only around the rail position in the corresponding frame. Next, the rail position is detected using the learned deep learning model. From among the rail detection frames, the detection region is then limited to an area centered on the vanishing point of the rail.

3.2 Over-detection suppression effect

Using the results of rail extraction using this method, the detection area limited around the extracted vanishing point are shown in Fig. 4. It was confirmed that the rails in the direction of travel were correctly extracted regardless of the track surface condition and alignment, and that the detection area was appropriately narrowed down.

The number of frames in which over-detection occurred for 2,500 frames of forward video was also compared. The number of frames in which over-detection occurred before limiting the detection area was 52, while the number of frames in which over-detection occurred after limiting the detection area was 1. This result confirms that this method can reduce the over-detection to less than

2%.

4. Detection methods using camera alone

4.1 Deep-learning based detection method

We developed a method to detect people and other objects using only a camera, on the basis of the detection area limited as described in the previous section. Figure 5 shows an image of the detection method. The proposed method uses an object detection algorithm based on deep learning [7]. This algorithm simultaneously predicts the object-likeness and type of objects in an image, and outputs the position, size, probability of existence, and classification of the object. The detection result is output for each frame, but information from the past 10 frames is used for the detection decision, and a frame is considered “detected” if 3 or more frames are observed in which “the existence probability is 80% or more and the person is correctly classified” out of 10 frames. This reduces the influence of instantaneous noise that occurs when the image of a person is momentarily obscured by windshield wipers, etc. in rainy weather.

4.2 Experiment for performance evaluation of the proposed detection method

4.2.1 Method of experiment

A field experiment was conducted to evaluate the detection method. A camera was installed inside the cab window at the back of a train, as shown in Fig. 6. Then, the camera took pictures as the train moved away from the subject (about 475 m away) again from the starting point near the subject on the track, as shown in Fig. 7. This single run is referred to as one trial run. The subjects were

people in different postures and clothing as shown in Fig. 8. In order to obtain sufficient resolution (more than 50 pixels) for the person at a distance of 300 m, a USB camera with a pixel count of 4,096 (W) x 2,160 (H) and a lens with a focal length of 50 mm was used.

4.2.2 Method of evaluating detection rate per distance

The detection rate for each distance between the train and the subject was obtained from the captured forward video using the following procedure.

- I. The total amount of movement is calculated by integrating over the frames after calculating the amount of movement of feature points between frames in the video.
- II. The distance between the train and the subject in each frame is estimated from the correspondence between the total distance traveled by the train per test number (475 m) and the total movement of the feature points.
- III. The entire frame is divided into 10-m distance increments from 0 m to 480 m, and the detection decision logic described in Section 4.1 is applied in each section. The detection rate is defined as the percentage of “detection” states.

For example, if the detection process is executed a total of 10 times for images obtained at 100 m to 110 m from the subject, and the “detection” status is obtained 9 times out of 10 times, the detection rate is 90%.

4.2.3 Result of evaluation

The detection algorithm was applied to a total of 56 test videos of a standing person during the daytime, and the detection rate for each distance was evaluated according to the procedure described in Section 4.2.2. Figure 9 shows an example of detection of a standing person facing 400 m away for one trial. It can be seen that the red frame indicating detection is displayed around the person even at a distance that is difficult to see with the naked eye. Figure 10 shows the results of obtaining the average value of all trial numbers (hereinafter referred to as “average detection rate”) and the maximum/minimum value for each trial number for the detection rate at each distance. The average value of the trial number confirms that the detection rate exceeds 98% at a target distance of less than 300 m. Figure 11 shows the results of the evaluation of the detection rate at different distances for different illuminance levels, using a person in a standing position facing forward as the subject and repeatedly photographed in the evening. The figure shows that the distance at which more than 90% of the subjects could be detected became shorter as the illuminance decreased, and this tendency was particularly pronounced at illuminances of less than 10 lx.

5. Detection method by camera-LiDAR fusion

5.1 Selection of a sensor used with the camera

The results of Section 4.2.3 suggest that in low-light conditions, in addition to cameras, it is necessary to combine other sensors that can be applied regardless of illumination. In automotive driver assistance systems, sensor fusion technology, which integrates information from multiple sensors to provide robust detection against environmental changes, has been adopted [8]. Millimeter-wave radar and LiDAR (Light Detection And Ranging) are rep-

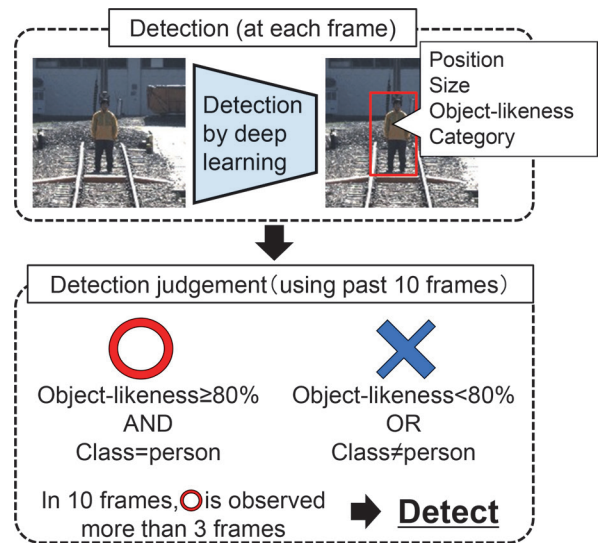


Fig. 5 Obstacle detection method from images.

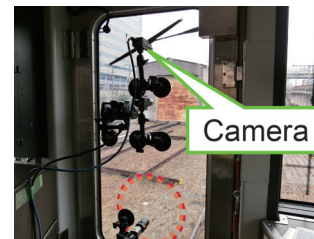


Fig. 6 Installation of camera on a train.



Fig. 7 Scene during data acquisition.



Fig. 8 Examples of subjects considered.

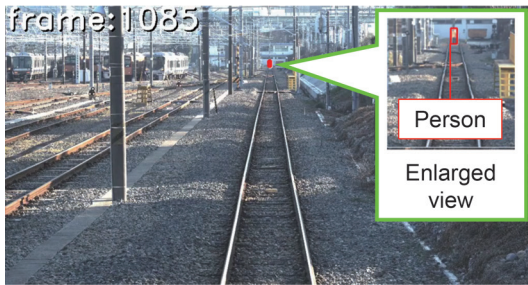


Fig. 9 Example of person detection results

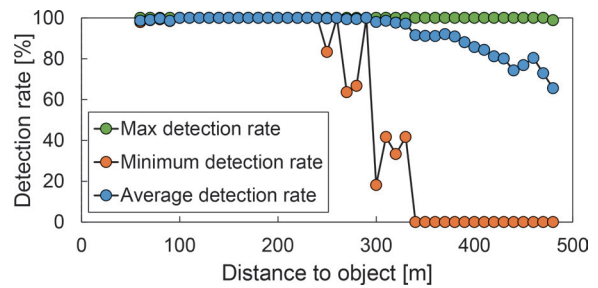


Fig. 10 Person detection rate by distance

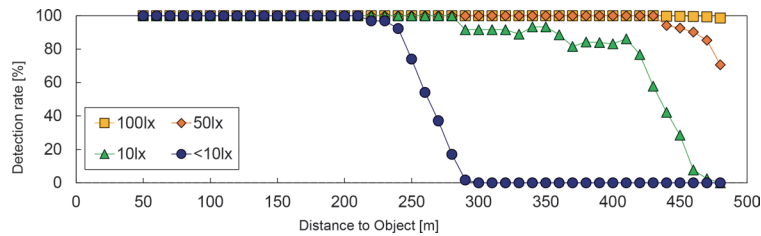


Fig. 11 Person detection rate at different distances when illumination is low.

representative sensors used with cameras in sensor fusion technology.

Millimeter wave radar emits radio waves in the millimeter wave band and uses the reflected wave information for object detection. LiDAR emits lasers in various directions and acquires reflections from objects as a point cloud. Like millimeter-wave radar, LiDAR can be used even at night, and depending on the model, high-density point cloud data can be obtained.

Sensors used together with cameras at night in a railway environment should be able to measure far distances regardless of brightness and have sufficient spatial resolution to detect objects. We decided to investigate the integration of a camera and LiDAR as a sensor to satisfy these conditions. In this study, we selected a sensor that can measure objects at distances of at least 300 m, regardless of the reflectance of the object and which had an angular resolution of 0.03° or less between adjacent lasers so that at least two lasers could hit a front-facing, standing person at 300 m away in the shoulder-width direction. The main characteristics of the selected LiDAR are shown in Table 1, and the point cloud of the test line in the Railway Research Institute acquired by LiDAR is shown in Fig. 12. Results shown in Fig. 12 confirm that a high-density 3D point cloud of the railway environment can be acquired.

5.2 Detection method by camera-LiDAR fusion

We developed a detection method by integrating a camera and selected LiDAR. An image of the detection method is shown in Fig. 13. In this method, the 3D point cloud data measured by LiDAR is superimposed on the deep learning detection method described in Section 4.1. In the process of detecting objects from images by deep learning, predicted values of object-likeness and object classification are output for each small region (grid) that delimits the image. When the image of the object is clear, the area around the grid with high object-likeness is converted into the position and size of the object and output as the final detection result along with the classification of the object in this area. However, in low-light conditions, such as at night, the object-likeness value is reduced, and the object cannot be detected. Therefore, after the camera and LiDAR are aligned in advance, the point cloud data is projected onto this image to supplement the object-likeness information. The projected point

cloud is preprocessed by removing ground points using the Random Sample Consensus (RANSAC) algorithm [9] and by using Density-Based Spatial Clustering of Applications with Noise (DBSCAN) [10]. The algorithm removes the point clouds corresponding to the surrounding buildings, and only the candidate objects for detection are extracted. The degree of occupancy of the point cloud in each grid in the image is then determined. Occupancy is defined as the ratio of the pixel on which the point cloud is projected to the surrounding pixels in the small area. For each grid, the degree of occupancy is compared with the object-likeness, and if the degree of occupancy is greater than the value of object-likeness, the value of object-likeness is replaced by a degree of occupancy. This allows detection of an object even when the object is obscured in the image, as long as a point cloud data of a certain density is observed. Finally, the object detection results for each frame are output in the same format as in Section 4.1. Therefore, the same detection decision logic as in Section 4.1 can be applied to this method.

Table 1 Specification of selected LiDAR

| | |
|---------------------|--|
| Detection distance | 320 m at 10% Reflectivity 500 m at 50% Reflectivity |
| Angular resolution | 0.03° |
| Distance resolution | 15.7 cm (at 300 m) |

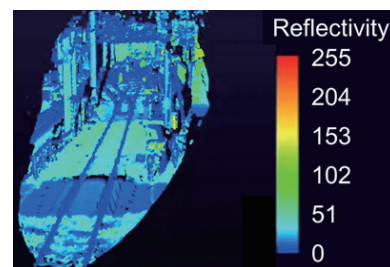


Fig. 12 Point cloud for 0.2 seconds obtained with selected LiDAR.

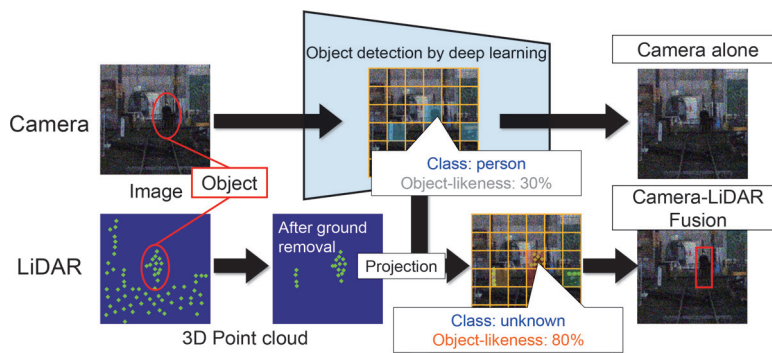


Fig. 13 The image of obstacle detection method by camera-LiDAR fusion.

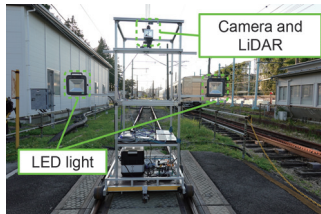


Fig. 14 Equipment used in experiment.



Fig. 15 Scene of experiment at night.

5.3 Experiment for performance evaluation of the proposed detection method

5.3.1 Method of experiment

Evaluations of the method’s performance described in the previous section were conducted in the evening and at night on a straight section (approximately 200 m in length) of the test line within the Railway Technical Research Institute. For the test, a device was made that imitated the head of a train. As shown in Fig. 14, the device consisted of a hand-pushed bogie and an aluminum frame, and a camera and LiDAR were installed at a height equivalent to that of the driver’s cab. As shown in Fig. 15, an LED light was installed at a position equivalent to the front light of a train and was always on during the night. All subjects were standing people facing the front.

When the illumination was low before and after sunset, the light was turned off and the dolly was positioned at 200 m from the subject, and the images were repeatedly taken for 10 seconds every minute. During the night, the dolly was positioned between 50 m and 200 m from the subject in 25 m increments for 10 seconds, and the images were repeatedly taken. The series of data taken from 50 m to 200 m was considered to be one trial number. The detection rate was calculated as the ratio of the number of “detection” events in the same way as when the detection judgment described in Section 4.1 was applied to the 10-second shooting data.

5.3.2 Result of experiment

Figure 16 shows the relationship between illuminance and detection rate at 200 m from the subject for each of the cases of a camera only and integrating a camera and LiDAR, in the evening when illuminance decreases. In the case of the camera only, the detection rate dropped sharply when the illuminance was between 5 lx and 10 lx, and fell to 0% at lower illuminance, while the detection rate in the case of the proposed method was confirmed to be over 90% regardless of the illuminance. Similar to Fig. 16, Fig. 17 shows the relationship between distance to object and detection rate (the

relationship between the distance from the subject and the detection rate under illumination of 0.2 to 0.3 lx, which is equivalent to an illuminance with a full moon) for the camera-only method and the integrated camera and LiDAR method respectively. Here, the average values of 20 trials are shown. While the detection rate of the camera alone was 0% at over 75 m from the subject, the detection rate of the proposed method was more than 90% up to a distance of 150 m from the subject and about 45% at 200 m, so that improvement of the detection rate was confirmed.

6. Conclusion

To improve safety and reduce transport disruptions by preventing train collisions, we developed a train frontal obstacle detection method with a camera and LiDAR.

A detection area limitation method based on rail extraction was developed to suppress over-detection. We confirmed that the detection area can be set centered on the vanishing point of the rail and that over-detection can be suppressed to less than 2% by limiting the detection area.

We also developed a method to detect obstacles in front of a train using only a camera by applying deep learning object detection. Using the developed method, we confirmed that the detection rate was 98% or higher at a distance of 300 m from the target during the daytime. On the other hand, we confirmed that the detection rate decreases as illuminance falls from evening to night. To complement the method’s nighttime performance, we selected and applied LiDAR. Furthermore, we developed a detection method that integrates the camera and the LiDAR. We have confirmed that the detection of a person in the evening is independent of illumination degradation, and that the camera cannot detect a person at a distance of over 50 m at night, whereas the integrated detection method with LiDAR was able to detect 45% of the human targets at a distance of 200 m. In the future, we will evaluate the performance of the system in a straight section of 300 m or more and the performance when the system is actually installed on a vehicle. The final goal is to establish a technology that can detect objects 600 m away.

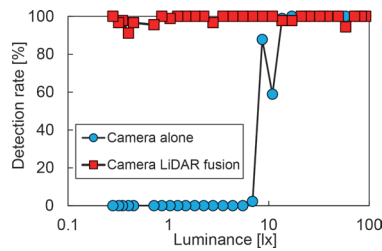


Fig. 16 Detection rate of person 200 m ahead at low illumination.

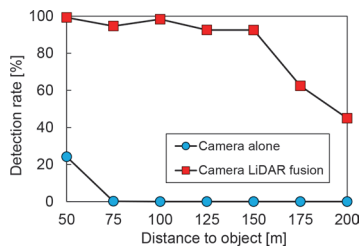


Fig. 17 Detection rate of person by distance at night.

References

[1] Hiraoka, T., “A Driving Support System for Encouraging Drivers to Drive Safely,” *Measurement and Control*, Vol. 51, pp. 742-747, 2012 (in Japanese).

[2] Niwa, J., et al., “The Detection of the Person on the Track by Front Surveillance from the Train based on Single-lens Camera Image,” *The papers of Technical Meeting on TER*, TER-17-020, 2017 (in Japanese).

[3] Nakasone, R., et al., “Frontal Obstacle Detection using Background Subtraction and Frame Registration,” *RTRI Report*, Vol. 31, No. 3, pp. 11-16, 2017 (in Japanese).

[4] Cabinet Office, “Trends in railway traffic accidents,” *Traffic Safety White Paper*, pp. 156-158, 2020 (in Japanese).

[5] MLIT Railway Bureau, *Explanation: Technical standards for railway (8th Edition)*, Japan Train Operation Association, 2020 (in Japanese).

[6] Nagamine, N., et al., “People Detection Method using Deep Learning by Monocular Train Frontal View Camera,” *The papers of Technical Meeting on TER*, TER-19-025, 2019 (in Japanese).

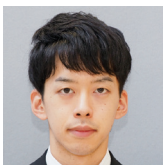
[7] Bochkovskiy, A., et al., “YOLOv4: Optimal Speed and Accuracy of Object Detection,” arXiv: 2004.10934, 2020.

[8] Technical Information Institute, *Development of sensor fusion technology and application examples (1st Edition)*, 2019 (in Japanese).

[9] Fischler, M.A., et al., “Random sample consensus: a paradigm for model fitting with applications to image analysis and automated cartography,” *Commun. of the ACM*, Vol. 24, No. 6, pp. 381-395, 1981.

[10] Ester, M., et al., “A density-based algorithm for discovering clusters in large spatial databases with noise,” *Proc. KDD 1996*, pp. 226-231, 1996.

Authors



Ryo KAGEYAMA
 Researcher, Image Analysis Laboratory,
 Information and Communication Technology
 Division
 Research Areas: Computer Vision, Image
 Processing, 3D Point Cloud Processing



Nozomi NAGAMINE, Ph. D.
 Senior Chief Researcher, Head of Image
 Analysis Laboratory, Information and
 Communication Technology Division
 Research Areas: Computer Vision, Image
 Processing, Signalling Systems



Hiroki MUKOJIMA
 Researcher, Image Analysis Laboratory,
 Information and Communication Technology
 Division
 Research Areas: Computer Vision, Image
 Processing

Development of Automatic Train Operation System Based on Intermittent Type ATP with Continuous Speed Checks

Hiroyuki FUJITA

Signalling Systems Laboratory, Signalling and Operation Systems Technology Division

Takuya NOMURA

Signalling Systems Laboratory, Signalling and Operation Systems Technology Division (Former)

Takahiko AOYAGI

Kyushu Railway Company

Shunji MORITA

Nippon Signal Co., Ltd.

ATO (Automatic Train Operation) systems which are equipment for automated driving control under protection of ATC (Automatic Train Control), continuous type of ATP, is introduced in specific types of line, such as AGT (Automated Guideway Transit) systems or subway systems in Japan. There is a growing need for new type ATO system which is operated by a staff who is not required driver's license in order to reduce operating costs further. We have developed an ATO system based on ATS (Automatic Train Stop) -DK which is intermittent type ATP and equipped continuous speed check. In this paper, we show the concept of the ATS-based ATO system and report on the specifications of this system and functional field test results.

Key words: ATP, ATS, ATS-DK, ATC, automatic train operation, staff at the front end, fail-safe, GoA 2.5

1. Introduction

With a declining birthrate, aging population and shrinking working population, it is necessary to reduce the cost of train operations in order to maintain the railway network including local lines. One solution to overcome this problem is to introduce automatic train operation (ATO), with a view to achieving unattended train operation (UTO). In Japan, UTO and driverless train operation (DTO) that do not require drivers have already been operated in some automated guideway transit (AGT) lines and monorail lines. The current Japanese Technical Standard Ordinance assumes that DTO and UTO are performed by an ATO equipment within the control range of ATC which is a continuous transmission type ATP equipment. On the other hand, intermittent type ATP systems called ATS are installed on over 90% of conventional lines in Japan. Especially, in local lines, introducing ATC would entail a huge amount of investment cost, making the replacement of ATS unviable.

Since ATS transmits control information when a vehicle passes over ground beacons installed at specific points, there is a restriction that control information is not continuously transmitted like with ATC. However, ATS-DK which has been used from 2011 recognizes its own position continuously and generates permissible speed profile based on stop signal information and then line profile database that include speed limit section and so on, and checks the speed continuously [1]. Using ATS-DK, it would be possible to realize in conventional lines without the need to replace existing ATS.

Therefore, this research aims to realize automatization of driving operations in conventional lines by using the continuous type ATS. In addition, for operations on general conventional lines with level crossings, we aimed to realize the automatic operation where staff without a train driver's license attending at the front end of a train would be in charge of stopping operations and evacuation guidance in emergencies. This direction of work reflects forecast shortages of drivers and the need to reduce training and maintenance

costs.

This paper describes the outline of the functions of the ATS-based ATO system using ATS-DK and the results of functional tests using prototype equipment for mass-production.

2. Concept of automatic train operation based on ATS-DK

2.1 Grades of automation

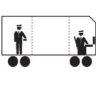


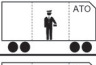

The grades of automation (GoA) are defined by IEC 62267: "Railway Applications – Automated Urban Guided Transport (AUGT) – Safety Requirements [2]." Currently, in the study group of Ministry of Land, Infrastructure, Transport and Tourism (MLIT), new type of the train operation, tentatively called GoA 2.5, of which concept is described in Chapter 1 is added as the topics [3]. Table 1 shows types of GoAs including GoA 2.5.

The ATO system based on ATS-DK is being developed as GoA 2.5. In this system, the staff at the front end would be in charge of such as an emergency stop operations in the event of obstacles found on tracks, train protection actions, and evacuation of passengers. ATO on-board equipment performs main operations conventionally performed by drivers. This system differs greatly from conventional ATO system in that it is characterized as using fail-safe devices for ATO on-board equipment, not just the ATS-DK on-board transceivers. In this paper, ATO on-board equipment in this system is called "FS-ATO." In other words, the new ATO meets safety requirements as a whole system combining FS-ATO and ATS-DK [4].

2.2 Preconditions

This system is based on an intermittent type ATP with continuous speed check called ATS-DK introduced in JR Kyushu general conventional lines. ATS-DK on-board transceiver detects train po-

Table 1 Classifications by types of staff assignment for railways (grade of automation)

| Grade of automation, GoA*1 | Images of types of staff assignment [main tasks of staff] | Status of introduction in Japan |
|--|---|---------------------------------|
| GoA 0 TOS: On-sight Train Operation |  | Trams |
| GoA 1 NTO: Non-automated Train Operation | | General lines |
| GoA 2 STO: Semi-automated Train Operation |  | Some subway lines |
| GoA 2.5*2 with staff at the front end |  | None |
| GoA 3 DTO: Driverless Train Operation |  | Some monorail lines |
| GoA 4 UTO: Unattended Train Operation |  | Some AGT lines |

*1 Definition according to IEC 62267 (JIS E 3802) "Automated urban guided transport (AUGT) – Safety requirements"

*2 GoA 2.5 is not defined in IEC 62267 (JIS E 3802)

sition continuously using an database of line profile and so on. Control information according to the signal aspect is transmitted to an on-board antenna from beacons when trains pass over them. By this information, on-board transceiver calculates the speed profile for a stop signal. Furthermore, it calculates speed limit profiles for curves or turnouts using the database. An outline of the ATS-DK control function is shown in Fig. 1. Although ATS-DK is an intermittent type ATP, it continuously checks train speed against the permissible speed, and outputs emergency brake command if the train speed exceeds the permissible speed.

In developing this system, we aimed to achieve automatic train control under precondition that currently used ATS-DK function should not be changed. Furthermore, we defined the following pre-conditions.

ATS-DK has two options to generate permissible speed profile. Simple option is that the speed profile is only generated when control information according to stop signal is received. However, in order to achieve required safety, another option that the speed profile is always generated is applied to this system. By this option, an end position of movement authority is set at next signal, even if the closest signal indicates proceed (green). In other words, the train always has the continuous permissible speed profile. Preconditions that relates to train operations are as follows.

- This system controls only trains on main lines, and other movement such as shunting are out of scope.
- Trains controlled by this system do not pass through stations.
- The length of a train is fixed to the maximum length of regular trains on the line.
- The stopping position at the station is the same regardless of trains.
- The system controls trains traveling forward only.

The staffs at the front end shall have the aptitude, knowledge, and skills necessary to perform tasks such as train protection and brake operation, and shall have received the training necessary to handle the automatic train operating equipment.

2.3 Purpose of new ATO system

Originally, ATS was designed as backup equipment assuming licensed train drivers are capable of appropriate driving operations. Generally, if the signal indicates stop (red), ATS on-board transceiver provides a warning and the driver performs the operation to stop

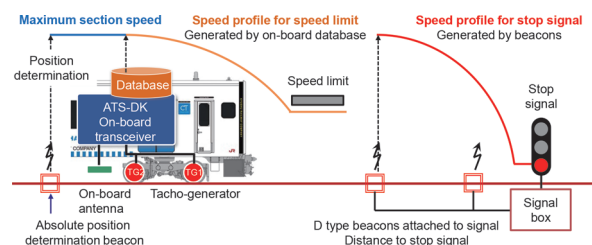


Fig. 1 Outline of ATS-DK control function

the train at the approach of the signal. Once the train stops and the driver performs the operation in the appropriate sequence, ATS permits the driver to operate the train at low speed while focusing on safety ahead. In other words, in the case of train operation using ATS, the driver plays a role in part of ensuring safety. However, the train must stop at the approach of the stop signal in any case relying only on the system to realize an automatic train operation.

On the other hand, as vehicles may not be running exclusively in automatic train operation sections but also in manual operation sections, ATS-DK basic functions must not be changed so as not to affect driver's task in the manual operation section. We thus aimed to apply proven fail-safe equipment (FS-ATO) to the on-board ATO system unlike with conventional ATC-based system. FS-ATO equipment complements the safety-related functions of the ATS-DK on-board transceiver and allows a control that compares favorably with ATC-based systems even though it uses intermittent type ATS. In other words, we developed a mechanism that assures safety required for an automatic train operation by the system that combines FS-ATO with ATS-DK, originally used fail-safe devices. This concept is our original, differs from conventional one, and we believe that our concept indicates one direction for realizing automatic train operation without the need to redesign existing ATS. Detail functions of the developed system are described in section 3.

3. System overview

3.1 System configuration

This system consists of existing ATS-DK equipment, newly added automatic train control equipment (FS-ATO and relay circuit

unit), and beacons for ATO system, as shown in Fig. 2. FS-ATO is equipment that generates a speed profile for train operation that becomes the target speed (hereinafter, “running speed profile,” green line in Fig. 2) based on a permissible speed profile (hereinafter, “DK speed check profile,” red line in Fig. 2) calculated by the ATS-DK on-board transceiver, and outputs powered running and braking commands based on the running speed profile. FS-ATO is fail-safe equipment with a same basic hardware configuration like the ATS-DK on-board transceiver. The DK speed check profile is constantly held by the ATS-DK on-board transceiver, and FS-ATO equipment performs two types of calculations: the running speed profile for speed control within the range of the DK speed check profile and another speed check profile by itself (hereinafter “ATO speed check profile,” blue line in Fig. 2). FS-ATO equipment has a function to output a maximum service braking (hereinafter referred to as “B7”) command if the train exceeds the running speed, thus achieving a speed control equivalent to that of ATC. The ATO speed check profile is set to the running speed profile plus 8 km/h, and FS-ATO outputs an emergency braking command if the train exceeds this check speed. The purpose of this function is to stop the train as soon as possible before the train speed reaches the DK speed check profile. Note that the functions for the ATO speed check profile calculation, output of B7 command and emergency braking command when the train speed exceeds the ATO speed check profile are executed independently from the ATS-DK on-board transceiver function. Furthermore, FS-ATO equipment calculates running distance by the same proven logic as in the ATS-DK on-board transceiver. Other devices installed for automatic train operation are an operating mode (automatic/ manual) selection switch, a running start request button, an emergency stop button, a trigger button for a short distance and low-speed movement, and a temporary speed limit setting switch. Meanwhile, beacons for ATS-DK (hereinafter, “DK beacons”) that can send digital messages in addition to the conventional resonance frequency, as well as TASC (train automatic stop control) beacons for controlling stop position in stations and two kinds of beacons for complementing ATS-DK’s functions are installed. The main functional composition of ATS-DK on-board transceiver and FS-ATO equipment is shown in Fig. 3. In this way, functions of ATS-DK and FS-ATO are combined in our system to ensure the required safety for an automatic train operation. For example, functions to complement ATS-DK are assigned to FS-ATO mainly to prevent SPAD by a systematic procedure.

3.2 Overview of train control

Figure 4 shows an image of basic running control by this system from departure to arrival, and the details of control per step are described below.

3.2.1 Departure after activation of ATO equipment

At the initial departure station (Station A in Fig. 4), after activation of on-board equipment or arrival at the designated position in the station by manual operation, the operating mode of the system is set to automatic. ATS-DK on-board transceiver generates speed check profile at 25 km/h and send the information that the transceiver is normal to FS-ATO equipment. FS-ATO equipment generates the running speed profile of 12 km/h subtracting 13 km/h from the 25 km/h. The staff at the front end confirms the departure time and that the departure signal indicates proceed (green), and he/she closes doors after passengers have boarded and presses the running start request button upon confirming safety on the platform and so on. As

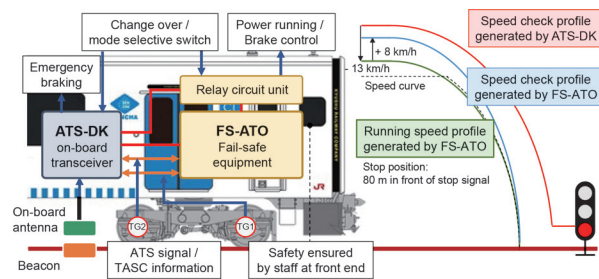


Fig. 2 System configuration of ATS-based ATO

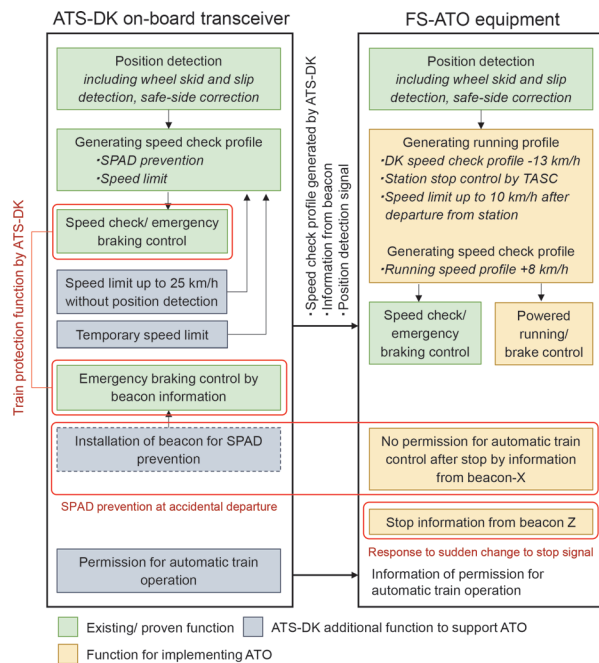


Fig. 3 Main functional composition of ATS-DK on-board transceiver and FS-ATO equipment

a result, the FS-ATO equipment outputs a powered running control command and performs speed control according to the running speed profile.

3.2.2 Position detection and running control according to control information from beacon

After departing from the initial station, the ATS-DK on-board transceiver clears the speed limit up to 25 km/h (see 3.2.1) and generates the DK speed check profile for the next signal by detecting position and receiving information of the proceed signal from the first beacon (beacon-B) in approach of the departure signal. Based on newly generated the DK speed check profile, the FS-ATO generates the running speed profile that will stop the train at 80 m before the next signal (green line in Fig. 4).

3.2.3 Stop control according to information from TASC beacons

Beacons to provide trains with control information to stop at a designated position in a station for ATO systems are called train automatic stop control (TASC) beacons in Japan. In this system, two pairs of TASC beacons. In other words, the number of it smaller

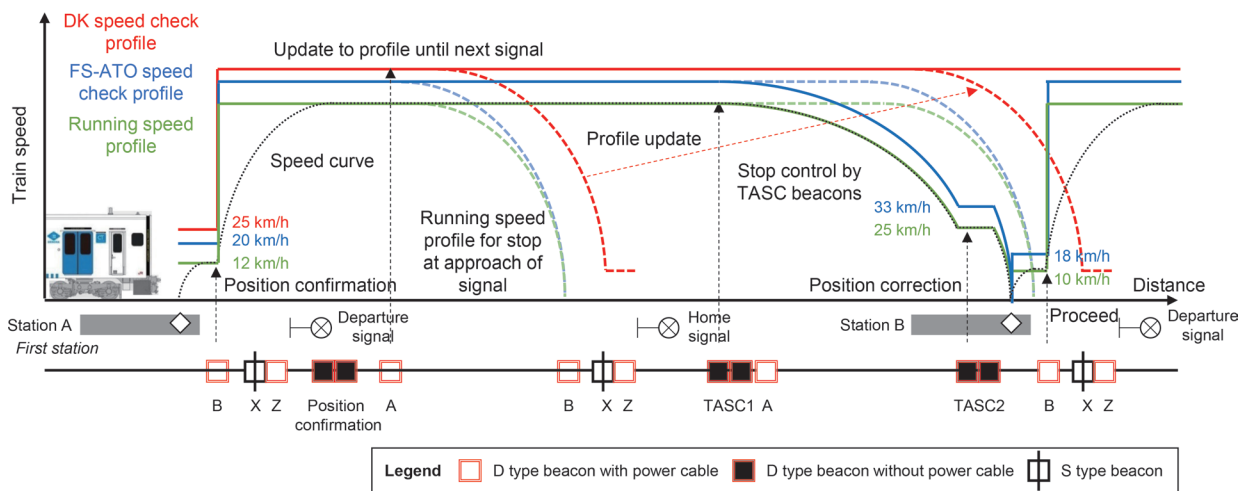


Fig. 4 Image of basic running control from departure to arrival station

than general ATO systems. Reasons are that main application target of this system is local line in which station platform screen doors would not be installed and allowable range of train stopping position is set to ± 2 m that is the same as the criterion of the driver's licensing test. FS-ATO equipment generates a TASC speed profile (green line in Fig. 4) by receiving information from TASC 1 beacon, and FS-ATO modifies the running speed profile when the train passes TASC 2 beacon. The train once decelerates to 25 km/h at 70 m before the stopping position and stops at the station by running speed profile based on information from TASC beacons. The reason for gradual deceleration is to stop at the station smoothly even if there is an error in running distance calculation due to the long distance between beacons.

3.2.4 Departure from station

After the staff at the front end confirms the departure time and so on, he/she presses the running start request button. FS-ATO equipment generates a running speed profile at 10 km/h until the information is received from the first beacon (beacon-B), regardless of the aspect of the departure signal (Station B in Fig. 4). This is so that the train can stop in approach of the signal even at an emergency stop command.

4. Comparison with ATC-based ATO

As described in Chapter 3, this system is based on ATS-DK which has the function of checking speed continuously, however, control information is received intermittently at locations where beacons are installed. On the other hand, ATC-based system can receive control information continuously via rails, and it differs greatly in terms of system configuration. The two main impacts of this difference are departure control from a stopped state and the response to sudden signal changes to stop in emergencies and the like. The functions described as follows are added in order to handle those. Although the system configuration is different, we consider that our new system, ATS-based ATO system, could provide the necessary safety compared to the ATC-based ATO.

4.1 Departure control from stopped state

When departing from a station or restarting after an unavoidable stop between stations, departure permission and signal information can be transmitted to the train immediately at any positions with the ATC-based ATO system. On the other hand, the train with the ATS-based ATO system cannot receive the latest information until it passes the next beacon. The train needs to move to the closest beacon to continue running. Meanwhile, a train must be prevented from entering an area protected by a stop signal, even if the staff at the front end accidentally presses the running start request button regardless of the stop signal being indicated. A countermeasure to this is to install a beacon (beacon-X in Fig. 4) to prevent SPAD in addition to the DK speed check profile up to 25 km/h and running speed profile at 10 km/h by FS-ATO equipment. FS-ATO equipment disables further automatic train operation if the train stops due to that information from beacon-X. Beacons installation conditions in relation to signals are as shown in Fig. 5. Taking into account the deceleration performance of applicable vehicles, a beacon-X is installed 30 m ahead of a signal as a rule.

4.2 Response to situations when sudden indication of the stop signal

In this system, locations where control information can be obtained are limited in contrast to ATC-based ATO which performs continuous transmission. Thus, beacons (beacon-Z) are installed immediately in front of a signal to prevent trains entering an area protected by a stop signal without obtaining control information to stop if the signal aspect suddenly changes to stop in situations such as emergencies. This control information from a beacon-Z shown in Fig. 5 only affects FS-ATO's function, so it plays the role of outputting emergency braking commands after receiving stop information. Depending on train locations and speeds when an event envisioned here of sudden changes to stop signal occurs, the train may proceed into the protection area of the signal even with the ATC-based ATO system. In such a situation, the functions of interlocking equipment and block equipment ensure that there are no other trains on the track and that no conflicting route is set. Furthermore, after the train enters the protection area of signal, safety is ensured by detecting the train by the track circuit. If the control information according to stop signal is received from this beacon, FS-ATO equipment out-

puts an emergency braking command and generates a running speed profile at 10 km/h after stopping. The running speed profile is subsequently replaced by new profile which is generated when control information according to proceed signal is received from the next beacon.

5. Tests for verifying the functions

Tests for verifying functions of the ATS-based ATO system were carried out with prototype equipment for mass-production to verify the functional specifications of the system. This chapter describes the procedure and results of the tests.

5.1 Test procedure

In the verification test of the system, 217 items to be evaluated were selected as the contents covering safety under normal and abnormal conditions and safety against operating errors. As shown in Table 2, these tests were divided into four phases which are the test in the manufacturer's factory, the test with stationary train, the test with running train in the depot and the test with running train in the actual line. The test in the manufacturer's factory was carried out with prototype equipment alone, and after the test with stationary train, the test vehicle (BEC819 series 2-car train) equipped with various switches and buttons was used. Figure 6 shows an image of the installed equipment. The test to reproduce equipment failure and handling in abnormal conditions was mainly carried out in the test with running train in the depot. On the other hand, the tests for items that are difficult to be reproduced on actual equipment were carried out in combination with the simulator in the manufacturer's factory. The test with running train in the actual line was conducted for the purpose of confirming the functions in conditions that the train runs at operation speed and ground equipment are installed at actual layout with the beacons for the ATS-based ATO system installed on commercial lines. Whether each function operates according to the specifications was verified by analyzing the operation status record data of the ATS-DK transceiver and the FS-ATO equipment. In the operation status record data, the ground beacon reception status, relay input / output status, speed / distance integration status, various speed profile control status, and so on, were recorded in 100 ms cycles.

5.2 Test results

As a result of the verification test, the recognition accuracy of the own train position is within the permissible value, and the driving control by the operation profile generated by the FS-ATO equipment was executed without any problem. We also confirmed that the information from newly added beacons for ATS-based ATO system can be received appropriately by the on-board equipment and the system functions were performed in accordance with the specifications. Through the verification tests, we confirmed safety in normal and abnormal situations and safety against erroneous operation, and the results indicates that our system can be used without any problems in practical use.

Among the results of the verification test, the details of distance calculation accuracy and stop position accuracy, which are the prerequisites for control function verification and automatic driving control, are shown below.

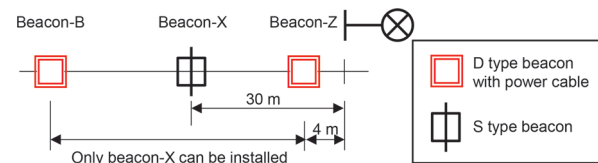


Fig. 5 Beacons installation conditions on relation to signals

Table 2 Outline of verification test

| Phase | Test type | Location | Contents |
|-------|--------------------------------|-----------------------------------|--|
| 1 | Test in manufacturer's factory | Manufacturer's factory | Functional verification with simulator |
| 2 | Test with stationary train | Rolling stock depot | Combination test with vehicle, Input / output confirmation |
| 3 | Test with train in depot | Rolling stock depot | Basic function, reproduction anomaly in test track |
| 4 | Test with train in actual line | JR Kashii Line between 3 stations | Basic function, reproduction anomaly in commercial line |

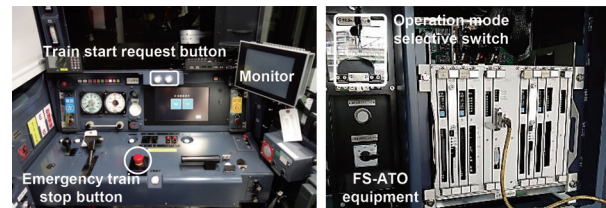


Fig. 6 Image of installed equipment

5.2.1 Automatic driving control function

In each test, we confirmed the functions that operation mode selection, external input such as information from beacons and switches, and the control function using the on-board database. In Fig. 7, an example of the control state when the train departs from the first station is shown. Figure 7 shows that each speed profile with speed limited up to 25 km/h, 20 km/h, and 12 km/h were generated when the train does not detect its position, and that the train detects the position when pass over first beacon. It also shows that the power running and the brake notch were controlled according to the various speed limits, and the train runs in accordance with speed profile generated by FS-ATO. By checking the control status in this way, it was confirmed that there is no problem in practical use.

5.2.2 Distance calculation accuracy

The distance calculation algorithm of this system is same as that has been proven by actual record of ATS-DK on-board transceiver. Therefore, when verifying the accuracy of the distance calculation, we confirm that it should be $\pm 3\%$ or $\pm 4\text{ m}$ or less with respect to the distance between beacons, which is the allowable error margin of the ATS-DK system. The maximum error margin for distance is within 3% if the interval between beacons is over 133 m and 4 m if under 133 m. We performed verification of the accuracy to all the beacons used in the running test in the depot and in the actual line by comparison with the measured distance between the beacons in advance and the calculated distance by the FS-ATO equipment. As a result of the comparison, the distance calculation

error for the measured distance was within the reference values of $\pm 3\%$ and ± 4 m. In some cases, the reference value was exceeded when both axles to which a speed generator was attached skidded at the same time. Even when the reference value was exceeded, it was confirmed that all calculated distance values larger than actual distance, safe side, and that the train position and various speed profiles were corrected based on the newly received beacon information in accordance with the specification.

5.2.3 Stop position accuracy

FS-ATO equipment generates TASC profiles based on the distance to the stop position received from the TASC beacons and stops the train near the stop sign. In this system, the allowable range of stop positions is set to ± 2 m from stop signs. As the results of verification by actual measurements of the stop position for 68 running tests in the main line, we confirmed that all the vehicles were stopped within the specified range.

6. Conclusions

This paper described the concept of the ATS-based ATO system and reported on the specifications of this system and the results of tests. We think that the safety of the entire system including the ATS system can be ensured by making the ATO on-board equipment the same configuration as the proven fail-safe device with ATS-DK on-board equipment, and by adding the control function. We believe that our concept indicates one direction for realizing an automatic train operation without redesigning of existing ATS.

On December 24, 2020, proving runs started on the JR Kyushu Kashii Line with licensed drivers aboard using this system. In future, qualification requirements for the staff at the front end will be examined in the light of discussions at the “Railway Automated Driving Technology Study Group” of the MLIT. Additionally, it is expected that operating costs will be reduced by introducing this system as a so-called GoA2.5 compatible autonomous driving system.

Authors



Hiroyuki FUJITA
Senior Researcher, Signalling Systems Laboratory, Signalling and Operation Systems Technology Division
Research Areas: Signalling Systems, Automatic Train Protection, Reliability



Takuya NOMURA
Researcher, Signalling Systems Laboratory, Signalling and Operation Systems Technology Division (Former)
Research Areas: Signalling Systems, Reliability



Takahiko AOYAGI
Deputy Manager, Transportation Safety Department, Railway Operations Headquarters, Kyushu Railway Company
Research Areas: Automatic Train Operation



Shunji MORITA
Assistant Manager, Advanced Railway System Development Department, Nippon Signal Co., Ltd.
Research Areas: Automatic Train Protection, Automatic Train Operation

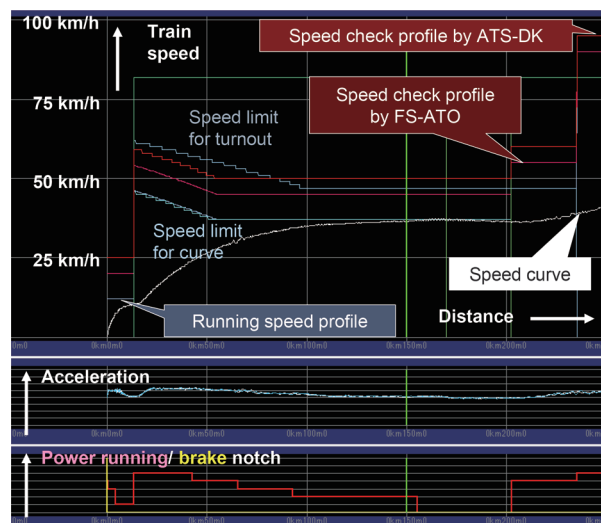


Fig. 7 Example of control state at departure from first station

References

- [1] H. Fujita, H. Arai, K. Sato, “Development of New Type Automatic Train Protection ATS-Dx with Permissible Speed Profile Using On-board Database,” *QR of RTRI*, Vol. 51, No. 4, pp. 189–195, November 2010.
- [2] IEC 62267: 2009, “Railway Applications – Automated urban guided transport (AUGT) – Safety requirements,” International Electrotechnical Commission, 2009.
- [3] Study Group on Automatic Operation Technology for Railways, “2019 summary (main text),” https://www.mlit.go.jp/tetudo/tetudo_fr1_000058.html, (accessed June 1, 2021).
- [4] T. Aoyagi, “Development of ATS (Automatic Train Stop)-based automatic train operation system using FS-ATO,” *Proceedings of STECH 2021*, Chiba, Japan, November 23–25, 2021.

Study of Anomalous Characteristics Exhibiting Between Fixing Force of Switch and Tongue Rail Opening Force

Shunsuke SHIOMI

Signalling Systems Laboratory, Signalling and Operation Systems Technology Division

Yoshikazu OSHIMI

Kentaro TSUBAKI

Signalling Systems Laboratory, Signalling and Operation Systems Technology Division

Ken TAKASAKI

Terutaka SATO

Signalling Systems Laboratory, Signalling and Operation Systems Technology Division (Former)

The tongue rail opening force of a turnout is measured to indirectly estimate the fixing force of a turnout. Although tongue rail opening force is known to be proportional to the fixing force, it is also known that the proportional relationship sometimes does not hold. This non-proportionality can lead to mis-estimation of the fixing force, in turn causing malfunction of the switch due to the high fixing force. In order to solve this problem, we clarified the mechanism and causes of the mis-estimation related to contact between rails. The results of field investigations and motion simulation using a flexible multibody model of switch, were used to developed maintenance methods and a measurement tool for avoiding mis-estimation.

Key words: opening force, fixing force, closure between rails, switch, point machine

1. Introduction

Closure between the stock rail and tongue rail of a turnout is highly related to running safety of vehicles passing through a turnout. Therefore, the locking devices and locking mechanism of a point machine have to tightly fix the tongue rail (blade) against the stock rail. This fixing between rails occasionally loosens due to lateral displacement of the stock rail and the tongue rail. When this occurs, lock rods of the point machine detect this insufficiently fixed condition as a locking malfunction. The detection of this malfunction ensures the safety of a train passing through the turnout but disrupts train operations. It is therefore important to reduce the frequency of this malfunction to ensure operational stability. Thus, the fixing between rails should be checked by periodical maintenance and the actual method for checking the fixing status is also important.

Since most electric point machines in Japan have internal locking mechanisms, the status of the fixing force acting between the tongue rail and the stock rail is generally used to indirectly manage the closure and fixing status. The fixing force is supported by the point machine and acts on the switching bar of the turnout. The fixing force can be measured as the strain of devices between the throw bar on the point machine and the switching bar. It has been established empirically that the fixing force is proportional to the tongue rail opening force. Although the method for measuring the strain for a permanent monitoring device had been developed, this method has not been used yet commercially in Japan because of the need for periodical calibration of the strain sensors. Therefore, the fixing force between the rails is measured indirectly during periodical maintenance work on point machines by using the tongue rail opening force. The maximum and minimum strength range of the tongue rail opening force is stipulated in a maintenance rule. The indirect measurement of the fixing force using the tongue rail opening force normally gives the appropriate fixing force to be set in most turnouts. However, it has also been shown empirically that anomalous characteristics, i.e., non-proportionality, is exhibited between the fixing force and the opening force in some turnouts. This character-

istic may cause the switch to malfunction, since the fixing force is adjusted to be larger than the switching force of a point machine, even if the opening force is normal. That is one of the problems related to the difficulty of maintaining point machines.

This paper reports on the results of experimental investigations and analyses the relationship between the tongue rail opening and fixing forces and its effect according to the type and condition of a turnout. We also report that the anomalous characteristics of the forces are affected by a contact position between the stock rail and the tongue rail. Moreover, we propose a new measurement tool and method, to avoid mis-estimation of the fixing force.

2. Fixing force and tongue rail opening force

2.1 Fixing force

The fixing force acts on a tongue rail as the elastic force in a switch adjuster and switching bar to ensure the tongue rail is tight against the stock rail. It is responsible for maintaining the position of the tongue rail so that the gap is closed between rails when a lateral force acts from wheels. To achieve this, the fixing force is empirically adjusted to 1 kN in a hinged heel switch. The fixing force can also be adjusted to be stronger. However, a strong fixing force exceeding the maximum switching force of the point machine may cause the switch to malfunction, and a strong fixing force may also wear of parts in the point machine and the rods. Accordingly, it is important to adjust the fixing force to within a proper range.

Figure 1 shows the fixing force action and related forces on the point machine and the rods including the switch adjuster and the switching bar. The internal locking mechanism of the electric point machine and the escapement crank in switching mechanisms for large turnouts, including high-speed rail turnouts, maintain a relative position against the stock rail because they are locked into position with fixing bolts and plates. The fixing force is affected by elasticity of the rods and tongue rail between both fixed ends, which are the switching bar in an electric point machine and the contact

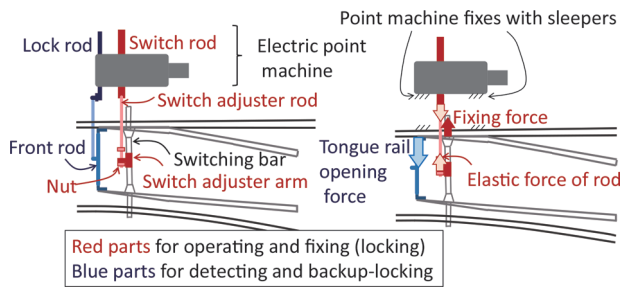


Fig. 1 Fixing force and tongue rail opening force

point on a stock rail. The strength of the force is mainly adjusted with the distance between one end of switch adjuster rod, which connects with the point machine or the escapement crank, and the adjustable nut facing to the arm connected to the switching bar. The fixing force can be measured as strain of the switch adjuster rod and the jaw pin. A jaw pin with strain sensor for testing of switch and permanent condition monitoring methods of the fixing force and switching load [1] had been already developed. However, these methods have not been used yet in commercial permanent monitoring systems because of problems related to periodical calibration and durability of sensors.

2.2 Tongue rail opening force

The tongue rail opening force is the force acting on a tool when the toe of a tongue rail is opened from the stock rail. Since the opening force is known to be empirically proportional to fixing force, the fixing force is determined by the measured opening force. There are many kinds of measurement and methods for determining the opening force. Some inspectors use measurement devices, while others measure the force manually. On the other hand, maintenance rules for railway operators specify a range for the measured strength of adherence, which indicates when the points can be considered to be in good condition.

Figure 2 shows an example of a method for measuring the opening force using a measurement device. Inspector A operates the device for measuring the tongue opening rail force to open the toe of tongue rail, and inspector B measures the opening width between the tongue rail and the stock rail using a thickness gauge. Inspector B checks the opening width by inserting a thickness gauge between the rails or a pull-out from the rail of the thickness gauge. Inspector A confirms an indicated opening force on the device at the moment when the opening width reaches the thickness of the gauge. The thickness of the gauge is 1.0 mm in case of hinged heel switches and 0.5 mm in case of flexible switches. Although the range of the open-

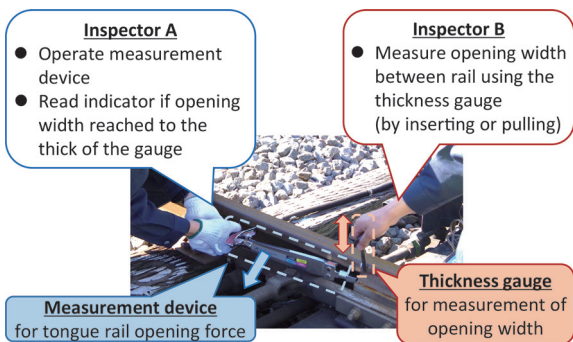


Fig. 2 Example of method for measuring tongue rail opening force

ing force differs from railway operators and the type of turnout, it is normally specified as 2.0 kN to 2.7 kN maximum.

2.3 Problems in fixing force management using opening force measurement

To identify problems in fixing force management using opening force measurement, a questionnaire survey was conducted among maintenance companies doing measurement works of the opening force. Table 1 shows the results of a survey to identify difficulties encountered by inspectors. The results indicate that inspectors believed that same turnouts had different opening force and the opening force was influenced by the measurement devices, inspectors, method of measurement and season when inspections were conducted. Moreover, it was reported that for some turnouts it was difficult to satisfy the specified range of opening force and specified clearance between the tongue rail and the stock rail at once. In case of such turnouts, the fixing force was strongly adjusted to satisfy the specification of clearance of rails.

In addition, it has been shown that some turnouts present anomalous characteristics where the opening force is empirically smaller than the expected force on the basis of the relationship between the normal fixing force and opening force. This anomalous characteristic may induce a switching malfunction in a turnout even when the opening force is adjusted to satisfy the specified range, because the fixing force exceeds the switching force of the point machine.

These issues and characteristics are problems for fixing force management based on opening force.

3. Experimental investigations

In order to clarify actual states of the problems managing the fixing force based on opening force measurements, we experimentally investigated the relationship between the forces and other parameters.

3.1 Investigation methods

Table 2 shows numbers of the turnouts investigated in the field by type and shape of turnouts. These turnouts were measured and investigated in the field for opening force, fixing force and gaps between the rails. The opening force was measured with the same opening force measurement device used by railway operators. The fixing force was measured with the strain gauge equipped with a jaw pin, which was a normal jaw pin taken from one end of a switch adjuster. The characteristics between the fixing force and the open-

Table 1 Result of questionnaire survey (selected)

| Type of measurement device | Type A shown in Fig. 1 | Other Types | Manual measurement with wrench |
|------------------------------------|---|-------------|--------------------------------|
| (N=19, multiple responses) | 19 | 1 | 9 |
| Maintenance works related problems | a) Differences depending on who is inspecting and conditions of front rod b) In some locations, the guard (check) angle makes inspection difficult c) Results influenced by different gauge insertion methods and positions d) With some switches, when the opening force is within the specified range, the rail gap fails to meet requirements | | |

Table 2 Types and numbers of field investigations

| (Numbers) | Hinged heel switch | | | | Flexible switch | | Turnout for Sliding | Special Turnout | Total |
|-------------------------------------|--------------------|-----|-----|-----|-----------------|-----|---------------------|-----------------|-------|
| | 30k | 37k | 40N | 50N | 50N | 60k | | | |
| Simple turnout | 1 | 4 | 14 | 21 | 15 | 9 | 1 | 1 | 92 |
| Symmetrical turnout | 0 | 0 | 2 | 4 | 5 | 0 | 0 | | |
| Asymmetrical turnout | 0 | 1 | 3 | 4 | 2 | 2 | 0 | | |
| Curved turnout (same direction) | 0 | 0 | 0 | 1 | 0 | 0 | 0 | | |
| Curved turnout (opposite direction) | 0 | 0 | 2 | 0 | 0 | 0 | 0 | | |

ing force (referred to below as FOC) were measured by adjusting the fixing force at the switch adjuster nut. Gaps between a tongue rail and a stock rail were measured to investigate the effect of the contact position of the rails on the FOC. These measurements were normally done in both directions of a switch (Normal and Reverse). The opening width at the toe of a tongue rail at the opening force measurement is 0.5 mm for flexible switches and 1.0 mm for hinged heel switches normally. Note, if an opening occurred at the toe of the tongue rail before measurement, the width before opening was added to the measurement width.

Moreover, the FOCs were measured when contact positions between the rails were changed for a hinged heel turnout with 50 N rail [2] in RTRI to investigate the effect of the contact position of the rails on the FOC. On the same turnout, the FOCs were measured to investigate the influence of different inspectors and opening force measurement methods, which was claimed by inspectors to influence the opening force, including insertion position of the thickness gauge and insertion angle of the measurement device.

3.2 Effect of types and shapes of turnout

Figure 3 shows the field investigation results for the FOC on hinged heel switches and flexible switches. Since measured results of hinged heel switches are highly dispersed, it is difficult to think that the opening force of all measured hinged heel switches are proportional to the fixing force. However, it is possible to contend that the FOC of each turnout is proportional to the fixing force, focusing on the result of each turnout A to E. Since slopes of hinged heel turnouts and y-intercepts are different for each turnout, the opening force does not appear to be proportional to the fixing force.

Figure 4 shows the FOCs of hinged heel turnouts by shapes of turnouts, size, rail types and configurations of switching rods and cranks. These results confirmed that turnout shape, size and rail type do not affect the FOC. Meanwhile, the FOC with the configurations using two cranks differed from the FOC with the other configurations: in the configuration using two cranks, the opening force was the same, but the fixing force was stronger than in the other configurations.

Figure 5 shows configurations of switching rods and cranks for large turnouts. A configuration with two cranks shown in Fig. 5 (a) fixes a tongue rail to a stock rail by two switch adjuster rods. For this configuration, a fixing force of the second switch adjuster is transmitted from second crank to first crank and first switch adjuster directly, because a normal crank has no locking function to hold fixing force by itself. It is possible to contend that this transmission of fixing force from second switch adjuster relates to a special tendency of the FOC of 1:16 turnouts shown in Fig. 4 (b). The FOC of this configuration without the effect of a fixing force of a second switch adjuster is shown in Fig. 4 (d). It was confirmed that this FOC is as

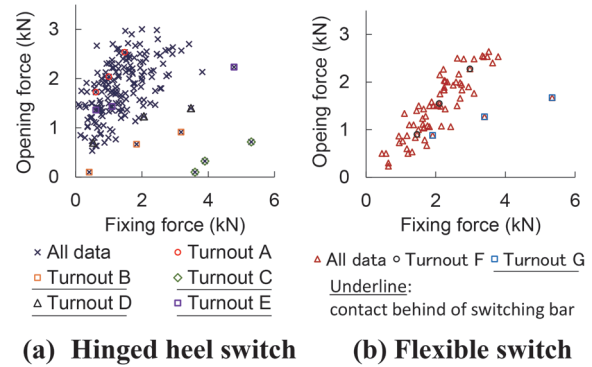


Fig. 3 Results of the field investigation (fixing and opening forces characteristics: FOC)

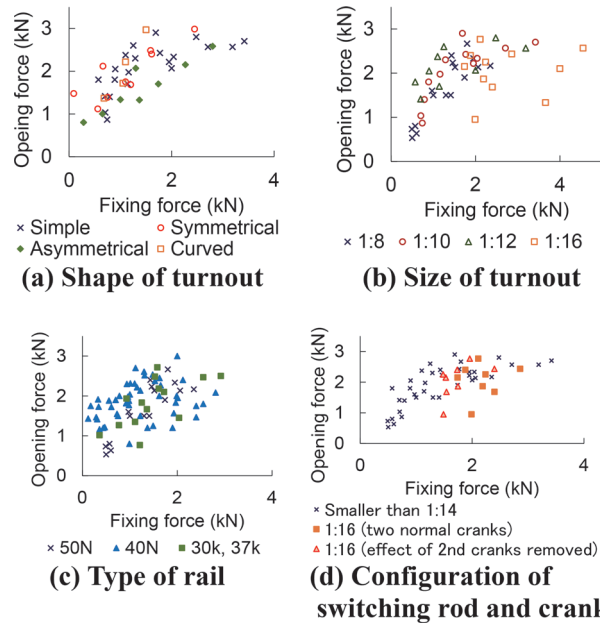


Fig. 4 FOCs by type and shape of turnout

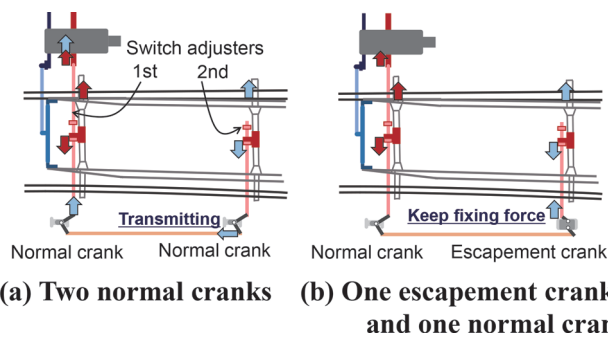


Fig. 5 Configurations of switching rods and cranks for large turnout

same as the FOCs of the other configurations. Furthermore, since an escapement crank holds the fixing force itself, the FOC of the configuration shown in Fig. 5 (b) is as same as the others.

3.3 Effect of contact position of rails

In order to investigate the effect of the contact position of the

tongue rail and the stock rail on the FOC, FOCs at two different contact positions A and B were measured at the same turnout. Figure 6 shows the FOCs at contact positions A and B. Contact position A, which is the position between toe of tongue rail to a switching bar, is considered to be a “good contact position.” On the other hand, contact position B, which is the position behind a switching bar, is normally considered to be a “bad contact position.” The results show that for contact position A, FOC increases with the fixing force, but for contact position B, FOC has little correlation with the fixing force.

This tendency is also true for the results of the field investigation shown in Fig. 3. The characteristic that increases with increasing fixing force of the FOC in turnouts B to E, where the contacts are behind the rolling rods, is smaller than in the case of turnouts A and F. Table 3 shows the average, median and standard deviation of y-intercepts and the slopes, when FOCs of each flexible switches are linearly approximated, for each type of contact. The slopes and y-intercepts have some dispersion in each turnout. However, focusing on median, it is found that the slope of the cases for contacting on the position behind the switching bar is smaller than other results. Meanwhile, no significant difference was found at y-intercepts. This tendency may explain why the dispersion of y-intercepts is not affected by contact positions and structures of turnouts.

3.4 Effect of measurement method of tongue rail opening force

The opening force was measured by two inspectors who normally use an opening force measurement device and a thickness gauge, respectively.

One inspector operates the device to open the toe of the tongue rail, while the other checks the opening width between the tongue rail and the stock rail using a thickness gauge. They confirm an indicated opening force on the device at the moment when the opening width reaches to the thick of the gauge. However, details of the measurement method, such as a measurement method of the opening width by the thickness gauge, measurement position of the width, were not specified in the working procedure. To clarify the relationship between the measurement methods and the dispersion

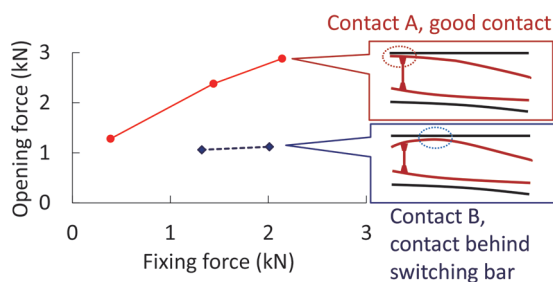


Fig. 6 FOCs by contact position between tongue rail and stock rail

Table 3 Slopes and y-intercepts of linear approximation of FOC by contact position

| (kN) | Slope of OFC | | | y-intercept of OFC | | | Number of samples |
|---|--------------|--------|----------|--------------------|--------|----------|-------------------|
| | Mean | Median | σ | Mean | Median | σ | |
| Contact at toe | 1.13 | 1.01 | 0.61 | 0.66 | 0.75 | 0.6 | 34 |
| Good contact (Toe is closed, contact is available at a section between toe and switch bar) | 0.91 | 0.83 | 0.43 | 0.5 | 0.46 | 0.58 | 13 |
| Toe is open, contact at a section between toe and switch bar | 0.7 | 0.69 | 0.22 | 0.85 | 0.85 | 0.52 | 4 |
| Contact behind of switch bar | 0.36 | 0.33 | 0.09 | 0.43 | 0.63 | 0.88 | 5 |

of the measured value, we experimentally studied the effect of changing the conditions of the inspectors and measurement methods on the opening force measurement result using the same turnout.

Figure 7 shows effects of inspectors A to E on FOCs. All inspectors who worked on this test were researchers of RTRI, and the same turnout and device were used. Figure 7 (a) shows the effect of an inspector who used same measurement device on FOCs, and Fig. 7 (b) shows the effect of an inspector who uses same thickness gauge on FOCs. The dispersion of the opening force when measured with the same measurement device used by different inspectors on the same fixing force was within 0.4 kN which is as near as the result of a same inspector of 0.2 kN. Meanwhile, the dispersion of the opening force measured by different inspectors using a thickness gauge on same fixing force was 1.0 kN maximum, however dispersions of the opening force when a same inspector used the thickness gauge was normally within 0.2 kN. By the results of this test, we confirmed that measured opening force was related to different inspectors using a thickness gauge. We also confirmed that the maximum difference of 1.0 kN had a non-negligible effect on the strength of the fixing force, which is around 1.0 to 3.0 kN.

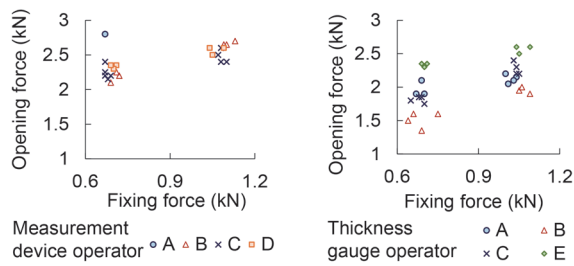
Figure 8 shows effects of measurement methods on the FOCs. Figure 8 (a) shows the effect of insertion positions of the thickness gauge, and Fig. 8 (b) shows the effect of the insertion angle of the measurement tool. These tests confirmed that the measurement method affects the values of the measured opening force, and we also confirmed importance of specifying the measurement method of the opening force on a working manual.

4. Causes and effects of contact position of rails against the tongue rail opening force

In order to experimentally clarify the causes and effects of anomalous FOC relating to the contact position between rails shown in section 3.2, a dynamics model of the switch considering the relationship between the fixing force and the opening force was developed. Moreover, the relationship between the FOCs and contact position of the rails was calculated using this model on a dynamics simulator for a turnout and switching devices developed by RTRI [3].

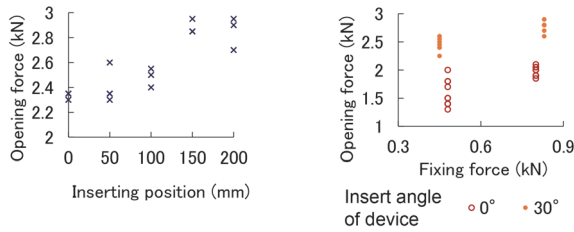
4.1 Modeling of mechanisms of the fixing force and the opening force

Figure 9 shows the relationship between the forces acting on a turnout and switching devices from when the rails is fixed by the fixing force to when the tongue rail is opened by the opening force. The relationship suggests that the fixing force of the rails relates to a constraint force on the end of the tongue rail (a), an elastic force of the tongue rail (b) and an elastic force of the switch adjuster (c). In addition, this relationship also suggests that the opening force re-



(a) Change for measurement device operator (b) Change for thickness gauge operator

Fig. 7 Effects of inspector against FOCs



(a) Insert position of thickness gauge (b) Insert angle of measurement device

Fig. 8 Effects of measurement method against FOCs

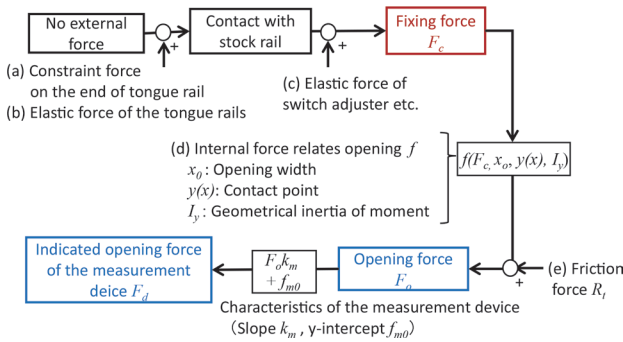


Fig. 9 Relationship between forces acting on a turnout and switching devices

lates to the fixing force acting on the switching bar, an internal force (d) and friction forces (e) between the tongue rails and bed plates on the sleepers. The internal force relates to the opening width of the tongue rail and contact point between the rails.

If the tongue rail has no contact point, the relationship between forces can be defined as an elastic deformation of a static beam [3]. Since, in a real turnout, one or more contact points are occasionally found on the tongue rail, and positions and numbers of the contact points move dynamically, it is difficult to analyze the relationship of the forces using a static beam model. To solve it, we modified the multi body dynamics model and simulator for a turnout and switching devices developed by RTRI which considers the forces relating the fixing force and the opening force. Moreover, the effects of the contacting position of the rails on the FOCs, motion of rails and related forces were computed using the model and simulators.

Parameters assuming a hinged heel 1:8 simple turnout, were used for the simulation. In the simulation, motion and forces were calculated when the turnout switched its direction and when the tongue rail was opened 1.0 mm by the opening force measuring device, to confirm the relationship between the FOCs against fixing

forces and contact positions.

4.2 Result of simulation and effect of contact position on the FOCs

We simulated the FOCs and geometry of the tongue rail with two different contact positions between the tongue rail and the stock rail. One of them was a contact at the toe of the tongue rail which is a normal contact, and the other was a contact at 0.6 m behind the toe of the tongue rail which is behind the switching bar. Figure 10 (a) shows the simulation results of the FOCs, and Fig. 10 (b) shows the simulation results of the gap between the rails also showing of the geometry of top view for the tongue rail.

The simulation results showed that the anomalous FOC is confirmed when a contact exists behind the switching bar, and this tendency is as same as the investigation results. Moreover, the simulations also calculated the opening force and related forces such as the elastic forces and the fixing force. When the toe of the tongue rails is opened in 1.0 mm for measuring the opening force, the fixing force directly acts on the opening force at the case of a normal contact, because there is no supporting point of the force on the tongue rail except for the toe. On the other hand, the fixing force acts on the toe of the tongue rail and the contact point, when the contact point is available behind the switching bar. Since the fixing force is supported at those two points, the opening force is smaller than normal contact even if in same fixing force. By this mechanism, it is considered that increasing of the FOC is smaller than increasing of the FOC of the normal contact when a contact point of the rails is available behind the switching bar.

4.3 Results of simulation and effect against geometrical inertia of moment of tongue rail

Parameter studies using the simulator showed that a lateral geometrical inertial of moment (referred to below as LGIM) of the tongue rail relates to the FOC, because a LGIM relates to a geometry of the tongue rail and the contact points. Figure 11 shows the simulation results of the FOCs against LGIMs and the geometries of the tongue rail. On the simulations, a contact point is set at the toe of the tongue rail. However, it was confirmed that the slope of the FOC decreases when LGIMs are 25% and 50% of that of the 70S rail used in 50N rail turnouts. The results shows that low LGIM tongue rails tend to come into contact with the tongue rail behind the switching bar when the opening force is measured, since low LGIM rails bend easily.

These results showed that a main cause of the anomalous FOC is an effect of the contact position of the rails behind the switching bar. Moreover, we also confirmed that the contact position is affected by the geometry of the tongue rail, width between the tongue rails

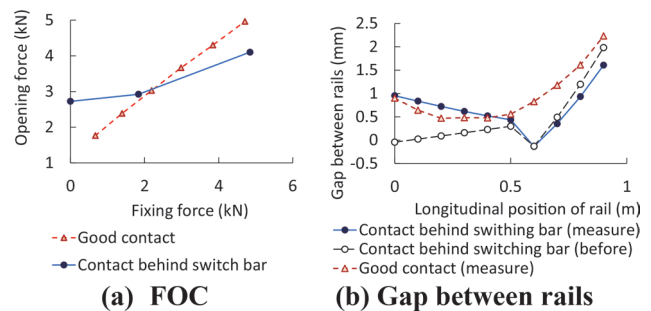


Fig. 10 Simulation results of effect of contact points

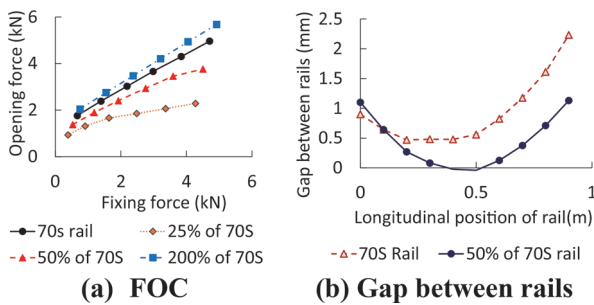


Fig. 11 Simulation results of effect of geometrical inertia of moment

adjusted by the width of the front-rod, and LGIM of the tongue rail. Since LGIM of turnouts normally used in main tracks and sidetracks range between 71% to 214% of LGIM in a 50N turnout, the effect of the difference in LGIM on the FOCs is small (within $\pm 10\%$). Therefore, a specification of opening force can be applied for different types of turnouts. However, for example, a special turnout having low LGIM characteristics, such as a single tongue rail for dividing direction of the dual gauge track to a broader gauge track and a narrower gauge track, may have an anomalous FOC. Considering these characteristics, it is necessary to specify an opening force range within which the fixing force is considered normal.

5. Proposal for an adjustment and measurement method for opening forces

The procedures and contents of the fixing force using opening force measurement devices were conducted in accordance with railway operator maintenance manuals. An opening force range used for determining the state of health of an opening force and the thickness of the thickness gauge are specified for hinged heel switches and flexible switches, respectively.

Our investigations confirmed the basis of current regulations whereby the FOC is nearly stable regardless of size, shape and type of rail in the turnout. However, we also confirmed the highlighted problems in the current regulation, which are that the FOC is affected by contacts between rails and the position and method used to make measurements.

Table 4 shows the proposed modifications to the measurement methods in the current maintenance manual, based on the investigation described in this paper. Figure 12 shows a flowchart of the maintenance work reflecting our proposal. To avoid strong fixing forces due to adjustment of the opening force to a regulated range for a turnout with rails making contact behind the switching bar, a

Table 4 Current maintenance manual regulations and proposals for modification

| Current measurement method regulations and <u>proposals from this study</u> (<u>underlined</u>) |
|---|
| <ul style="list-style-type: none"> Opening force should be adjusted in following range [Hinged heel turnout] X to Y kN in 1.0 mm opening [Flexible turnout] Z to W kN in 0.5 mm opening If there is a gap before the measurement is taken, the width of the opening should be added to the gap (i.e., gap is 0.3 mm, opening width is 1.3 mm in hinged heel turnout) The device should be inserted N mm behind the toe of the tongue rail Thickness gauge should be inserted, and opening force should be measured if the gauge pulls out The opening force device should be inserted parallel to the rail |

task was added, which is to check for contact between rails before measuring the opening force. To reduce the dispersion of measurement results due to individual differences between inspectors and measurement methods, we proposed clarifications to the method used to measure the opening force, such as how the device should be inserted, the position of the thickness gauge, and type of measurement device.

For turnouts with a gap on the toe of the tongue rail before opening, the problem is that the opening force is often found to be weaker than in normal turnouts. The problem occurs because the opening width of the tongue rail, defined by thickness of the gauge, is affected by the pre-opened gap, and becomes smaller than specified opening width of 1.0 mm or 0.5 mm. To avoid this problem, the thickness of the gauge was adjusted in our investigations using relative displacement as the specified width. The modified maintenance method shown in Table 4 suggests adding the gap width before measuring to avoid this problem.

Moreover, a device assisting the opening width measurement was developed to solve problems related to opening width measurement. Figure 13 shows the developed device which measures relative displacement of the tongue rail and warns the inspector when a measured width reaches a specified opening width. This device is still under development for practical use, and it is expected it will replace opening width measurements using a thickness gauge.

6. Conclusions

We conducted field tests and analyses to investigate the relationship between the tongue rail opening force and the fixing force, and the impact of type and condition of the turnout. On the basis of the results obtained from these tests and analyses, the characteristics

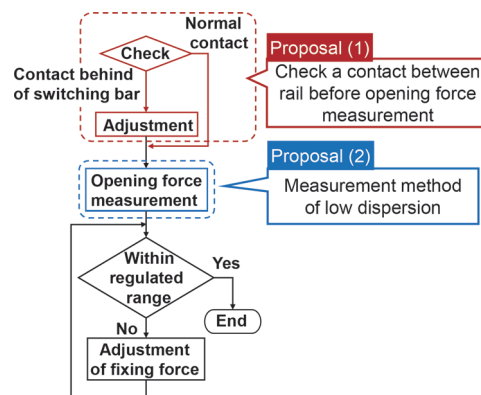


Fig. 12 Proposal for work flow of opening force measurement

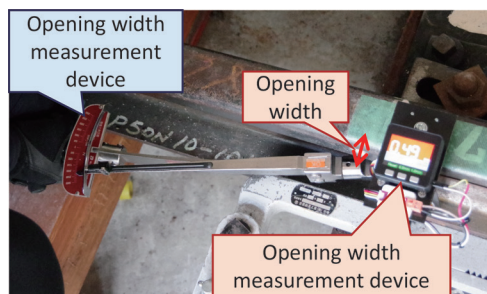


Fig. 13 Opening width measurement device (Prototype)

of the fixing force and the opening force are summarized as follows.

- The anomalous characteristics of forces are affected by a contact position between the stock rail and the tongue rail. The anomalous characteristics were confirmed when there was contact behind the switching bar.

- The anomalous characteristics were also confirmed when lateral geometrical inertial of moments were 25% and 50% of that of a 70S rail used in 50N rail turnouts.

Moreover, we proposed a new measurement tool and method to avoid the mis-estimation of fixing forces. We hope that the results of this investigation and proposed method and tools contribute to improving maintenance work on switches, point machines and related devices.

Acknowledgment

The authors thank the staff of the Hokkaido Railway Company,

East Japan Railway Company, and Kyushu Railway Company for their indispensable work on testing at their turnouts and suggestions related to adjustment works.

References

- [1] Shiomi, S., Igarashi, Y., et al., "Monitoring method for a switching load of spring point machines," *RTRI Report*, Vol. 25, No. 5, pp. 23-28, 2011 (in Japanese).
- [2] Japanese Standard Association, "Flat bottom railway rails and special rails for switches and crossings of non-treated steel," JIS E 1101:2001.
- [3] Shiomi, S., Oshimi, Y., et al., "Analysis of an object detection function of a turnout and a switch machine," *Transactions of the JSME*, Vol. 84, No. 681, p. 17-00568, 2018.

Authors



Shunsuke SHIOMI
Senior Researcher, Signalling Systems Laboratory, Signalling and Operation Systems Technology Division
Research Areas: Point Machine, Signalling Devices



Ken TAKASAKI
Researcher, Signalling Systems Laboratory, Signalling and Operation Systems Technology Division
Research Areas: Signalling Devices



Yoshikazu OSHIMI
Assistant Senior Researcher, Signalling Systems Laboratory, Signalling and Operation Systems Technology Division
Research Areas: Point Machine, Signalling Devices



Terutaka SATO
Researcher, Signalling Systems Laboratory, Signalling and Operation Systems Technology Division (Former)
Research Areas: Signalling Devices



Kentaro TSUBAKI
Researcher, Signalling Systems Laboratory, Signalling and Operation Systems Technology Division
Research Areas: Signalling Devices

Evaluation of Material Properties of Pantograph Contact Strip by Microscopic Structure Model

Fumiko MORIMOTO Yoshitaka KUBOTA
Frictional Materials Laboratory, Material Technology Division

Most frictional materials used in railways are made of composite material, and their macroscopic material properties are largely affected by their microscopic structure. It is useful to clarify the relationship between microscopic structure and material properties by numerical simulation for effective improvement or development of the materials. In this study, we developed an image-based microscopic model by using X-ray computed tomography for a metalized carbon pantograph contact strip material and evaluated its Young's modulus, thermal conductivity and electrical resistivity based on the homogenization method. The calculated material properties were more consistent with the experimentally measured values than the estimated values based on the classical Voigt model. We also introduce the analysis result of the stress, temperature and current density distribution in the microscopic model.

Key words: pantograph contact strip, Cu-impregnated carbon, homogenization method, X-ray CT, finite element method

1. Introduction

Most frictional material used in railways such as pantograph contact strips and wheel tread brakes are made of composite material. It is well known that macroscopic properties of the composite material largely depend on their geometric microscopic structure such as size, shape and distribution of their constituents. Conventionally, railway materials have tended to be developed experimentally by trial and error. However, to make the process of material improvement or development more effective, it would be useful to clarify the relationship between a material's microscopic structure and macroscopic material properties by numerical simulation.

In recent years, despite the increased use of various simulation methods to assist material design, few methods have been applied for railway materials. One example for railway material does exist, which is the application of atomic scale methods such as molecular orbital methods and molecular dynamics methods to evaluate the behavior of materials [1]. However, it is difficult to interpret macroscopic phenomena using an atomic scale model. In this study, we attempted to model composite material in a micro-meter scale structure and develop a method to calculate the material properties to be compared with macro-scale values. The procedure of the method is shown in Fig. 1. Firstly, a three-dimensional microstructure of a sample of a contact strip is visualized using high-resolution X-ray computed tomography (CT). Secondly, a part of the CT images obtained is extracted as a region for modeling. The extracted region is segmented into each constituent material, and then meshed to make an FEM model. Finally, the material properties are calculated using the homogenization method [2].

This paper describes the results of applying the method to metalized carbon, which is one of the pantograph contact strip materials (Chapter 2 to 5). Using the microscopic model, the stress, temperature and current density distribution in the microscopic model are also calculated (Chapter 6).

2. Material

The material used in this study is a metalized carbon (PC78A, manufactured by Toyo Tanso Co., Ltd.), which is widely used for pantograph contact strips on Japanese railway lines. This material is made by impregnating porous carbon with copper and is regarded as almost isotropic. Figure 2 shows the material structure of PC78A by an optical microscope. The yellow parts are copper, the black parts are voids, and the other gray parts are carbon.

Table 1 shows the material properties of PC78A and the volume fraction of each component estimated from the bulk density.

3. Observation of microstructure by X-ray CT

3.1 Observation method

The microstructure of PC78A was observed by X-ray CT. Table 2 shows the X-ray CT measurement conditions. SkyScan 2211 (Bruker Corporation) was used.

A schematic diagram of X-ray CT is shown in Fig. 3. It irradiates the sample with X-rays and detects the transmitted X-rays to

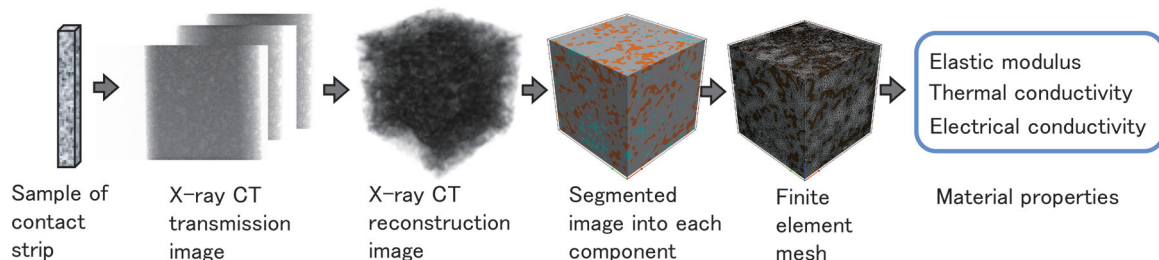


Fig. 1 Procedure for modeling using X-ray CT and calculating material properties

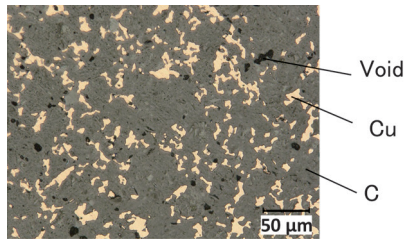


Fig. 2 Material structure of PC78A

Table 1 Material properties and volume fraction of each component of PC78A

| Young's modulus (GPa) | Poisson's ratio | Thermal conductivity (W/mK) | Electrical resistivity ($\mu\Omega\text{m}$) | Volume fraction (%) | | |
|-----------------------|-----------------|-----------------------------|--|---------------------|-------|------|
| | | | | C | Cu | Void |
| 28.8 | 0.23 | 13.9 | 1.26 | 78~85 | 15~20 | 1~4 |

know the internal structure. Since the X-ray transmittance depends on the density and atomic number of each constituent material, the two-dimensional transmission image visualized by the detector reflects the internal structure of the sample. By rotating the sample to collect transmission images from multiple directions and reconstructing the images by computer, a three-dimensional image of the sample can be obtained. The brightness of the grayscale image corresponds to the X-ray transmittance at each position in the sample. The higher the transmittance, the lower the brightness, and the lower the transmittance, the higher the brightness.

Table 2 X-ray CT imaging condition

| Sample size (mm) | Tube voltage (kV) | Detector | Voxel spacing of image (μm) |
|------------------|-------------------|------------|--|
| 2×2×10 | 110 | CCD camera | 1 |

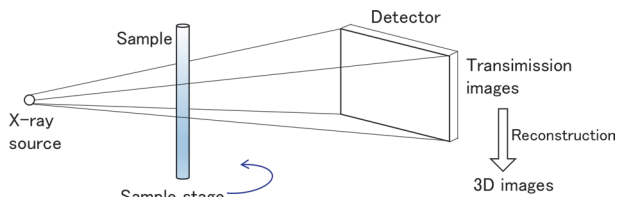


Fig. 3 Schematic diagram of X-ray CT

3.2 Result of observation

Figure 4 shows a part of the 3D and 2D image of PC78A. The white parts seem to be mainly copper, the black parts seem to be mainly voids, and the gray parts seem to be mainly carbon. But the boundary between the void and carbon is unclear. Since the black parts also have a continuous brightness distribution as will be described later, the black parts may contain low-density carbon in addition to void.

4. FEM modeling based on X-ray CT image

4.1 Modeling method

First, in order to reduce the image processing time, the image

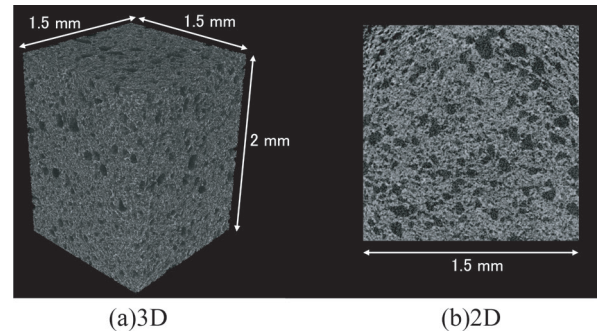


Fig. 4 X-ray CT image

resolution was lowered by changing the voxel spacing of the image from $1\ \mu\text{m}$ to $3\ \mu\text{m}$, and then a median filter was applied to remove the impulse noise of the image. After that, a cube with a side of $600\ \mu\text{m}$ was extracted from the CT image as a region representing the microscopic structure. Next, the image was segmented into voids, carbon, and copper regions on the basis of the difference in their X-ray transmittance. The threshold value of the image brightness was set so that each segmented region would have the volume fraction shown in Table 1. Each segmented region was composed of many connected parts with various size of volume. Since the connected part with a small volume will generate many finite elements on the subsequent meshing process, the part connected with less than 10 voxels in the void region and the part connected with less than 50 voxels in the copper region were reassigned as carbon regions. By meshing the carbon and copper regions, an FEM model was created (hereinafter referred to as model 600). FEM models with a side of $300\ \mu\text{m}$ (hereinafter referred to as models 300① to 300⑧) were also created to evaluate the difference in the volume fraction of the model and the accompanying physical property values depending on the extraction position from the CT image. These models were created by dividing the area of the above model 600 into eight as shown in Fig. 5. Simpleware (Synopsys, Inc.), 3D image processing software, was used for the above image processing and meshing.

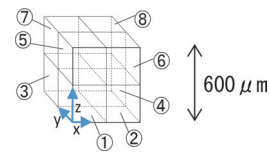


Fig. 5 Positional relationship between model 600 and models 300① to ⑧

4.2 Result of modeling and discussions

Figure 6 shows the image brightness histogram of the cubic region of the model 600 as frequency on the vertical axis and brightness on the horizontal axis. Note the range of brightness assigned to voids, carbon, and copper is also shown on the horizontal axis. Figure 7 shows an image segmented into the void, carbon, and copper regions and a microscopic structural model of 300①. The cross-sectional segmented image is shown in Fig. 8 together with the microstructure photograph by an optical microscope, although it is a different sample from the CT-imaging sample shown in Fig. 7. The volume fractions of each component after meshing for each model are shown in Table 3.

As shown in Fig. 6, the boundaries in brightness between voids,

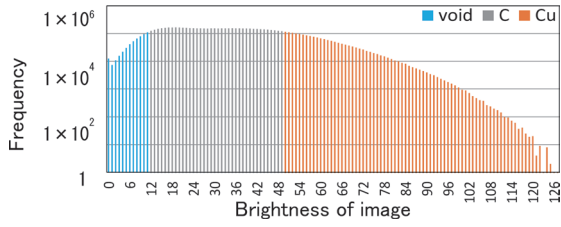


Fig. 6 Histogram of brightness of X-ray CT image with assignment of brightness range to each component

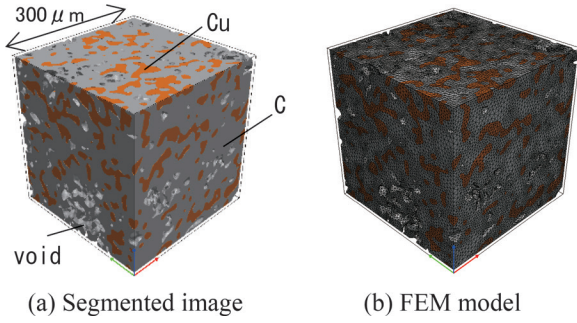


Fig. 7 Example of segmented image to components and FEM model

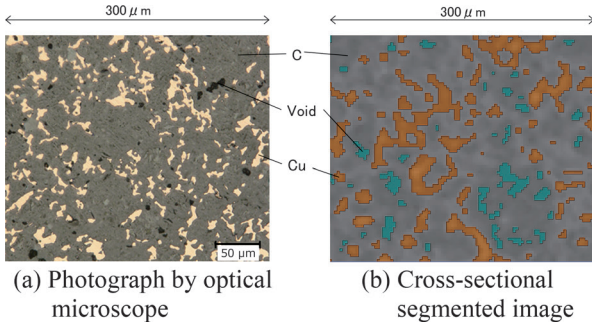


Fig. 8 Comparison of material structure photograph and cross-sectional segmented image

Table 3 Volume fraction and calculated material properties of each model

| Model | Volume fraction(%) | | | Material property | | | |
|----------------|--------------------|-------|------|------------------------|-----------------|------------------------------|-------------------------------|
| | C | Cu | Void | Young's modulus E(GPa) | Poisson ratio ν | Thermal conductivity λ(W/mK) | Electrical resistivity ρ(μΩm) |
| 600 | 79.83 | 15.70 | 4.47 | 28.12 | 0.23 | 16.10 | 0.79 |
| 300① | 79.47 | 14.83 | 5.70 | 26.97 | 0.23 | 14.58 | 0.98 |
| 300② | 75.25 | 19.89 | 4.86 | 29.76 | 0.23 | 24.82 | 0.38 |
| 300③ | 79.37 | 16.46 | 4.17 | 29.07 | 0.23 | 18.10 | 0.65 |
| 300④ | 80.16 | 14.75 | 5.09 | 26.95 | 0.23 | 14.38 | 0.91 |
| 300⑤ | 81.69 | 14.48 | 3.82 | 27.93 | 0.23 | 13.44 | 1.19 |
| 300⑥ | 82.01 | 14.97 | 3.02 | 28.65 | 0.23 | 13.84 | 1.18 |
| 300⑦ | 84.04 | 12.58 | 3.38 | 27.61 | 0.23 | 12.41 | 1.30 |
| 300⑧ | 82.87 | 12.19 | 4.94 | 25.98 | 0.23 | 11.39 | 1.43 |
| Average 300①-⑧ | 80.61 | 15.02 | 4.37 | 27.86 | 0.23 | 15.37 | 0.85 |

carbon, and copper are not clear, and multiple components may be in the same brightness region. However, even with the simple segmentation method using the brightness threshold shown above, the obtained model had a distribution and volume fraction of each com-

ponent close to the actual material as shown in Fig. 8 and Table 3. Comparing the volume fractions of model 600 and models 300① to 300⑧ from Table 3, the average values of models 300① to 300⑧ are close to the values of model 600, but the volume fractions of copper of models 300① to 300⑧ vary widely from 12% to 20%. These variations occur due to structural non-uniformity by the extraction position of the model in the sample. Although the variation due to the position can be reduced by increasing the modeling area, it is considered that the material properties of PC78A can be evaluated reasonably in feasible calculation time by using the average value of eight 300 μm size models.

In creating an image-based model of a material, the larger the size of the modeling area, the smaller the effect of material non-uniformity. However, as the size of modeling area increases, the computational load for image processing and material property calculation increases. Hence, it is necessary to determine the appropriate size of the modeling area according to the structural characteristics and purpose of calculation.

5. Calculation of material properties by homogenization method

5.1 Calculation method

Figure 9 shows a schematic diagram of the homogenization method. In the method, it is assumed that the inhomogeneous material has a periodic microstructure, and the scale of the microstructure is sufficiently smaller than that of the macroscale. Considering that the microscopic structure is replaced with a homogeneous material having the same properties, the equivalent material properties of the inhomogeneous material are obtained.

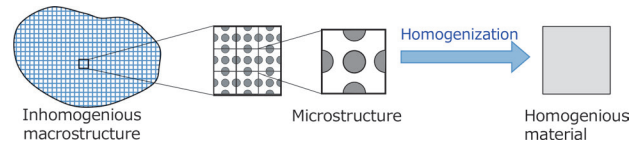


Fig. 9 Schematic diagram of homogenization method

The elastic constants of replaced homogeneous material D_{ijkl} are derived by (1), where y is the coordinate in the microscopic structural model (region Y) and $E_{ijkl}(y)$ (each index=1,2,3) are the elastic constants at y [2].

$$D_{ijkl} = \frac{1}{|Y|} \int_Y \left(E_{ijkl}(y) - E_{ijmn}(y) \frac{\partial X_m^{kl}}{\partial y_n} \right) dy \quad (1)$$

The characteristic displacement function X_m^{kl} in (1) is obtained by solving (2) under periodic boundary conditions.

$$\int_Y E_{ijmn}(y) \frac{\partial X_m^{kl}}{\partial y_n} \frac{\partial \delta u_i}{\partial y_j} dy = - \int_Y E_{ijkl}(y) \frac{\partial \delta u_i}{\partial y_j} dy \quad (2)$$

where δu_i is virtual displacement. For isotropic materials as PC78A, the elastic constants are reduced to two components, Young's modulus and Poisson's ratio.

The thermal conductivity and electrical conductivity can be also derived by the same method. For the microscopic structure model created in Chapter 4, the homogenization analysis of (1) and

(2) was performed to calculate the material properties using Simpleware module.

To calculate the material properties of PC78A by (1), the material properties of carbon and copper are required. For copper, the nominal value was used. For the carbon parts of PC78A, which are polycrystalline carbon and contain micro voids below the resolution of X-ray CT, a suitable value cannot be determined from the relevant literature. In general, the material properties of polycrystalline carbon greatly depend on the raw material, manufacturing process, heat treatment temperature, density, void ratio and crystal orientation. Furthermore, the material properties of carbon part only cannot be measured experimentally.

Therefore, the material properties of the carbon part were estimated by the carbon substrate before impregnation with copper. Specifically, a model of the carbon substrate was created using only the carbon part of the CT image of PC78A in Chapter 4, and the material properties of carbon were determined so that the calculated material properties of the carbon substrate model by the homogenization analysis would reproduce the measurements.

The material properties of copper and carbon were applied to the PC78A model and homogenized analysis was performed to calculate the material properties of PC78A.

5.2 Results of calculations and discussions

Table 4 shows the estimated material properties of carbon by homogenization analysis using the model of carbon substrate. Table 4 also shows the material properties of copper used for the analysis below.

Some measurements and estimates of carbon material properties are described in several documents. For example, the Young's modulus of an isotropic pyrolytic carbon is experimentally 13.5 GPa and theoretically 16 to 74 GPa [3]. The thermal conductivity is 6 to 420 W/mK for a polycrystalline graphite [4]. The electrical resistivity is estimated to be 2.2 to 234 $\mu\Omega\text{m}$ corresponding to the thermal conductivity 6 to 420 W/mK by the relationship between the thermal conductivity and the electric resistance for the artificial graphite [5]. The estimated material properties of carbon in Table 4 are considered reasonable because they are within the range of these literature values.

Table 3 shows the results of calculated material properties of each model of PC78A by the homogenization method with the values in Table 4.

Table 4 Material properties of carbon and copper for analysis

| | Young's modulus (GPa) | Poisson's ratio | Thermal conductivity (W/mK) | Electrical resistivity ($\mu\Omega\text{m}$) |
|----|-----------------------|-----------------|-----------------------------|--|
| C | 24 | 0.22 | 3.8 | 38.46 |
| Cu | 118 | 0.33 | 391 | 0.0171 |

Figure 10 shows the relationship between the volume fraction of copper and calculated material properties together with the measured values in Table 1. The larger the ratio of copper, the higher the Young's modulus (the slope of linear regression is 0.43 GPa/%) and thermal conductivity (the slope of linear regression is 1.7 W/mK/%), and the lower the electrical resistivity (the slope of linear regression is -0.14 $\mu\Omega\text{m}/\%$). Compared to Young's modulus, thermal conductivity and electrical resistivity depend more on the volume fraction of copper. The difference based on the influence of the

copper ratio can be considered to be due to the difference in the ratio of the material property value of copper and carbon. That is, this is because the Young's modulus of copper is 5 times that of carbon, the thermal conductivity of copper is 110 times that of carbon, and the electrical resistivity of carbon is 2250 times that of copper.

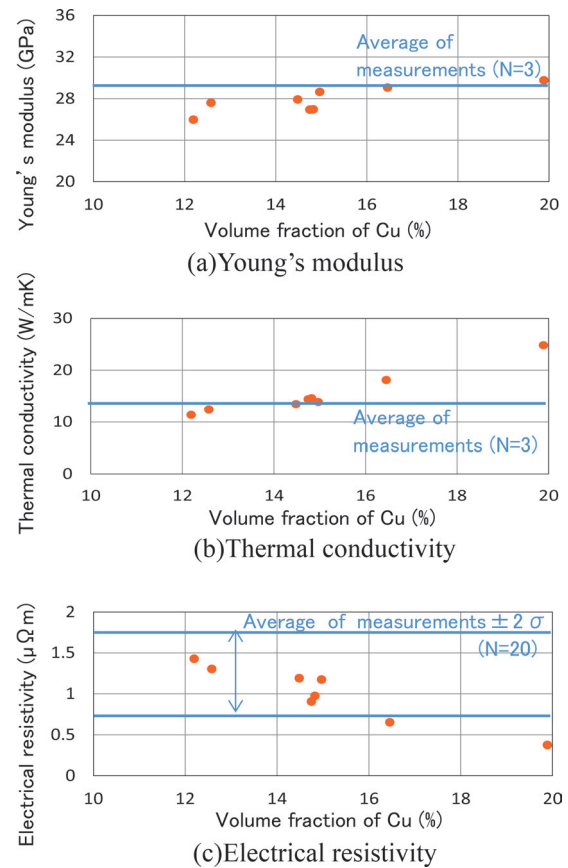


Fig. 10 The relation between volume fraction of copper and material properties

As shown in Fig. 10, in the range of the volume fraction of copper of 12% to 16%, each calculated material property is close to the measured value.

Figure 11 shows the average of calculated material properties for models 300 ① to ⑧ (indicated as "Hom." in figure) in comparison with the measured values (indicated as "Exp." in figure) and the estimated values by the classical rule of mixture based on the Voigt model [6] (indicated as "Mix." in figure), which estimates the material properties by the volume fraction of the constituents. The calculated values by the homogenization method are closer to the measured values than the values by the rule of mixture. This result is because the rule of mixture uses only the volume fraction of the components, whereas the homogenization method reflects the microscopic structure such as the arrangement and shape of each component in addition to the volume fraction.

6. Other analysis examples of the microscopic model

The pantograph contact strip slides along the contact wire while collecting electrical current. Therefore, in addition to the mechanical load caused by the contact with the contact wire, the con-

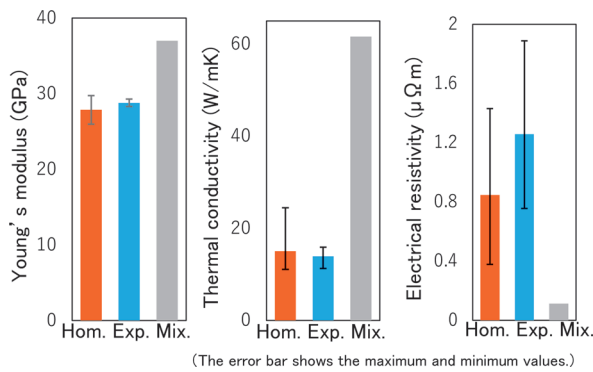


Fig. 11 Comparison between estimated and measured material properties.

tact strip is subject to Joule heat caused by energization, and thermal load by arc discharge when the contact strip is separated from the contact wire. The distribution of stress and temperature in the contact strip can be calculated by FEM analysis using a macro model with homogeneous material properties. However, a more detailed distribution considering the inhomogeneity of the material will be necessary to understand the frictional phenomenon near the surface. Therefore, we calculated the distribution of stress, temperature, and current density on μm scale using a microstructural FEM model, to which the boundary conditions were given.

6.1 Calculation method

Model 300④ described in the previous chapter is used. The stress distribution is calculated by structural analysis, and the temperature and current density distribution are calculated by thermal analysis with Joule-heat. The material constants in Table 4 are used for the analysis. The boundary conditions for structural analysis are shown in Fig. 12 (a). The bottom is completely restrained, and a pressure simulating the contact force with the contact wire is applied to the top. A static analysis is performed assuming the conditions shown in Table 5.

The boundary conditions for thermal analysis with Joule-heat are shown in Fig. 12 (b), and the assumed conditions are shown in Table 6. Since the contact wire is placed in a zigzag manner with respect to the rail direction, the contact position between the contact wire and the contact strip moves left and right on the strip in the sleeper direction. Under the conditions shown in Table 6, the contact

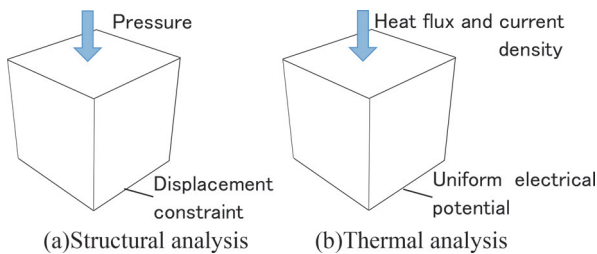


Fig. 12 Boundary conditions

Table 5 Assumed conditions for structural analysis

| | |
|------------------------------|-----|
| Width of strip (mm) | 33 |
| Contact width with wire (mm) | 1 |
| Contact load (N) | 64 |
| Contact pressure (MPa) | 1.9 |

Table 6 Assumed conditions for thermal analysis with Joule-heat

| | | |
|--|-------------------------------------|----------------------------------|
| Width of strip (mm) | h | 33 |
| Contact width with wire (mm) | w | 1 |
| Running speed (km/h) | v | 100 |
| Contact pressure (N) | P | 64 |
| Electrical current (A) | I | 200 |
| Frictional coefficient | μ | 0.2 |
| Electrical contact resistivity (m Ω) | R | 20 |
| Frictional heat (W) | $Q_f = \mu P v$ | 356 |
| Joule heat due to electrical contact resistance (W) | $Q_R = R I^2$ | 800 |
| Distribution ratio of frictional heat to the strip | α_f | 0.2 |
| Distribution ratio of Joule heat to the strip | α_R | 0.8 |
| Total amount of heat to the strip (W) | $Q = \alpha_f Q_f + \alpha_R Q_R$ | 711 |
| Lateral speed of contact position with wire on the strip (m/s) | v_L | 0.22 |
| Heat flux (W/m 2) | $q(t) = Q \cdot f(t) / (w \cdot h)$ | $2.2 \times 10^7 \times f(t)$ ** |
| Current density (A/m 2) | $i(t) = I \cdot f(t) / (w \cdot h)$ | $6.1 \times 10^6 \times f(t)$ ** |
| Contact time with wire at a certain position on the strip (ms) | $t_q = w / v_L$ | 4.5 |

** $f(t)$ is shown in Fig. 13.



Fig. 13 Time dependence of heat flux and current density

time of the contact wire at a certain position on the strip is 4.5 ms. Therefore, a transient analysis was performed by applying the time-dependent heat flux and current density shown in Fig. 13 to the top of the model. The initial temperature is 20°C, the potential on the bottom is 0 V, and the target time of transient analysis is 6.5 ms.

6.2 Results and discussions

Figure 14 (a) shows the model used, and Fig. 14 (b) shows the equivalent stress distribution in the model. The stress in the copper region was higher than that in the carbon region because the Young's modulus of copper is higher than that of carbon.

Figure 15 (a) and (b) show the temperature distribution and current density distribution at $t = 5$ ms. The temperature distributions are also shown in Fig. 15 (c) and (d), which are divided into copper regions and carbon regions. The temperature of the carbon regions was higher than the copper regions. It is considered that the heat transfer from the top surface to the bottom surface is slower in the carbon region because the thermal conductivity of carbon is lower than that of copper. The electrical current mainly flows in the copper region since copper has a higher electrical conductivity than carbon.

It is difficult to directly observe and measure the distribution of temperature near the friction surface on a microscopic scale. Hence, the estimation of it expected to be useful for understanding phenomena such as wear, damage, and deterioration due to friction.

In this study, the results are qualitative because only the cube region with a side of 300 μm is modeled and the boundary conditions are directly imposed on the model. In order to make a quantitative estimation on a micro scale, it is necessary to obtain the physical quantity distribution in the micro region inside the macro model that simulates the actual phenomenon. For that purpose, it is not feasible to model the entire strip with a mesh of μm size, but it is reasonable to perform zooming analysis using another macro model or to use a model in which only a part is meshed on a microscale.

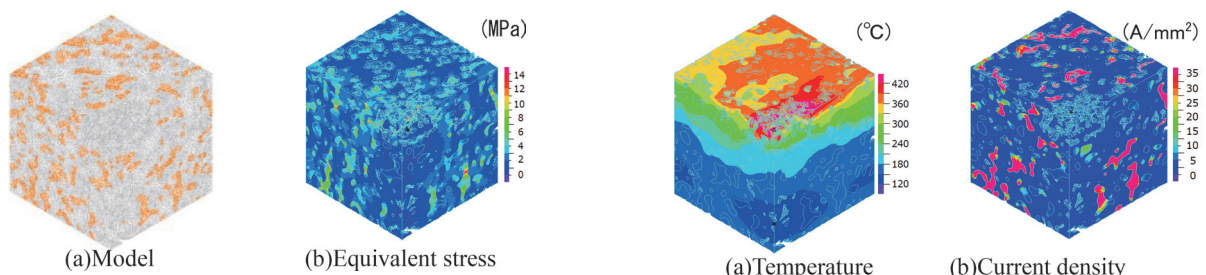


Fig. 14 Model and the equivalent stress distribution

7. Conclusions

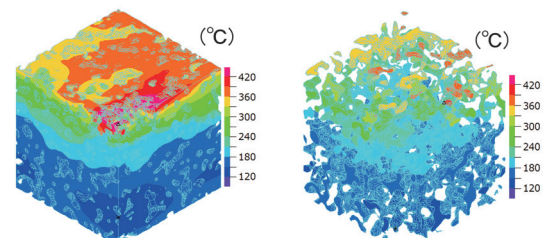
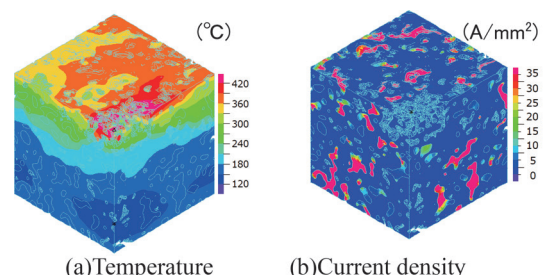
We constructed a method to calculate the material properties of copper-impregnated carbon using a microstructure model using X-ray CT images. The results are summarized as follows:

- (1) X-ray CT imaging was performed to obtain a three-dimensional microscopic structure.
- (2) A microscopic structural model based on X-ray CT images was created.
- (3) Using the created model, the Young's modulus, thermal conductivity and electrical resistivity were calculated by the homogenization method. The calculated values were closer to the measured values than those from the estimation by the rule of mixture.
- (4) The distributions of stress, temperature and current density in micro-meter scale were calculated by finite element analysis using the model.

The calculations using the microscopic model enable the estimation of the material properties before their trial production in the material development process and the proposal of the material structures having more desirable properties.

References

- [1] Iwafuchi, K., "Basic Study on the Application of the Computer Simulations for Material Designs and Estimations," *RTRI Re-*



(c)Temperature in C region (d)Temperature in Cu region

Fig. 15 Temperature and current density distribution

- port*, Vol. 8, No. 9, pp. 43-48, 1994 (in Japanese).
- [2] Guedes, J.M. and Kikuchi, N., "Preprocessing and postprocessing for materials based on the homogenization method with adaptive finite element methods," *Computer Methods in Applied Mechanics and Engineering*, Vol. 83, No. 2, pp. 143-198, 1990.
- [3] Price, R.J., "Young's Modulus of Pyrolytic Carbon in Relation to Preferred Orientation," *Phil.Mag.*, 12, p. 561, 1965.
- [4] Jamieson, C.P. and Mrozowski, S., Proc. *1st and 2nd Conf. on Carbon*, Univ.Buffaro Press, p. 155, 1956.
- [5] Mason, I.B., and Knibbs, R.H., "The thermal conductivity of artificial graphite and its relationship to electrical resistivity," *UKAEA Report R3973*, 1962.
- [6] Šarlošič, J. and Bocko, J., "Effective Material Moduli for Composites," *American Journal of Mechanical Engineering*, Vol. 4, No. 7, pp. 289-292, 2016.

Authors



Fumiko MORIMOTO
Senior Researcher, Frictional Materials
Laboratory, Material Technology Division
Research Areas: Frictional Materials,
Computational Mechanics



Yoshitaka KUBOTA
Senior Researcher, Frictional Materials
Laboratory, Material Technology Division
Research Areas: Frictional Materials,
Electrical Contact

Moisture Behavior in Concrete Repaired by Patching Observed with Neutron Imaging

Hiroaki SUZUKI Motoki UEHARA
Concrete Materials Laboratory, Materials Technology Division

Maki MIZUTA Yoshie OTAKE
RIKEN Center for Advanced Photonics

The cross sectional repair of concrete structures is carried out for the purpose of restoring or improving durability. However, some re-deterioration, such as corrosion of reinforcing bars, floating of repair materials, or peeling, has been observed. Such re-deterioration is considered to be due to deterioration factors such as water that has permeated the repair area. In this paper, we report the result of non-destructive visualization of the moisture behavior of the repair area using a neutron beam tester.

Key words: concrete, cross-section repair, moisture penetration, corrosion of reinforcing bar (rebar corrosion), interface

1. Introduction

To repair a deteriorated concrete structure, cross-section repair is widely used, which repairs deteriorated portions by chipping. Cross-section repair is carried out to restore or improve durability, but may partially cause some re-deterioration, including lifting, peeling, and peeled falling of cross-section repair materials (CRMs) in addition to steel material corrosion. These re-deterioration phenomena are considered to be due to deterioration factors such as water and chloride ions that have permeated portions which have undergone cross-section repair. In particular, water acts as a carrier for carrying harmful substances such as chloride ions, and can also be a physical deterioration factor of frost damage, etc., as well as facilitating reinforcing bar corrosion (rebar corrosion): therefore, it is important to know the behavior of water.

Although there have been many studies on moisture penetration into concrete structures in recent years [1], these addressed single concrete units; there are few studies that have focused on the periphery of the cross-section repair portions. To clarify the effect of the method for treating the interface between the base concrete and the CRM on the moisture behavior in the cross-section repair portion, we conducted a permeability test applying a water pressure of 1 MPa for 48 hours and demonstrated that the hydraulic conductivity decreases by primer treatment or water wetting treatment [2]. We also examined a method of detecting the depth of moisture penetration into concrete by destroying the test piece and spraying a chemical on it [1]. However, it is not yet known how the moisture action in normal pressure (e.g. water splashing) affects the moisture behavior around the cross-section repair portion. Therefore, we examined the moisture behavior in the cross-section repair section using a visualization technique with a neutron beam tester that makes it possible to non-destructively visualize the behavior with the same test piece [3]. This paper describes this process.

Depending on the water content of the base concrete or the chloride ion content, a poor reaction of the primer may occur and the moisture behavior at the interface of the cross-section repair portion may change, which may promote rebar corrosion. Therefore, we examined the following fundamental items: (i) the substrate treatment method at the interface between the concrete and CRM regarding various CRMs, and (ii) the relationship between moisture behavior and rebar corrosion at the interface from mass change and

rebar potential (by conducting a salt spray test on rebar-embedded test pieces with different chloride ion contents in the base concrete).

2. Outline of the test

The following test pieces were made. TP-A was a rebar-embedded test piece with a simulated cross-section repair portion, which was for examining the effect of moisture behavior at the interface on rebar corrosion. TP-B was a test piece in which a part of the cross-section repair portion was cut out, which was for visualizing the moisture behavior at the interface of the cross-section repair portion by neutrons.

2.1 Outline of the TP-A test (rebar-embedded test piece)

2.1.1 Making of TP-A

Figure 1 shows a conceptual diagram of TP-A, which we made. Table 1 lists the materials used. Table 2 summarizes the composition of concrete. Table 3 lists the materials used for the CRMs. The dimensions and shape of each test piece was a cube of side 100 mm, and the rebar was placed at a depth of 30 mm.

To simulate cross-section repair, about 50 mm of base concrete was cast in the lower layer, then the CRM was added (Fig. 2). Then, to clarify the effect of the state of the interface between the CRM and concrete on the rebar corrosion, sodium chloride (NaCl) was mixed at the outer percentage to make it a high-salt state so that the following conditions were met for the base concrete with $\phi 100$ mm embedded round steel: with/without primer construction, water wetting treatment of 2.0 g for every 10,000 mm², and chloride ion 10 kg/m³ (Fig. 3). In addition, a test piece consisting of only concrete and one consisting of only CRM were made for comparison. Three test pieces were used for the salt spray test for each condition, and one test piece was left in the atmosphere.

2.1.2 CRM construction

Each test piece was roughened on the base material surface at a material age of 1 day after the base concrete was cast. After cleaning, the interfacial treatments in Fig. 3 were performed. Then, the

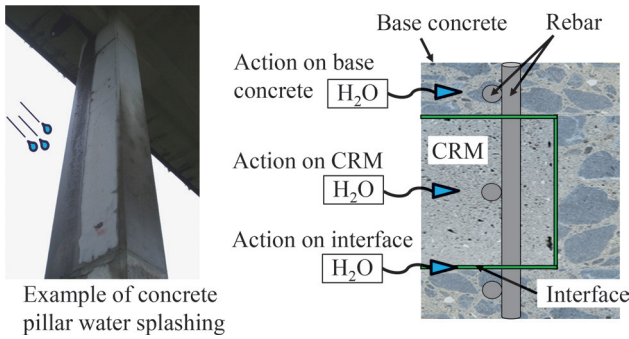


Fig. 1 Test piece conceptual diagram

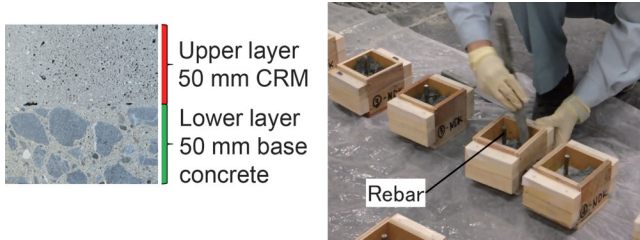


Fig. 2 A scene of making of test pieces

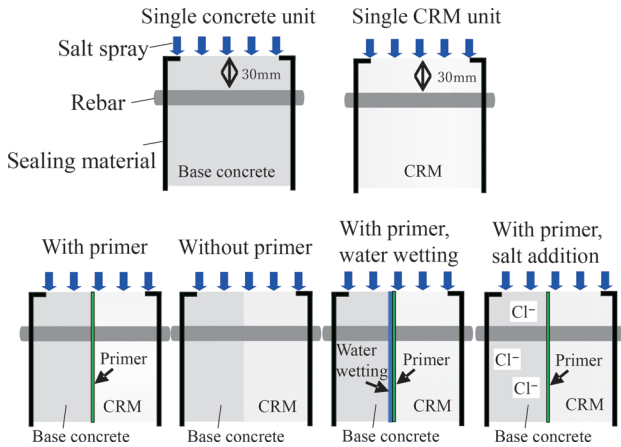


Fig. 3 Test piece making conceptual diagram

Table 1 TP-A and -B concrete materials used

| Material (symbol) | Type (name, quality) |
|----------------------|---|
| Cement (C) | Ordinary portland cement (density 3.16 g/cm ³) |
| Fine aggregate (S) | Land sand (surface dry density 2.58 g/cm ³) |
| Coarse aggregate (G) | Crushed stone (surface dry density 2.66 g/cm ³) |
| Admixture (Ad) | AE water reducing agent |
| Mixing water (W) | Tap water |

Table 2 TP-A and -B concrete composition

| Test piece | W/C | s/a | Chloride ion content | kg/m ³ | | | | Ad |
|------------|-----|-----|----------------------|-------------------|-----|-----|-----|--------|
| | | | | W | C | S | G | |
| (A) | 60 | 48 | 0 | 180 | 300 | 836 | 934 | 0.0045 |
| | | | 10 | | | | | |
| (B) | 60 | 48 | 0 | 180 | 300 | 841 | 938 | 0.004 |

Table 3 Materials used for CRMs for TP-A and -B

| Test piece | Abbreviation | Material type | Mixing ratio | Application amount |
|-------------|--------------|---------------|---|--------------------|
| | | | | g/m ² |
| (A) and (B) | NDK | Primer | Main agent : Hardener = 1 : 1 | 2 |
| | | CRM | Main agent : Admixture : Water = 20 : 3 : 1.5 | - |
| | VF | Primer | Main agent : Water = 3 : 1 | 6 |
| | | CRM | Main agent : Water = 20 : 3.25 | - |
| (A) | AM | Primer | Main agent : Water = 1 : 9 | 1 |
| | | CRM | Main agent : Water = 20 : 3.4 | - |

CRM was constructed and was left at 20°C and 60% RH for 14 days. After demolding, the test surface and the surface on the opposite side were opened, and the remaining four surfaces were covered with a covering material. This state was left in the same environment until the material age of 28 days. For the convenience of making the test piece, the test direction was rotated 90° relative to the driving direction.

2.1.3 TP-A rebar corrosion test by salt spray

The rebar-embedded test piece, the single concrete unit for comparison, and the single CRM unit made above were subjected to the salt spray test, which measured the mass and the rebar potential. The test piece was exposed to a 3% concentration of sprayed salt water at a rate of approx. 0.6 g/cm²/h for one day. Then, it was left in a dry environment for six days. This period of a total of seven days was defined as one cycle. The test piece mass and the rebar potential were measured before the start of spraying and again after 7, 14, and 28 days. The rebar potential was measured by pressing the reference electrode against the 60 mm surface with an uncoated cover placed on the other side of the salt spray, and forming a corrosion circuit to the rebar (Fig. 4). Some test pieces were left at 20°C and 60% RH for comparison.

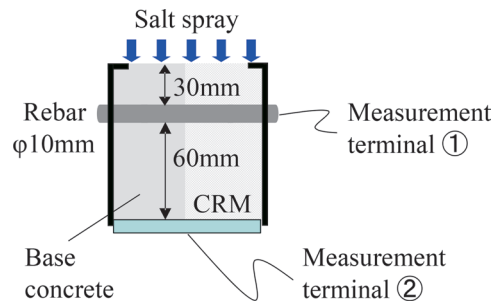


Fig. 4 Conceptual diagram of the salt spray test and potential of rebar measurement

2.2 Outline of the TP-B test

2.2.1 Making, curing, and strength test of TP-B

The specifications of concrete are the same as Section 2.1 and as summarized in Tables 1 to 3. The dimensions of the test pieces were 100 × 100 × 100 mm. After the base concrete was cast up to 5 cm, it was cured at 20°C and 60% RH until the material age of 7 days. Then, the organic (VF) and inorganic (NDK) CRMs in Table 3 were added for the remaining 5 cm. After the material had aged 28

days, the six faces of the cubic test piece were cut to a size of $70 \times 70 \times 25$ mm for the neutron imaging test. Then, the material was left at a constant temperature and humidity (20°C and 60% RH) until the material age of 6 weeks. Then, it was dried at 40°C until the age of 9 weeks, then left at a constant temperature and humidity (20°C and 60% RH) until the age of 11 weeks. In addition, three cylindrical test pieces ($\phi 100 \times 200$ mm) were made for the strength test of a single concrete unit, and the compression strength and static elasticity test were conducted as per JIS A 1108 at an age of 28 days.

2.2.2 TP-B test

To clarify the moisture behavior in the base concrete, CRMs, and near their interface, a one-sided immersion test was conducted that immersed the test piece surfaces with the interface into the water by 5 mm (Fig. 5), followed by the neutron beam imaging test.

This paragraph outlines the neutron beam imaging test. While neutrons have a high penetrating power for calcium and silicon, which are abundant in concrete, they are strongly scattered by hydrogen. Therefore, the obtained transmission image shows a shadow in places that contain moisture originally contained in the test piece or a permeated moisture. The darkness of the shadow changes along with the amount of hydrogen distributed in the permeation direction because the rate of permeability is output as an integrated value in the neutron beam permeation direction. From this principle, the distribution of the rate of permeability corresponds to the distribution of water absorption.

The test piece was taken out of water 24, 48, and 72 hours after the start of the one-sided immersion test, and the water on its surface was wiped off with a waste cloth, etc. before the mass was measured. Then, with the test piece set on the measurement stage, neutron beam imaging was conducted. A neutron beam output from the neutron source was irradiated to it for 3 minutes, and a neutral transmission image (which corresponds to an X-ray photo by neutron beams) was output by a detector consisting of a neutron converter and a CCD camera (a neutron image intensifier is used in this evaluation).

Open source software ImageJ was used for image analysis. For the immersion surface, the side surface for making the test piece was used to reduce the effect of bleeding on the upper surface of the test piece and the effect of consolidation of the lower surface.

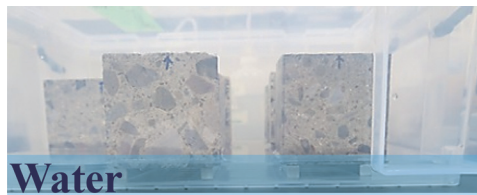


Fig. 5 A scene of the one-sided immersion test

3. Test results and discussion

3.1 Basic characteristics of concrete

Table 4 lists the fresh properties, compression strength, and static modulus of elasticity of concrete.

3.2 TP-A mass change

Figure 6 shows the results of the concrete and the single unit of CRM regarding TP-A mass change. Figure 7 shows the measured

Table 4 Fresh properties, compression strength, and static modulus of elasticity of rebar corrosion test concrete (A) and neutron imaging test concrete (B)

| Test piece | NaCl addition | Slump | Air content | Compression strength | Static modulus of elasticity |
|------------|---------------|-------|-------------|----------------------|------------------------------|
| | | cm | % | N/mm ² | kN/mm ² |
| (A) | Without | 14.0 | 4.0 | 26.5 | 24.1 |
| | With | 18.5 | 4.2 | 30.4 | 24.5 |
| (B) | Without | 18.5 | 3.8 | 32.7 | 29.0 |

mass of the test pieces simulating cross-section repair. For all the specimens, the mass increased in one cycle and the subsequent mass change was small. Figure 6 shows that the mass increase of the concrete and the single CRM unit with NaCl added were smaller than that of the single concrete unit and in particular, the mass change of every type of CRM was as small as approx. 1/8 that of the concrete. In addition, Figure 7 shows no clear differences resulting from the “with/without primer construction” condition regarding any of the CRMs. This can be because the interfacial area was very small com-

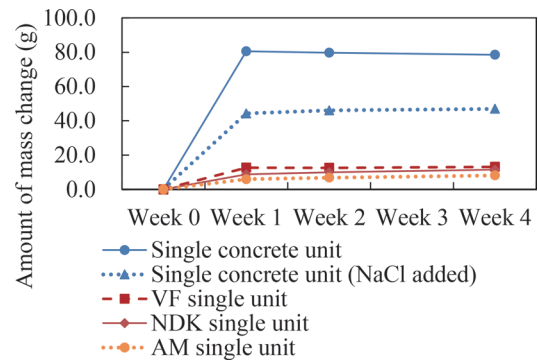


Fig. 6 Mass changes of single concrete unit and single CRM unit

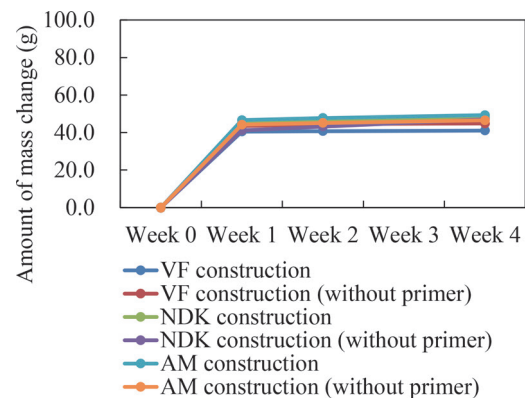


Fig. 7 Mass changes resulting from “with/without primer on the test piece with CRM constructed on the concrete”

pared to the surface of moisture action on the base concrete and the CRM, and the mass change was greatly affected by the amount of water that has permeated from the entire surface of the single concrete unit or the single CRM unit.

3.3 TP-A Potential of rebar

Table 5 summarizes the potential and rebar corrosion likelihood according to the Japan Society of Civil Engineers criteria [4]. This study used a silver-silver chloride electrode (SSE) as the reference electrode. Therefore, the values of the copper-copper sulfate electrode (CSE) in Table 5 were corrected according to Equation (1) [5]. If the potential was nobler than -90 mV vs SSE, it was considered to be not corroded with a probability of 90% or more; if it was more base than -240 mV vs SSE, it was considered to be corroded with a probability of 90% or more.

Table 5 Relationship between potential and rebar corrosion characteristics

| Potential (E) | Possibility of rebar corrosion |
|----------------------|-------------------------------------|
| $-200 < E$ | Not corroded \geq probability 90% |
| $-350 < E \leq -200$ | Undeterminable |
| $E \leq -350$ | Corroded \geq probability 90% |

$$E_{t,LCSE}^{Fc} = E_{t,SSE}^{Fc} - 120.1 - 2.00 \cdot (t - 25) \quad (1)$$

where

$E_{t,LCSE}^{Fc}$ (mV): Potential measurement of rebar for saturated copper sulfate electrode at temperature t ($^{\circ}$ C) and

$E_{t,SSE}^{Fc}$ (mV): Potential measurement of rebar for saturated silver-silver chloride electrode at temperature t ($^{\circ}$ C).

Figures 8 to 12 show the measurement results of the rebar potential. Figure 8 shows for the test pieces left at 20° C and 60% RH without being subjected to the salt spray test, the change in potential was small and constant regardless of the “with/without NaCl addition” condition or the CRM type. Figure 9 shows that the potential of the single concrete unit was base in the one-cycle test and the change in the potential was small thereafter. On the other hand, the concrete with NaCl added exhibited a base value even before being subjected to the salt spray test, and the value did not change significantly even after the start of the test, with the effect of salt spray being small. Also for the single CRM unit, the salt spray caused the potential value to be a base in 14 days up to the same level as the single concrete unit.

Figures 10 to 12 show that the potential of the rebar in the test pieces simulating the cross-section repair was almost the same as that of the single concrete unit in each test piece subjected to normal construction, which means adding the CRM after constructing the primer on the base concrete. By contrast, when the CRM was added without primer construction, the value varied widely. However, it was more base than in the normal construction and showed a value indicating a zone deemed to be corroded with a probability of 90% or more. For the test piece subjected to normal construction after water wetting treatment of the base concrete interface, like normal construction with primer construction, it showed that the value tended to be on the noble side compared to the case where the primer was not yet constructed. For the test piece cross-sectionally repaired to the base concrete containing NaCl, like the result of potential in a

single concrete unit containing NaCl, the base value appeared before the salt spray, and it did not exhibit a clear effect of the difference in the chloride ion content at the interface on rebar corrosion.

The above suggests that, by performing primer treatment or primer and water wetting treatment at the interface between the base

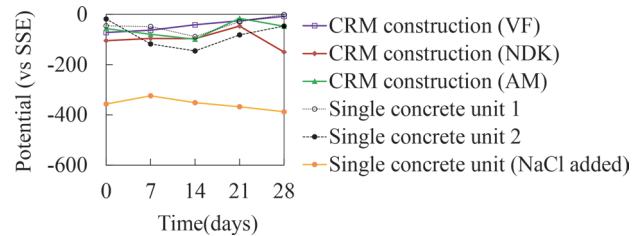


Fig. 8 Potential of the test pieces left in the atmosphere

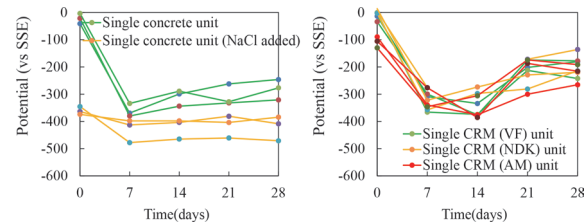


Fig. 9 Potential of single concrete unit and single CRM unit (salt spray test)

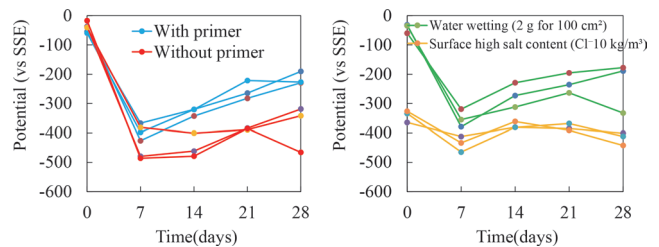


Fig. 10 Potential of the test pieces using CRM (VF) (salt spray test)

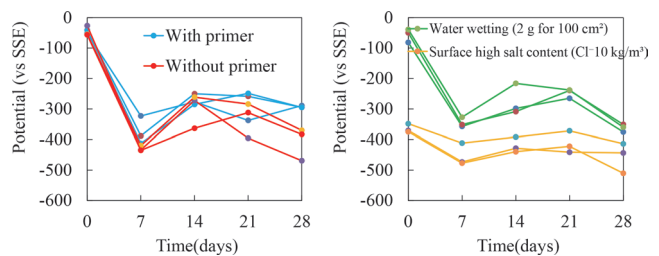


Fig. 11 Potential of the test pieces using CRM (NDK) (salt spray test)

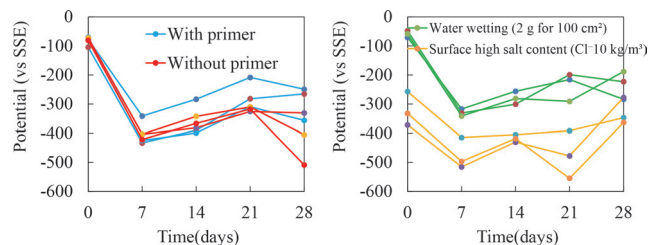


Fig. 12 Potential of the test pieces using CRM (AM) (salt spray test)

concrete and CRM, the water transfer at the interface can be suppressed and the progress of rebar corrosion can be suppressed in the cross-section repair portion.

3.4 Mass change of TP-B for neutron beam imaging test during one-sided immersion

Figure 13 shows the measurement results of the TP-B mass changes for one-sided immersion. The mass change rate of the single CRM unit was smaller than that of the single concrete unit. No clear difference was seen between “with/without primer construction” like the results in Section 3.2.

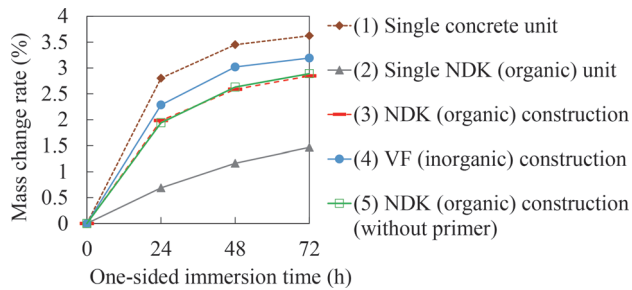


Fig. 13 TP-B mass change rate

3.5 TP-B neutron beam imaging

Figure 14 contains the images showing the differences between before and after the one-sided immersion, where the portions containing water permeated are represented by shading. A comparison of the single concrete unit (1) and single NDK (organic CRM) unit (2), shows that, for the single concrete unit, the water gradually permeated with the passage of the immersion time, and after 72 hours, permeated the whole, whereas moisture penetration in the single NDK unit was more suppressed than that in the single concrete unit.

These results match those of the mass changes from moisture penetration in Fig. 13. Considering the moisture penetration into

cross-section repair portions, polymer cement mortar, widely used as a CRM, contains organic materials such as polymers as its constituent materials; therefore, it has a larger hydrogen content in the base metal itself than that of concrete. In this test, for example, as a polymer component, the mortar contains acrylic resin, which is said to have a hydrogen density equivalent to that of water.

For this reason, since the CRM has more hydrogen content than that of the concrete, we expected that the difference in moisture penetration could not be clearly captured. However, from the results of mass change and neutron beam imaging in this test, we found that even a CRM containing a large polymer content can be neutron imaged by obtaining the difference before and after immersion. From the results of NDK (organic CRM) construction (3) and VF (inorganic CRM) construction (4), which simulated cross-section repair, moisture penetrates into concrete but has difficulty penetrating the CRM; both exhibited this tendency. Moisture penetration into inorganic CRM was larger than that of organic CRM, but it was smaller than that of a single concrete unit. Water diffusion from the interface was not found in both organic and inorganic ones. In addition, unlike the results inferred from the rebar corrosion data, the comparison between (3) and (5) in Fig. 14 showed that there was no significant difference in the moisture penetration status near the interface depending on the “with/without primer construction” condition. One of the possible reasons for this is that the CRM construction on the base concrete was vertically downward and the construction conditions were relatively good. The other is that, because the concrete side of the base material was at an early age and contained a large amount of water, the interface was densely filled without drying out at the interface. As for the test pieces in (5), the base concrete entered the CRM side in the shallow part, and the black discolored part was only on the base material side.

As detailed above, we attempted to visualize the behavior of moisture in cross-section repair portions over time with neutron beam imaging. As a result, we found that the moisture penetration rate differs greatly between concrete and CRM, it differs depending also on the CRM type, and if the CRM construction conditions for the base concrete are relatively good, no significant moisture penetration occurs near the interface.

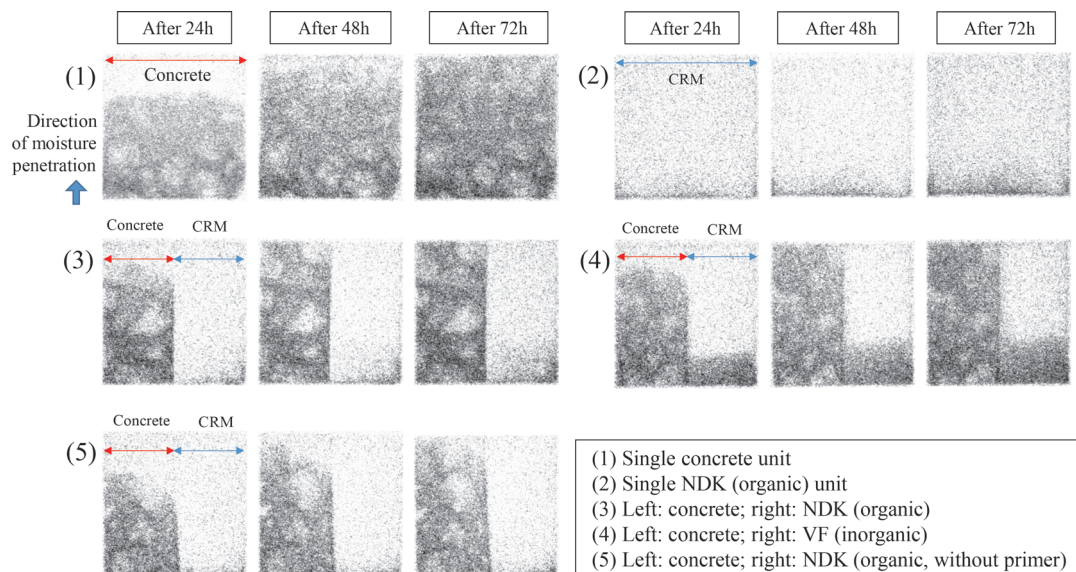


Fig. 14 Results of observation by neutron beam imaging

4. Conclusion

The findings from this study are summarized below.

- (1) The amount of mass change associated with moisture penetration was as small as approximately 1/8 of the single concrete unit in CRM, and the moisture penetration test by neutron beam imaging showed that the spread of moisture to CRM was small, which revealed that CRM has a high mass transfer resistance to water.
- (2) It was suggested that, by treating the interface between the base concrete and the CRM with primer or water wetting, (i) the effect of the construction situation would be reduced, (ii) the movement of water at the interface would be suppressed, and (iii) as a result, the progress of rebar corrosion in the cross-section repair portion could be suppressed.
- (3) We attempted to visualize the behavior of moisture at cross-section repair portions over time by neutron beam imaging. As a result, we found that the moisture penetration rate differs greatly between concrete and CRM, it differs depending also on the CRM type, and if the CRM construction conditions for the base concrete are relatively good, no significant moisture penetration occurs near the interface.

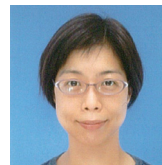
References

- [1] H. Suzuki, H. Ueda, "The effect of concrete quality on the time dependence of moisture penetration depth," *Proceedings of the Japan Concrete Institute*, Vol. 36, No. 1, pp. 676-681, 2014 (in Japanese).
- [2] H. Suzuki, H. Ueda et al., "Base treatment of concrete at the time of repair," *67th Annual Academic Lecture*, V-157, pp. 313-314, 2013 (in Japanese).
- [3] Y. Yoshimura, M. Mizuta et al., "Evaluation of Water Flux of Concrete by Neutron Imaging," *Proceedings of the Concrete Structure Scenarios, JSMS*, Vol. 19, pp. 379-384, 2019 (in Japanese).
- [4] Second Term Corrosion Protection Subcommittee of JSCE Concrete Committee, "Test method for half-cell potential of uncoated rebars in concrete structures (JSCE-E601-2000)," *Concrete engineering series*, Vol. 30, pp. 248-256, December 2000 (in Japanese).
- [5] Y. Shinoda, N. Mochizuki, "Base treatment of concrete at the time of repair," *66th Annual Academic Lecture*, IV-224, pp. 447-448, 2011 (in Japanese).

Authors



Hiroaki SUZUKI
Assistant Senior Researcher, Concrete
Materials Laboratory, Materials Technology
Division Research Areas: Concrete Materials



Maki MIZUTA, Dr. Eng
Research Scientist, Neutron Beam
Technology Team, RIKEN Center for
Advanced Photonics Research Areas:
Concrete Engineering



Motoki UEHARA, Dr. Eng
Senior Chief Researcher, Head of Concrete
Materials Laboratory, Materials Technology
Division Research Areas: Material Science
Development of New Materials



Yoshie OTAKE, Dr. Sc
Group Leader, Neutron Beam Technology
Team, RIKEN Center for Advanced
Photonics Research Areas: Compact Neutron
System Development

Effects of Rotational Conditions on Performance of Gear Unit Pinion Bearing

Ken TAKAHASHI

Daisuke SUZUKI

Takafumi NAGATOMO

Lubricating Materials Laboratory, Materials Technology Division

Tapered roller bearings are mainly used in rotating parts of gear units on railway vehicles. In order to prevent bearing seizure and to improve gear unit reliability, it is important to ensure appropriate clearance between bearings. Bearing clearance changes from its initial value as vehicles travel due to atmospheric temperatures and variation in the initial values in the gear unit assembly, which affects bearing performance. In this research, an actual gear unit was subjected to bench rotation tests under various bearing clearances and various atmospheric temperatures. Bearing temperature and torque were measured, and changes in bearing clearance were estimated.

Key words: gear unit, pinion, machine element, tapered roller bearing, bearing clearance

1. Introduction

In Japan, most gear units for power transmission in railway vehicles (electric cars) employ one-stage speed reducers, and use tapered roller bearings for the rotating parts [1]. Two tapered roller bearings are installed on the pinion shaft, which are referred to as pinion bearings, to support the pinion shaft against the gear case. Similarly, two tapered roller bearings are installed in the axle, which are referred to as gear bearings, to support the gear case. These bearings are lubricated with gear oil spread by the gear. Among these bearings, the rotational speed of the pinion bearings is higher than that of the gear bearings, so the sliding speed at the contact surface between roller ends and inner ring flanges of the pinion bearings is higher than that of the gear bearings. In the pinion bearings, therefore, seizure may occur by metal-to-metal contact from inadequate lubrication between roller ends and inner ring flanges [2]. In order to prevent pinion bearing seizures, it is important to appropriately manage bearing clearances. Although this bearing clearance is usually adjusted in a specified range when assembling gear units, this initial clearance value can change due to temperature changes in peripheral parts of the bearings as vehicles travel [3, 4].

The authors of this paper have already reported the behavior of bearing temperatures and torque under various rotational conditions, lubricating conditions, and bearing clearances by performing basic rotational tests of pinion bearings [5]. On the other hand, the previous research was conducted under circulating lubrication with gear oil, therefore there are many unverified items about the performance and the behavior of pinion bearings mounted on an actual gear unit which are lubricated with gear oil spread by the gear. Therefore, in this study, the effects of initial bearing clearance and atmospheric temperature on the bearing temperature and torque were investigated in bench rotation tests on an actual gear unit. In addition, the behavior of bearing clearance during the rotation of gears was estimated from the temperature changes on peripheral parts of bearings [6].

2. Test apparatus

2.1 Test rig of gear unit

Figure 1 shows the test rig of a gear unit used in this study. This rotation testing machine has the structure in which a pinion shaft is rotated by a motor through a coupling, using an actual gear unit as a

specimen. The gear unit is attached to an axle and supported by two bearings at both ends of the axle and a torque reaction rod. Blowers are installed in the vicinity of the gear unit and the support bearings to cool them.

The specifications of the gear unit are shown in Table 1, and a schematic view of the gear unit is shown in Fig. 2. The reduction gear mechanism was composed of helical gears with a left-hand

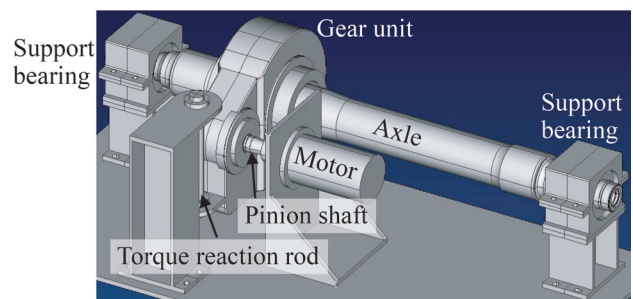


Fig. 1 Test rig of gear unit

Table 1 Specification of testing gear unit

| | |
|--|--------------------------|
| Material of gear case | Aluminum alloy |
| Material of housings | Carbon steel |
| Material of pinion and pinion shaft | Alloy steel |
| Dimensions of pinion bearings | (Tapered roller bearing) |
| Outside: $\phi 150$ mm \times Bore: $\phi 70$ mm \times Width: 38 mm | |

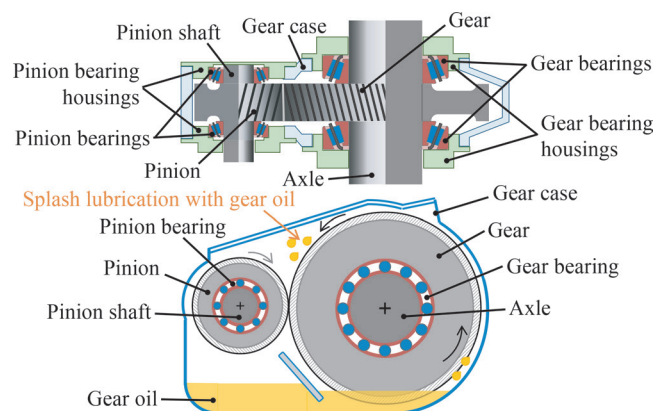


Fig. 2 Schematic view of testing gear unit

pinion and a right-hand gear. The pinion shaft was installed with pinion bearings on both sides of the pinion, which supported the pinion shaft against the gear case. The axle was installed with gear bearings on both sides of the gear, which supported the gear case against the axle. The inner rings of the pinion bearings were fitted to the pinion shaft, and the inner rings of the gear bearings were fitted to the axle. On the other hand, the outer rings of these bearings were fitted to the housings which were fastened to the gear case. The gear case was made of aluminum alloy, and gear oil was stored inside.

2.2 Measuring items

While the gear unit is operating, the temperatures, and the rotational speed and the torque of the pinion shaft can be measured (Fig. 3). The temperatures were measured at the outer diameter surfaces of the pinion bearings and the gear bearings, the surface of the gear case, the gear oil, and the atmosphere. These were all measured with thermocouples. The rotational speed of the pinion shaft was measured with a photoelectric rotation detector. The torque of the pinion shaft was obtained by calculation using the current value of the motor. Furthermore, the temperature at the end of the pinion shaft was measured with a small temperature data logger (Fig. 4).

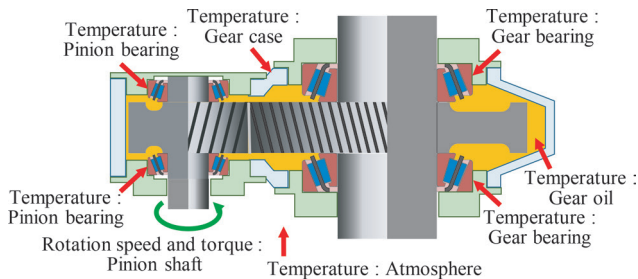


Fig. 3 Measuring items

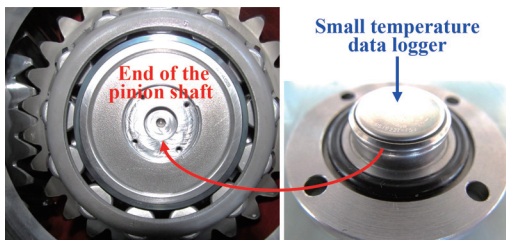


Fig. 4 Measurement of end of pinion shaft

2.3 Test bearing

In this study, we focused on the pinion bearing (hereinafter referred to as “bearing”). The outer ring, inner ring, and rollers were made of high-carbon chromium bearing steel. The cage was made of low-carbon steel. The bearing clearance (combination clearance in the axial direction of the two bearings) could be changed by inserting shims of various thicknesses between the gear case and the pinion housing (Fig. 5).

3. Test method

The rotation tests were performed under the constant conditions shown in Table 2. Figure 6 shows the rotational pattern of the pinion shaft. Maximum rotational speed of the pinion shaft is 6,000

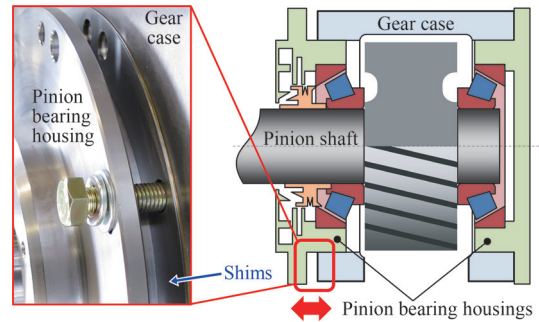


Fig. 5 Method of changing the bearing clearance

Table 2 Fixed test conditions

| Direction of pinion rotation | | Clockwise (In a view from the motor side) |
|------------------------------|---------------------|--|
| Lubricants | Oil type | Gear oil (Base oil: Mineral oil) |
| | Kinematic viscosity | 9.9 mm ² /s (100°C) |
| | Viscosity index | 78.7 mm ² /s (40°C) |
| Oil quantity | | 2.95 L |
| Air - cooling | | 10 m/s |

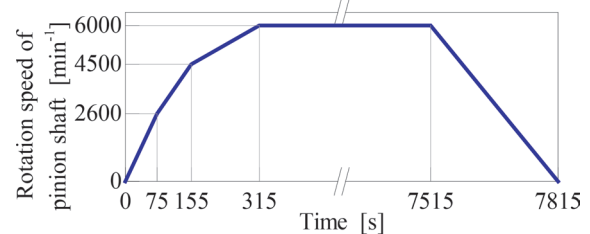


Fig. 6 Rotational pattern

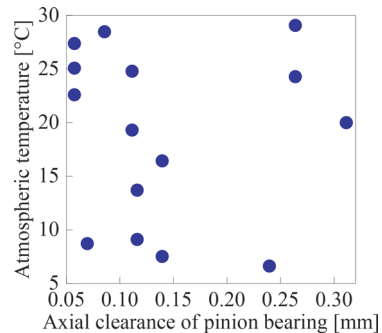


Fig. 7 Test conditions

min⁻¹. This rotational speed corresponds to a vehicle speed of approximately 320 km/h. The gear case and the support bearings were air-cooled when the rotational speed of the pinion shaft was 200 min⁻¹ or higher.

Under the constant conditions shown in Table 2, the axial clearance of the pinion bearings and atmospheric temperature were variously changed. They are shown in Fig. 7. Since the gear case and the pinion shaft were made of different materials shown in Table 1, the bearing clearance varied depending on the temperature of the gear unit. In this paper, the bearing clearances are shown as values by converting the measured values at assembling to the values at 20°C.

4. Temperature change of each part of the gear unit and torque of pinion shaft

4.1 Influence of the bearing clearance

Figure 8 shows the temperature change of each part of the gear unit and torque of the pinion shaft from the start of rotation to 3,600 s for the tests with different bearing clearances under conditions where the atmospheric temperature was close to 20°C. Regardless of the test conditions, the temperature measured at the end of the pinion shaft was the highest among the temperatures of each part,

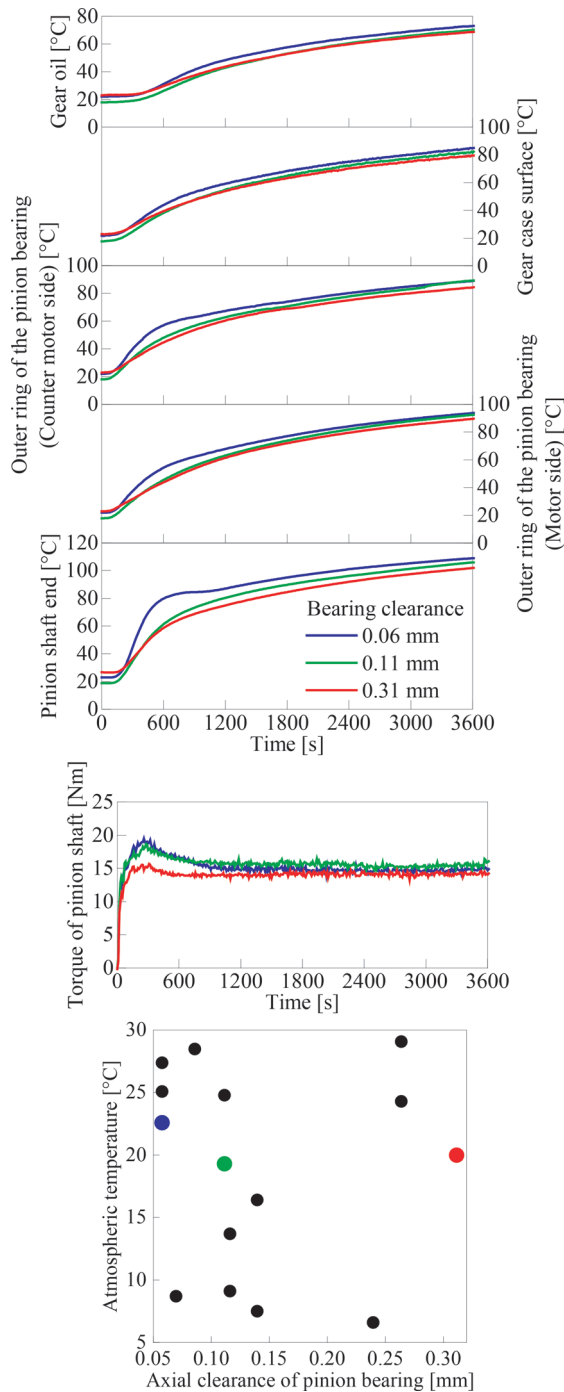


Fig. 8 Effect of bearing clearance for condition of gear unit

and increased rapidly from the start of rotation to approximately 600 s as the bearing clearance was smaller. In particular, when the bearing clearance was 0.06 mm, it reached about 80°C in 600 s after the start of rotation, and after a pause in the temperature increase, it rose slowly again. This is thought to be due to an increase in frictional resistance and rolling viscous resistance inside the bearing. The increase in these resistances resulted from the widening of a load contact zone and an increase in the number of loaded rollers due to a relatively small clearance. Although it is not as apparent as the trend of temperature at the end of the pinion shaft described above, the temperature rise in the outer ring of the bearing immediately after the start of rotation was more rapid on both the motor side and the counter motor side bearings as the bearing clearance was reduced. The tendency described above weakened further at the temperature of the gear case surface and gear oil. These trends may be attributed to the main heat source in the tests being the pinion bearings, and the temperature rise of the inner rings being the greatest [7, 8]. The torque of the pinion shaft reached its maximum value immediately after the start of rotation, then decreased, and became almost constant after about 1,000 s. The maximum value of the torque of the pinion shaft increased as the bearing clearance decreased. Although the torque of the pinion shaft included other torques than the torque of the pinion bearings (for example, the torque of the gear bearings and the stirring resistance of gear oil), it was confirmed that the torque of the shaft increased as the bearing clearance decreased in the rotation test performed by the authors with only the pinion bearings [5]. For this reason, it is considered that the bearing clearance has the most influence on the above torque difference.

4.2 Influence of the atmospheric temperature

Figure 9 shows the temperature change of each part of the gear unit and torque of the pinion shaft from the start of rotation to 3,600 s for the tests with different atmospheric temperatures under conditions where the bearing clearance was close to 0.11 mm. Regardless of the conditions, the temperature measured at the end of the pinion shaft was the highest among the temperatures of each part, and increased rapidly from the start of rotation to about 600 s as the atmospheric temperature was lower. In particular, when the atmospheric temperature was 9.1°C, it reached about 80°C in 600 s after the start of rotation, and after the rising stopped a while, it rose slowly again. This is thought to be due to an increase in rolling viscous resistance and stirring resistance of gear oil inside the bearing, caused by relatively low atmospheric temperature. In the rotation test performed by the authors with only the pinion bearings, it has been confirmed that the heating amount from the bearings increases when the gear oil temperature drops and its viscosity rises, which explains the trend of the temperature rise above [5]. The trends of temperature changes of the outer rings of bearings, gear case, and gear oil were the same as those described in Section 4.1. The torque of the pinion shaft reached its maximum value immediately after the start of rotation, then decreased, and remained almost constant after about 1,000 s. The maximum value of the torque of the pinion shaft increased as the atmospheric temperature decreased. This is because the viscosity of gear oil increased as the atmospheric temperature decreased, and the rolling viscous resistance inside the bearing and the stirring resistance of gear oil increased.

4.3 Temperature at the end of the pinion shaft and torque of the pinion shaft

As described in Section 4.1 and Section 4.2, the difference in

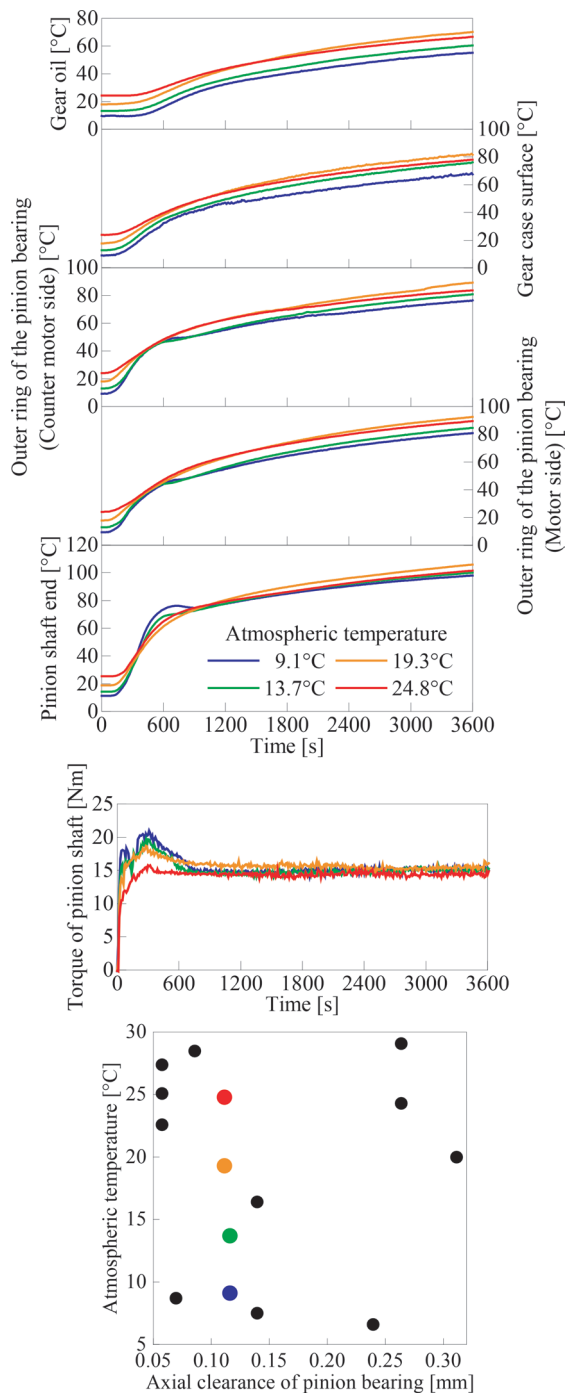


Fig. 9 Effect of atmospheric temperature for condition of gear unit

the test conditions most clearly affects the temperature at the end of the pinion shaft. In particular, it was found that the temperature rise from the start of rotation to about 600 s varies greatly depending on the test condition. Therefore, from the results of each test condition shown in Fig. 7, the maximum rate of increase in the temperature at the end of the pinion shaft (temperature rise per 10 s) is summarized in a contour diagram with respect to the initial bearing clearance EP_{20} (Axial clearance of pinion bearings shown in Fig. 7) and atmospheric temperature, and shown in Fig. 10. The white area in the diagram is the area for which data was not obtained because the rotation test was not performed. The maximum rate of increase in the

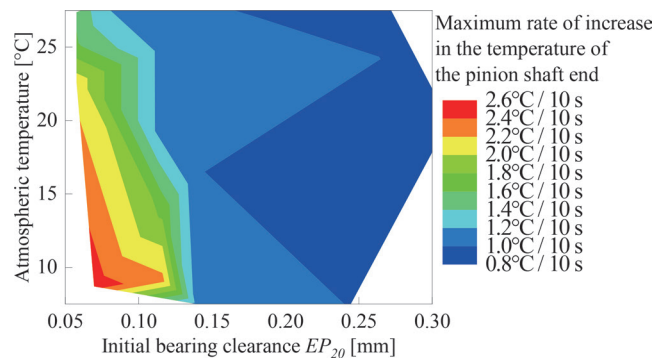


Fig. 10 Maximum rate of increase in temperature at end of pinion shaft

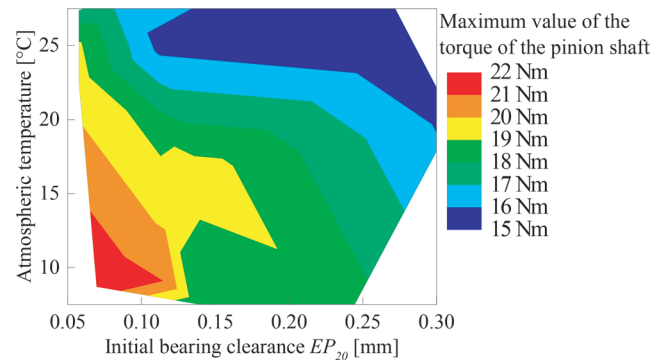


Fig. 11 Maximum value of torque of pinion shaft

temperature at the end of the pinion shaft tends to increase as EP_{20} decreases and the atmospheric temperature decreases. In particular, when EP_{20} is smaller than 0.14 mm, the maximum rate of increase in the temperature at the end of the pinion shaft increases rapidly as EP_{20} decreases.

It was found that the difference in the test conditions also affects the torque of the pinion shaft. Therefore, from the results of each test condition shown in Fig. 7, the maximum value of the torque of the pinion shaft is summarized in a contour diagram with respect to the initial bearing clearance EP_{20} and atmospheric temperature, and shown in Fig. 11. The maximum value of the torque of the pinion shaft tends to increase as EP_{20} decreases and the atmospheric temperature decreases.

5. Study on change of bearing clearance due to temperature change

As shown in Section 4, the temperature of each part of the gear unit greatly changes immediately after the start of rotation. For this reason, the bearing clearance changes due to the thermal expansion of each part of the gear unit. There is a concern that a seizure of the bearing may occur when the bearing clearance decreases to 0 mm. Therefore, the change in the bearing clearance is estimated from the temperature change in each part of the gear unit.

5.1 Method for calculating bearing clearance

By simplifying the structure around the pinion bearings of the gear unit shown in Fig. 2 (Fig. 12), we calculated the bearing clearance EP during the operation of the gear unit, using (1) that takes

into account only the axial thermal expansion of each component.

$$EP = EP_{20} + (t_c - 20) \cdot \alpha_c \cdot L_c - (t_h - 20) \cdot \alpha_h \cdot (L_c - L_b) - (t_s - 20) \cdot \alpha_s \cdot L_b \quad (1)$$

where EP_{20} is the initial bearing clearance shown in Fig. 7. t_c , t_h , and t_s are the temperatures of the gear case surface, the pinion bearing housing, and the pinion shaft. α_c , α_h , and α_s are the coefficients of thermal expansion of the gear case, the pinion bearing housing, and the pinion shaft. L_c is the distance between the housing fastening surfaces of the gear case, and L_b is the distance between the bearing centers. Since the temperatures of the pinion bearing housings are not directly measured, the temperature of the outer ring of the bearing near the housing (average value of the temperatures of the two bearings) is used, and the temperature of the pinion shaft is used for the temperature of the shaft end.

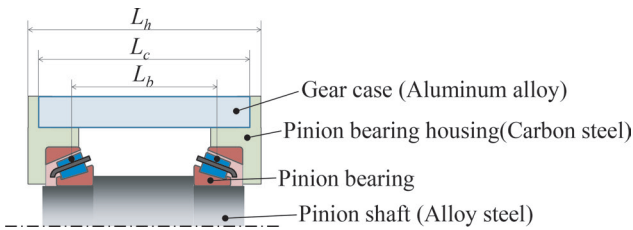


Fig. 12 Structure around pinion bearings

5.2 Calculation result of bearing clearance

Figures 13 and 14 show the bearing clearances calculated by (1) for the test results shown in Figs. 8 and 9. After about 600 s from the start of rotation, where the temperature rises in each part of the gear unit, the bearing clearance increases mainly due to the difference in the coefficient of thermal expansion between the gear case and the pinion shaft. However, for about 600 s from the start of rotation, the bearing clearance decreases with rotation, and this tendency is more pronounced as the initial bearing clearance is smaller (Fig. 13) and the atmospheric temperature is lower (Fig. 14). This is because, in the initial stage of rotation, the temperature of the pinion

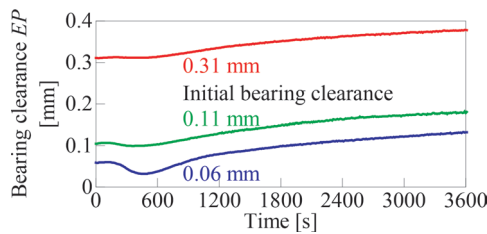


Fig. 13 Effect of initial bearing clearance on bearing clearance in rotation of pinion shaft

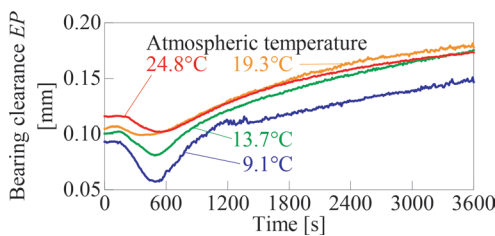


Fig. 14 Effect of atmospheric temperature on bearing clearance in rotation of pinion shaft

shaft t_s accompanying the rotation of the bearing rises faster than the temperature of the gear case t_c , and the thermal expansion of the pinion shaft becomes larger than the thermal expansion of the gear case. The trend whereby the bearing clearance first decreases after the start of rotation then increases agrees with the trend confirmed by the rotation test performed by the authors with only the pinion bearings [5]. As described in Section 4, when the initial bearing clearance was the smallest and the atmospheric temperature was the lowest, the temperature at the end of the pinion shaft increased rapidly in the initial stage after the start of rotation, and after the rising stopped a while, it rose slowly again. It is thought that this is because the bearing clearance (EP value) started to increase and the heat generation was suppressed after the heat generation of the bearing increased due to the decrease in the bearing clearance.

As shown in Figs. 13 and 14, the bearing clearance varies during the rotation of the pinion shaft. There is a concern that when the bearing clearance decreases the most the temperature of the bearing rises rapidly which may result in seizure of the bearing. Therefore, from the results of each test condition shown in Fig. 7, the minimum values of the actual bearing clearances EP_{min} obtained by (1) are summarized in a contour diagram with respect to the initial bearing clearance EP_{20} and atmospheric temperature, and shown in Fig. 15. Figure 16 shows the value obtained by subtracting EP_{min} from the initial bearing clearance EP_{20} , that is, the maximum decrease in bearing clearance during rotation.

When compared at the same atmospheric temperature, the smaller EP_{20} becomes, the smaller EP_{min} is. Further, when compared with the same EP_{20} , the lower the atmospheric temperature is, the smaller the EP_{min} is. In addition, the maximum decrease in bearing clearance tends to increase as EP_{20} decreases and the atmospheric

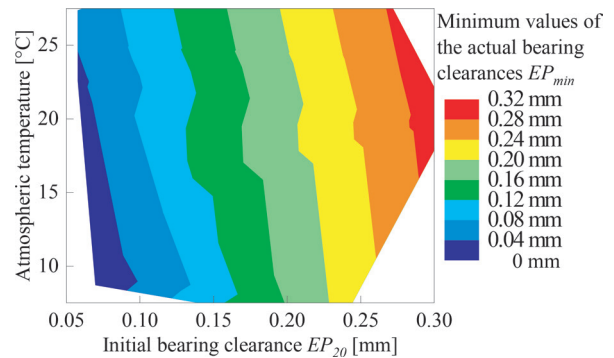


Fig. 15 Minimum values of actual bearing clearances during operation of gear unit

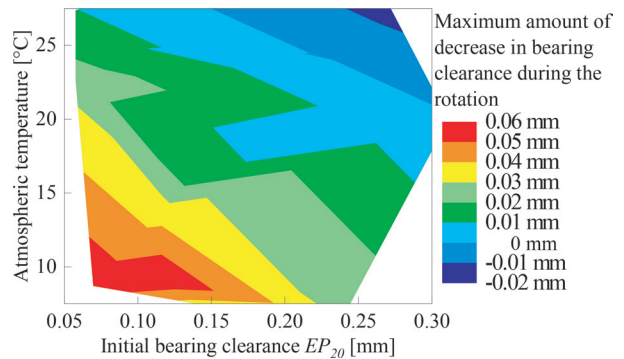


Fig. 16 Maximum amount of decrease in bearing clearance during operation of gear unit

temperature falls. In the range in which the test was performed, the maximum decrease in bearing clearance was a relatively large 0.05 mm or more under the conditions where EP_{20} was 0.10 mm or less and the atmospheric temperature was 10°C or less.

6. Conclusions

The findings obtained through this study are summarized below.

- (1) The temperature measured at the end of the pinion shaft is the highest among the temperatures of each part, and increases more rapidly from the start of rotation to about 600 s as the initial bearing clearance is smaller and the atmospheric temperature is lower. Therefore, the maximum rate of increase in the temperature at the end of the pinion shaft (temperature rise per 10 s) also increases as the initial bearing clearance is smaller and the atmospheric temperature is lower.
- (2) The maximum value of the torque of the pinion shaft tends to increase as the initial bearing clearance is smaller and the atmospheric temperature is lower.
- (3) The bearing clearance during the operation of the gear unit is calculated using the temperature change of each part. As a result, it was found that the bearing clearance decreases with rotation for about 600 s from the start of rotation, and this tendency is more pronounced as the initial bearing clearance is smaller and the atmospheric temperature is lower.
- (4) The minimum value of the bearing clearance during the operation of the gear unit decreases as the initial bearing clearance is smaller and the atmospheric temperature is lower.

Authors



Ken TAKAHASHI, Dr. Eng.
Senior Researcher, Lubricating Materials Laboratory, Materials Technology Division
Research Areas: Tribology, Roller Bearing, Mechanical Engineering



Daisuke SUZUKI
Assistant Senior Researcher, Lubricating Materials Laboratory, Materials Technology Division
Research Areas: Tribology, Roller Bearing, Mechanical Engineering

References

- [1] Ezaki, Y., Terasawa, H. and Wada, T., "Vibration Analysis for Tapered Roller Bearing Fatigue Prevention," *Journal of System Design and Dynamics*, Vol. 6, No. 5, pp. 665-675, 2012.
- [2] SKF, *Bearing damage and failure analysis*, p. 70, 2017.
- [3] Johns, T.M., "Application Guide for Tapered Roller Bearings in Aluminum Differential Housings," *SAE Transactions, Journal of Passenger Cars*, Vol. 107, Section 6, pp. 1610-1624, 1998.
- [4] Hayashi, Y., Zenbutsu, M. and Suzuki, H., "Analysis of Fluctuations in Bearing Preload and Optimal Design of Tapered Roller Bearings for Pinion Shaft Support in Differential Gearboxes," *SAE Transactions, Journal of Passenger Cars: Mechanical Systems*, Vol. 110, Section 6, pp. 1042-1049, 2001.
- [5] Takahashi, K., Suzuki, D. and Nagatomo, T., "Investigation of factors affecting the performance of pinion bearing for gear unit of railway vehicle," *Transactions of the JSME*, Vol. 85, No. 876, p. 19-00181, 2019 (in Japanese).
- [6] Takahashi, K., Suzuki, D. and Nagatomo, T., "Effects of bearing clearance and atmospheric temperature on performance of pinion bearings of railway vehicles," *Journal of Advanced Mechanical Design, Systems, and Manufacturing*, Vol. 14, No. 4, p. 20-00048, 2020.
- [7] Otaki, Y. and Haruyama, T., "Study on non-contact temperature measurement by temperature sensitive paint for roller end face of tapered roller bearing," *Proceedings of Tribology Conference 2018 Spring Tokyo*, pp. 108-109, 2018 (in Japanese).
- [8] Xianwen, Z., Hao, Z., Xu, H., Xin, L. and Qingkai, H., "Investigation on thermal behavior and temperature distribution of bearing inner and outer rings," *Tribology International*, Vol. 130, pp. 289-298, 2019.



Takafumi NAGATOMO, Dr. Eng.
Senior Chief Researcher, Head of Lubricating Materials Laboratory, Materials Technology Division
Research Areas: Tribology, Roller Bearing, Metallic Material

Summaries of Papers in RTRI REPORT (in Japanese)

Recent Trends of Design Technology of Railway Tunnel and Summary of Revision of Design Standards for Railway Tunnels

Kazuhide YASHIRO

(Vol.36, No.5, 1-7, 2022.5)

More than 20 years have passed since the three design standards for railway tunnels were published. In the meantime, design methods for structures other than tunnels have shifted to performance-verification design methods. Since 2014, a committee consisting of academic experts, railway operators has been set up to study the introduction of performance-based design, and as a result, in April 2022, the Ministry of Land, Infrastructure, Transport and Tourism issued the design standards for railway structures as a notification. This outlook commentary introduces trends in tunnel design technology for railways and an overview of new railway tunnel design standards based on performance-verification design methods.

Calculation Method of Design Earth Pressure of Shield Tunnel in Clayey Ground

Kiwamu TSUNO, Kiichi FUJITA, Koji FUNAKOSHI

(Vol.36, No.5, 9-14, 2022.5)

This paper describes a method of calculating earth pressure in the beam-spring model which was introduced in the design standard for railway shield tunnels in 1997. A parameter study was carried out to grasp the influence of the coefficient of lateral earth pressure on verification results and it was revealed that the coefficient of lateral earth pressure has a significant influence and is one of reasons for irrational design in case of medium cohesive clay. The authors of this paper modified the coefficient of lateral earth pressure and showed the relationship between vertical earth pressure and verification results using modified values.

Seismic Design Method for Shield Tunnels in the Condition of Change in Ground Conditions in the Longitudinal Direction

Kiichi FUJITA, Koji FUNAKOSHI, Kiwamu TSUNO

(Vol.36, No.5, 15-20, 2022.5)

The authors investigated influence of seismic motion on shield tunnels that are located in areas with varying ground conditions. This research revealed that the bigger inclination angle of boundary between basic layer and soft layer becomes, the bigger sectional force such as axial force, bending moment and shear stress becomes. In addition, the sectional force obtained by the equivalent stiffness beam model was found to be larger than that obtained by the beam-spring model. This research also confirmed that the results by the beam-spring model when the inclination angle is 5.9 degree is satisfied with the verification.

Proposal of Pre-verified Specification for Mountain Tunnel Lining and Invert

Keisuke SHIMAMOTO, Takeshi KAWAGOE, Kazuhide YASHIRO, Hikaru UENO

(Vol.36, No.5, 21-27, 2022.5)

Construction results analysis, laboratory tests and numerical analysis were carried out to propose pre-verified specifications for the standard design of linings and inverts for mountain tunnels. An analysis of recently constructed Shinkansen tunnels focusing on defects in the linings, showed that the number of cracks requiring repairs was small and the usability was sufficiently satisfied. The applicable conditions of pre-verified specifications were shown from the case analysis of tunnels where floor swelling was observed after the start of operation and laboratory tests of rock samples. In

addition, in the case of a tunnel in soft ground, an analytical design of linings and inverts was conducted using beam-spring analysis, and it was confirmed that the safety is satisfied. From the above, the validity of the standard design as pre-verified specifications was confirmed.

Performance Verification Design Method of Plain Concrete Lining and Invert Assuming Ground Displacement after Completion

Keisuke SHIMAMOTO, Kazuhide YASHIRO, Noriyuki OKANO

(Vol.36, No.5, 29-35, 2022.5)

There are various structures in railway systems. It is required that structures have the same level of performance and that their performance should be verified quantitatively. Therefore, we proposed a method for verifying the performance of plain concrete lining and invert, and made a trial design assuming a mountain tunnel receiving ground deformation after completion. In the trial design, we estimated residual displacement from displacement speed, and imposed the corresponding displacement to the lining and invert using an analysis method of reducing the strength of the ground. As a result, it was found that the performance can be verified by the proposed method and that the required performance can be satisfied by adopting strong invert structures against heaving, even when large residual displacement exists to some extent.

Detailed Evaluation Method of Seismic Impact on Mountain Tunnel Entrance Using Response Displacement Method Considering Shape of Ground

Kazuhide YASHIRO, Jun IZAWA, Naoki ITO

(Vol.36, No.5, 37-42, 2022.5)

A detailed method for evaluating seismic impacts on mountain tunnel entrances was proposed, using response displacement method and static FEM structural analysis. The validity of the proposed method was confirmed by comparing the ground strain around a tunnel with the result of the ground response analysis. For the mountain tunnel entrance, the ground response analysis was performed by changing the gradient of the slope above the tunnel and the ground conditions to evaluate the influence of the slope, and restorability was checked using the proposed method. As a result, it was found that as the slope angle increases, the bending moment increases at the corners of some structures, and that changes in thickness and main steel bar of members might be necessary.

Trend Analysis of Segments and Tunnel Boring Machine for Railway Shield Tunnels

Koji FUNAKOSHI, Kiwamu TSUNO, Kiichi FUJITA, Kaho KINOSHITA

(Vol.36, No.5, 43-46, 2022.5)

Trends of railway tunnels constructed by the shield method were analyzed based on the database, which covers 388 construction cases since 1964 to 2013. This research investigated thickness and width of segments, numbers of divided segments and intervals of ring joints. The tendency of items regarding a shield machine was also described such as types of TBM, tail clearances between shield skin plates and segments, thickness of shield skin plates and backfill grouting.

Trial Design of Shield Tunnels Based on Revised Design Standards for Railway Structures (tunnel)

Ryo TAKIGAWA, Kiwamu TSUNO, Kaho KINOSHITA, Takashi USHIDA
(Vol.36, No.5, 47-50, 2022.5)

The design standards for railway shield tunnels have been revised for the purpose of introducing the performance-based design method to railway tunnels. This paper describes the method of performance verification for shield tunnels including performance items and verification indices. A trial design based on the performance-based design method against railway shield tunnels located in the sandy ground was carried out and performance items used for determining structural specifications were identified. The results were also compared with those obtained by the conventional allowance stress design method and it was found that both results were in general agreement with each other.

Trial Design of Mountain Tunnels Based on Revised Design Standards for Railway Structures (tunnel)

Kazuhide YASHIRO, Keisuke SHIMAMOTO
(Vol.36, No.5, 51-54, 2022.5)

Design standards for railway mountain tunnels have been revised to introduce a performance-verification design method to railway tunnels. This report outlines the performance-based design method introduced in this revision and outlines the procedures for design using this method. First, specific inspection methods for mountain tunnels under general design conditions are shown. Then, the results of trial design using the performance verification design method carried out for the railway mountain tunnel with reinforced concrete are shown, focusing on structural conditions and ground conditions.

Maglev Technology and Research Trends on Superconductivity

Masaru TOMITA

(Vol.36, No.6, 1-4, 2022.6)

Railway Technical Research Institute has conducted research and development of superconducting Maglev railways and superconductivity. In this paper, we introduce evaluation technology of the ground coils, wireless power transfer technology and linear rail brake technology as applied Maglev technology. In addition, we introduce outlines of our recent research such as the science of high-temperature superconductors, superconducting feeder cables, and superconducting magnetic energy storage.

Development of Inverter-less Excitation Method for a Linear Rail Brake

Yasuaki SAKAMOTO, Keigo UKITA

(Vol.36, No.6, 5-11, 2022.6)

Studies have been carried out on rail brakes applying linear induction motor technology. This brake is capable of generating braking force without contact. In addition to the aspect of non-contact brakes, no on-board power supply for energizing this brake is required by using dynamic braking. This dynamic braking is performed with an excitation inverter, however another method without using one is desired in order to reduce the cost. Therefore, an inverter-less excitation method using the self-excitation phenomenon of induction generators was devised and tested on a track wheel testing machine. We clarified that the method devised is useful as a low-cost excitation system.

Wireless Power Transfer System for Railway Vehicles with Improved Power Density of Onboard Coil

Hiroshi YODA, Keigo UKITA

(Vol.36, No.6, 13-19, 2022.6)

To enhance the flexibility of installation of wireless power transfer (WPT)

system on railway vehicles, we modified WPT to increase the power per unit opposing area of ground and onboard coil up to 150 kW/m² by setting mechanical gap between coils at 150-mm. In this paper, we describe the design of improved WPT system capable of collecting 150 kW with a single onboard coil and the results of bench test using a reduced model to verify the system.

Evaluation of Vibration Resistance of Levitation and Guidance Ground Coils by Electromagnetic Excitation Tests Using a Superconducting Magnet

Ryohei IKEDA, Katsutoshi MIZUNO, Minoru TANAKA
(Vol.36, No.6, 21-26, 2022.6)

During superconducting Maglev vehicles running, ground coils vibrate due to the reaction force of levitation force and guidance force. In electromagnetic excitation tests, a ground coil is vibrated under the strong magnetic field of a superconducting magnet. In this paper, we describe an examination of test conditions based on numerical analysis, a processing method for energizing only an unit coil to be evaluated, and the electromagnetic excitation test results of the levitation and guidance coil. We have evaluated the vibration resistance of levitation and guidance ground coils by electromagnetic excitation tests.

Evaluation of Electrical Characteristics of Superconducting Feeder Cables

Yusuke FUKUMOTO, Tomoyuki AKASAKA, Yuuki ARAI, Masaru TOMITA

(Vol.36, No.6, 27-32, 2022.6)

DC electric railway systems are widely used in Japan. However, they have some problems, such as voltage drops, limited use of regenerative brakes and energy transmission losses. We have been developing superconducting feeder cables for DC feeder systems as a next-generation railway system without transmission losses solving these problems. In order to apply this to railway systems, it is necessary to develop the method of connecting a superconducting feeder cable to a feeder circuit, and to meet the required specifications from railway systems. In this paper, we introduce R&D for the application of superconducting feeder systems to commercial lines.

Cooling Methods of Superconducting Feeder Cables

Yusuke KOBAYASHI, Atsushi ISHIHARA, Kenji SUZUKI, Yusuke FUKUMOTO, Masaru TOMITA

(Vol.36, No.6, 33-38, 2022.6)

When superconducting cables are installed in feeder cables, it is expected to improve regenerative efficiency, reduce power loss, level the load between substations and consolidate substations by suppressing voltage drops. On the other hand, it is needed to cool superconducting cables by a refrigerant such as liquid nitrogen for keeping a superconducting state. In this paper, the design concept of superconducting cables and cooling systems which constitute superconducting feeder systems is introduced, and the efficient circulation method of refrigerants is discussed. Also, the result of cooling tests performed after constructing a cooling system is reported.

Development of Superconducting Coils Using MgB₂ Wires

Taiki ONJI, Yusuke KOBAYASHI, Masaru TOMITA

(Vol.36, No.6, 39-44, 2022.6)

To realize carbon neutrality, we are developing energy storage technology. In the railway field, superconducting magnetic energy storage (SMES) has an advantage assuming a unique power load that frequently changes by train powering and braking. So, we have been developing superconducting coils for SMES using MgB₂ superconducting wire which has low cooling cost and manufacturing cost. It has been reported that MgB₂ superconducting wire is sensitive to bending strain and MgB₂ wire deteriorates under certain bending strain. Therefore, we evaluated superconducting characteristics of

superconducting stranded conductors. Also, the deterioration due to the dent was investigated. As a result, it was clarified that not only bending strain but also dents due to compression lead to deterioration of superconducting characteristics.

Fabrication and Characterization of High-temperature Superconducting Materials with High Magnetic Field

Tomoyuki AKASAKA, Atsushi ISHIHARA, Kenji SUZUKI, Masaru TOMITA
(Vol.36, No.6, 45-50, 2022.6)

Since superconducting bulk material is compact and can generate a strong magnetic field, it is expected to be applied to various devices as a magnetic field generation source. High magnetic field strength, magnetic field uniformity, and magnetic field stability are required so as to apply superconducting bulk material to magnets. In order to realize these high characteristics, we fabricated and evaluated MgB₂ and RE-based superconducting bulk material.

Recent Research on Railway-specific Dynamic Issues

Fumiaki UEHAN
(Vol.36, No.7, 1-5, 2022.7)

Railway system is composed of many sub-systems such as overhead contact lines, vehicles, tracks and structures, which interact with each other and show complex dynamic behaviors. We are working on elucidation and countermeasures of railway-specific phenomena caused by the interaction of the sub-systems such as damage due to natural disasters, train running safety, and deterioration of structures, using our own simulation and experiment/measurement technologies. In this report, as our research examples in the field of railway dynamics, we present some recent research works related to improvement of resilience against natural disasters, digitalization of structures maintenance, hybridization of OCL/pantograph simulation, weight reduction of train car body.

Analytical study on effect of Sliding Friction on Unstable Vibration of Pantograph

Yuki AMANO, Shigeyuki KOBAYASHI
(Vol.36, No.7, 7-16, 2022.7)

Sliding of the pantograph head and contact wire causes frictional force acting on traveling pantograph head in horizontal direction. If the coefficient of friction between the pantograph head and contact wire is large, unstable vibration of the traveling pantograph could be observed. To analyze this vibration, a 2-dof pantograph model considering frictional force acting on the pantograph head has been proposed. However, stability of the contact strip attached to the pantograph is not studied in this model. Therefore, this study proposes two types of a 2-dof contact strip model for the cases where the contact strip slides on rigid contact bar or overhead contact line. This 2-dof contact strip model considers vertical and pitching direction movement. In addition, a stability analysis method using the 2-dof contact strip model is also proposed. In this method, we apply the complex eigenvalue analysis to the 2-dof contact strip model. Furthermore, excitation test of actual contact strip for Shinkansen train was carried out to identify its dynamic characteristics. Then mode shapes and natural frequencies of the contact strip were identified by utilizing the Maxwell's reciprocal theorem. Moreover, the stability analysis based on the complex eigenvalue analysis was carried out using identified modal parameters.

Improvement of Running Safety of Railway Vehicles with Yaw Damper during Earthquakes

Kohei IIDA, Masahito KUZUTA, Yukio NISHIYAMA, Hiroyuki KANEMOTO, Daichi NAKAJIMA
(Vol.36, No.7, 17-26, 2022.7)

In recent years, railroad corporations have become increasingly concerned about running safety for conventional lines during earthquakes, especially in metropolitan areas. Therefore, for trains equipped with yaw dampers, the authors propose that of the yaw dampers are placed symmetrically front-to-back in bogie as a countermeasure against an earthquake. This paper also numerically clarifies that the proposed layout of yaw dampers improves running safety against sinusoidal oscillation. An actual bogie oscillation test was performed to validate the numerical results. From probabilistic perspective, it is shown that the proposed layout of yaw dampers and the conventional guard usually placed on sharp curves have almost same effects on improving running safety against seismic vibration of track.

Influence of Wheel Turning Trace on Wheel/Rail Tangential Contact Force Characteristics under Running in Rainy Conditions

Daisuke YAMAMOTO
(Vol.36, No.7, 27-34, 2022.7)

A wheel tread has wheel turning traces like grooves on a rubber tire tread. In the case of such a tread, the friction force of wheel/rail in wet conditions was expected to increase as was that of tire/road. Therefore, to clarify the relationship between wheel turning traces and friction force, tangential contact force measurements using a twin-disk rolling machine were carried out in several wet conditions. As a result, it was clarified that the friction force is almost unchanged regardless of the existence of wheel turning traces due to high iron's stiffness and that, especially under low velocity conditions, the friction force with wheel turning traces is smaller compared with that without wheel turning traces due to a small contact-patch. This means that the combination of wheel/rail is different from that of tire/road in terms of tangential force characteristics.

A Study on the Countermeasure Method for Gauge Corner Cracking by Reducing the Contact Pressure Between Wheel and Rail

Masahiro TSUJIE, Masaharu KONO, Tatsuya IDO, Hua CHEN, Yoshiaki TERUMICHI
(Vol.36, No.7, 35-40, 2022.7)

Gauge corner cracking (GCC) occurs in heat-treated rail installed on curved high rails with a radius of 600 m to 800 m. The GCC can propagate to the bottom of rail, resulting in rail breakage. However, no countermeasure has yet been developed to prevent GCC from occurring. The aim of this study is to investigate suppression method of GCC initiation by reducing the contact pressure between wheel and rail. Therefore, we focused on wear development of rail, and evaluated the effect of worn profiles of rail on wheel and rail contact. The results showed that the worn profiles of rail are effective in suppressing rolling contact fatigue that can develop into GCC by reducing the contact pressure between wheel and rail.

Structural Performance Evaluation of Existing Bridges by Acceleration Monitoring

Munemasa TOKUNAGA, Manabu IKEDA
(Vol.36, No.7, 41-50, 2022.7)

The aim of this study is to realize monitoring structural performance condition for concrete girders. At first, we have developed a method to restore displacement waveform based on acceleration waveform during train passing by utilizing the linear vibration theory. Numerical experiments have shown that the method can estimate the maximum displacement within approximately 5% errors. Furthermore, the equivalent linearized beam

theory has been extended to estimate reinforcing bar stress waveform based on the displacement waveform. These methods realized the structural performance evaluation of bridges such as riding comfort and fatigue fracture from acceleration measurements.

Verification of Longitudinal Level Irregularity Suppression Effect at the Structural Boundary by Ballasted Ladder Track

Tsutomu WATANABE, Shintaro MINOURA, Keiichi GOTO, Kodai MATSUOKA
(Vol.36, No.7, 51-57, 2022.7)

Numerical experiments were conducted using a three-dimensional numerical analysis model to quantify load dispersion performance of ladder sleepers at line structural boundary. As a result, it was revealed that compared with conventional prestressed concrete sleepers, the ladder sleeper can reduce the pressure on the sleeper bottom plane by approximately 70%. Furthermore, when laying the ladder sleeper at the structural boundary, it was shown that laying across the structural boundary may be more effective in reducing the pressure on the sleeper bottom plane than laying it in front of the structural boundary. Finally, the ladder sleepers were installed on commercial line to verify the effect in suppressing longitudinal level irregularity.

Development of Simulator to Accurately Reproduce Snow Accretion Phenomenon for Railway Vehicles Traveling in Snowy Areas

Kohei MUROTANI, Koji NAKADE, Yasushi KAMATA
(Vol.36, No.7, 59-68, 2022.7)

When accreted snow drops off train bogies, it might damage railway ground facilities along tracks, train devices, etc. To establish countermeasures against such snow accretion damage, we have developed a snow accretion analysis method to understand the snow accretion process. The “snow accretion analysis method” developed in this research consists of an “airflow calculation,” a “trajectory calculation” and a “snow accretion calculation.” In this research, we performed two kinds of snowfall wind tunnels to validate the proposed simulator.

Improvement of Numerical Method Focusing on Micro Mechanics of Ballasted Track

Akiko KONO
(Vol.36, No.7, 69-75, 2022.7)

Numerical simulation by DEM have been adopted as analysis methods for focusing on micromechanics of ballasted tracks. However, DEM simulation has issues of low quantitative accuracy because DEM models are subjected to be simplified to reduce a computational load. Therefore, DEM code was parallelized by using Open MP to decrease computing time that contribute to improve quantitative accuracy by using more precise models. Then the author validates simulation results by comparing with measured data from real railway lines.

August 2022 Vol. 63 No. 1 - No. 3

- 3-axis strain gauge, 139
 3D point cloud processing sensor fusion, 181
 5G, 155
 A Method for Estimating Bedrock Ground Motion Based on Nonlinear Time-history Analysis (P), 50
 actual train test, 44
 aerodynamic force coefficient, 37
 ATC, 187
 ATP, 187
 ATS, 187
 ATS-DK, 187
 automatic operation, 155
 automatic train operation, 187
 autonomous train operation, 155
 auto-transformer, 175
 ballast, 1
 base material of friction material, 88
 Basic Research in Track Technology: Current Work and Outlook (Per), 1
 battery degradation evaluation, 75
 bearing clearance, 212
 bending moment, 139
 bogie, 95
 brake control, 75
 brake friction material for Shinkansen, 88
 bridge, 133
 car body tilting, 75
 centrifuge modelling, 56
 CFD, 37
 clarification of phenomena, 159
 closure between rails, 193
 collapsed soil, 121
 compaction, 121
 concrete, 206
 contact strips, 128
 corrosion of reinforcing bar (rebar corrosion), 206
 countermeasures, 159
 COVID-19, 155
 cross-section repair, 206
 Cu-impregnated carbon, 200
 current collection, 128
 curving performance, 95
 DC feeding, 101
 DC feeding system, 175
 DC-DC converter, 175
 DC-DC Converter Control Method for High Voltage DC Feeding System to Improve Use of Regenerative Power (P), 175
 decarbonization, 151
 deep learning, 181
 degree of saturation, 121
 derailment quotient, 139
 design method, 108
 Design Method for GRS Integral Bridge with the Use of PCT Girder (P), 108
 Development and Validation of Drive-by Detection Method for Resonant Bridges (P), 133
 Development of Active Bogie Steering System to Improve Curving Performance (P), 95
 Development of Automatic Train Operation System Based on Intermittent Type ATP with Continuous Speed Checks (P), 187
 Development of High-speed Test Facility for Pantograph/OCL Systems (P), 128
 development of materials, 159
 Development of Train Operation Power Simulator Reproducing Commercial Operation (P), 101
 diagnosis, 79
 digital technology, 155
 digital twin, 84
 displacement sensor, 64
 drivability/maneuverability, 101
 drive-by inspection, 133
 early resumption, 64
 earthquake, 169
 earthquake resilience, 9
 Effective Specifications for the Cross-sectional Area of Tunnel Hoods for Reducing Micro-pressure Waves (P), 31
 Effects of Rotational Conditions on Performance of Gear Unit Pinion Bearing (P), 212
 electric power supply system (EPSS), 151
 electro-hydraulic actuator, 95
 embankment, 56, 121
 energy consumption, 101
 energy saving, 175
 energy-saving, 151
 equipment saving, 155
 equivalent single degree of freedom method of ground, 50
 ESDD, 163
 estimating method, 163
 Estimation Method of Seismic Damage of Bearings at Railway Structure by Displacement Sensor (P), 64
 evaluation methods, 159
 Evaluation of Material Properties of Pantograph Contact Strip by Microscopic Structure Model (P), 200
 existing structure, 79
 Experimental Study on Curve Squeal Noise with a Running Train (P), 44
 Exposition of Revision of Seismic Design Guideline for Overhead Contact Systems (P), 169
 fail-safe, 187
 finite element method, 200
 fixing force, 193
 floor heave mechanism, 115
 Floor Heave Mechanism and Effect of Countermeasures for Mountain Tunnels (P), 115
 friction coefficient, 88
 gear unit, 212
 GoA 2.5, 187
 ground vibration, 5
 GRS integral bridge, 108
 Heat Resistance Effect Evaluation Method of Copper-based Sintered Alloy Base Material on Friction Coefficient (P), 88
 high-speed railway, 133
 High-speed test facility for pantograph/OCL systems, 84
 High-speed wheelset dynamic load test facility, 84
 high-temperature friction apparatus, 88
 high-voltage DC feeding system, 175
 homogenization method, 200
 hunting motion, 75
 infrastructure maintenance, 13
 infrastructure scenario, 37
 input ground motion, 50
 inspection, 79
 insulator, 163
 integrated management, 13
 Integrated Railway Infrastructure Management System with Uniform Location on a Kilometerage Basis (P), 13
 interface, 206
 joint structure, 108
 kilometerage, 13
 Large-eddy Simulation of the Aerodynamics of a Simplified Train under Crosswinds (P), 37
 large-scale test facility, 5
 lateral force, 95
 LES, 37
 LiDAR, 181
 Lime improvement, 121
 line bearing, 64
 longitudinal level irregularity, 25

- low-frequency sound in open sections, 5
 Low-noise moving model test facility, 84
 machine element, 212
 maintenance, 79
 maintenance-saving, 151
 materials for railway applications, 159
 measurement of wheel-rail interaction force, 139
 meteorological, 163
 Method for Estimating Equivalent Salt Deposit Density on Insulator Surfaces Using Meteorological and Topographical Information Provided by Public Institutions (P), 163
 Method for Measuring Lateral Force Utilizing Shear Strains inside Wheel Load Measuring Holes of Instrumented Wheelset (P), 139
 micro-pressure wave, 5, 31
 Moisture Behavior in Concrete Repaired by Patching Observed with Neutron Imaging (P), 206
 moisture penetration, 206
 monitoring, 84
 mountain tunnel, 115
 new materials, 159
 noise, 5
 numerical study, 37
 open data, 163
 opening force, 193
 overhead contact line (OCL) equipment, 151
 overhead contact lines, 128
 Overhead Contact System, 169
 pantograph, 128
 pantograph contact strip, 200
 PCT girder, 108
 performance item, 19
 performance verification, 19
 performance-based design, 19
 Performance-based Design of Slab Track (P), 19
 phenomenon elucidation, 1
 pinion, 212
 PIV, 56
 point machine, 193
 position information, 13
 Proposal for Unsupported Sleeper Detection Method and Utilization in Track Maintenance (P), 25
 rail, 1
 rail vibration, 44
 railway infrastructure, 13
 railway noise, 44
 railway structure, 79, 169
 Recent Activities for Research and Development of Vehicle Technology (Per), 75
 Recent Research and Development for Improvement of Earthquake Resilience (Per), 9
 Recent Research and Development on Maintenance of Existing Railway Structures "Inspection, Diagnosis and Reinforcement" (Per), 79
 Recent Studies on Wayside Environmental Problems (Per), 5
 recovery, 9
 regenerative power, 175
 reinforcement, 79
 required performance, 19
 Research and Development Activities and Future Outlook in Materials Technology (Per), 159
 Research and Development on Power Supply Systems for a Sustainable Society (Per), 151
 resonance, 133
 restoration method, 121
 Restoration Technology of Embankment Reusing Collapsed Soil (P), 121
 restored waveform, 25
 rock moisture content, 115
 rubber bearing, 64
 running resistance, 101
 running safety, 139
 seismic damage inspection, 64
 seismic design, 56, 169
 Seismic Design of Embankments in Consideration of Damage Process during Earthquakes (P), 56
 sensing, 84
 Shinkansen, 31
 slab track, 19
 solid lubricants, 88
 speed-up, 31
 square cylinder, 37
 staff at the front end, 187
 steering control, 95
 strength, 9
 Study of Anomalous Characteristics Exhibiting Between Fixing Force of Switch and Tongue Rail Opening Force (P), 193
 supports, 169
 sustainability, 151
 switch, 193
 tapered roller bearing, 212
 Technology for Experiment/Measurement to Clarify Phenomena Specific to Railway System (Per), 84
 testing facility, 128
 thermal analysis, 88
 time domain, 50
 topographical, 163
 track geometry car, 25
 track maintenance, 13
 track panel, 25
 track-bed, 25
 Train Data Collection Device, 101
 train front monitoring, 181
 Train Frontal Obstacle Detection Method with Camera-LiDAR Fusion (P), 181
 train running simulation, 1
 Trend on Research and Development Activities Relating to Signalling and Telecommunication Systems in Railway Fields (Per), 155
 tunnel hood, 31
 unsupported sleeper, 25
 vehicle, 75
 vehicle auxiliary power, 101
 vehicle position detection, 75
 wayside environment, 5
 wheel vibration, 44
 wheel/rail noise, 44
 X-ray CT, 200

WCRR 2022 Held in Birmingham

WCRR 2022, the 13th World Congress on Railway Research, took place from June 6 to 10 in the International Convention Centre in Birmingham, UK, co-hosted by RSSB and the University of Birmingham (UoB). WCRR 2022 was organized by its Organizing Committee consisting of permanent members UIC, MxV Rail in the USA, RSSB in the UK, SNCF, DB AG, Trenitalia and RTRI, and WCRR 2022 special members UoB and UNIFE. Over 700 participants from about 20 countries took part in this congress, out of which about 60 were from Japan and 22 were from RTRI. Under the main congress theme “Reshaping our railways post-pandemic: Research with an impact,” three plenary sessions were held, and the technical sessions featured 178 presentations in oral sessions (10 from RTRI) and 129 presentations in interactive sessions (8 from RTRI). The next congress will be held in 2025 in Colorado Springs in the USA, hosted by MxV Rail.



Fig. 1 Panel discussion in Plenary Session 2



Fig. 2 Executive Director Furukawa and plenary session participants

QUARTERLY REPORT of RTRI

第 63 卷 第 3 号

2022 年 8 月 1 日 発行

監修・発行所：公益財団法人鉄道総合技術研究所

〒 185-8540 東京都国分寺市光町 2-8-38

発行人：芦谷公稔

問い合わせ：鉄道総研広報

Vol.63, No.3

Published date: 1 August 2022

Supervision/Publisher: Railway Technical Research Institute

Address: 2-8-38 Hikari-cho, Kokubunji-shi, Tokyo 185-8540, Japan

Issuer: Dr. Kimitoshi ASHIYA

Contact us: Public Relations, Railway Technical Research Institute

Mail Address: [www-admin @ rtri.or.jp](mailto:www-admin@rtri.or.jp)

QUARTERLY
REPORT of
RTRI